Doctoral Thesis

NUMERICAL ANALYSIS OF CONCRETE-FILLED TUBES WITH STIFFENING PLATES UNDER LARGE DEFORMATION AXIAL LOADING

phD student
Albert Albareda Valls

Directed by
Dr. Jordi Maristany Carreras

June 2012

Chapter II

STATE OF THE ART

※※※

The state of the art corresponding to this investigation has been separed into four different Sections. The first two refer to the acquired knowledge about the behavior of the two components forming concrete-filled tubes.

The third Section refers to the axial compressive response of concrete-filled tubes generally, by describing the process of confinement and the influence of the way of loading. Two different simplified methods are also described in order to obtain the maximum compressive plastic load.

And finally, the fourth Section is devoted to summary the most relevant numerical and experimental studies about concrete-filled tubes under compression. Thus, a short review of the existing literature about CFT sections and their derived typologies is presented in this Chapter.

※※※

Chapter II

STATE OF THE ART

2.1 Behavior of steel.

2.1.1 General considerations about elemental behavior.
2.1.2 Uniaxial stress state.
2.1.3 Biaxial and triaxial stress state.
2.1.4 The von Mises Yield Criterion for steel.

2.2 Behavior of concrete.

2.2.1 General considerations about elemental behavior.
2.2.2 Uniaxial stress state.
2.2.3 Biaxial stress state.
2.2.4 Triaxial stress state.
2.2.5 Yield criteria for concrete.
  2.2.5.1 Failure surface.
  2.2.5.2 Associated and non associated flow rule.
2.2.6 Elastic perfectly plastic models.
  2.2.6.1 Mohr-Coulomb Criterion.
  2.2.6.2 Drucker-Praguer Criterion
2.2.7 Elastic hardening-plastic models.
  2.2.7.1 Concrete Damage Plasticity model [CDP]
2.2.8 Experimental determination of the stress-strain curves and the evolution of damage.
  2.2.8.1 Uniaxial stress state.
  2.2.8.2 Triaxial stress state.

2.3 Structural response of CFT sections under compression.

2.3.1 Confinement effect.
2.3.2 Available simplified design methods.
  2.3.2.1 Simplified Method of Eurocode 4.
  2.3.2.2 Unified Theory [Zhong].
2.3.3 Influence of the loading process.

2.4 Experimental and Numerical studies about CFT sections under compression.

2.4.1 Studies about circular and rectangular concrete-filled tubes.
2.4.2 Studies about improved typologies derived from CFT sections.
  2.4.2.1 Concrete-filled double skin tubes [CFDST].
  2.4.2.2 Concrete-filled tubes stiffened with plates
  2.4.2.3 Concrete-filled tubes stiffened with plates

2.1 Behavior of steel.

2.1.1 General considerations about elemental behavior.

Steel is an almost elastic perfectly-plastic material that shows a constant behavior independently of the hydrostatic state. Its mechanical properties are currently well-known by the engineering community, as a result of its applicability in many different industrial and civil fields. Since there are lots of different steel qualities depending on their utility and requirements, this investigation has been only focused on the structural steel considered by the Eurocodes [see Chapter IV].

Independently of the yield and the ultimate stress in each case, all different steels share two elastic properties, capable of describing their initial behavior: these properties are the elastic modulus [E_s] and the elastic Poisson's ratio [ν_s]. The values of these two parameters for the elastic range are always the same, with the following values:

$$E_a = 210000\ MPa \qquad \textbf{(2.1)}$$

$$\nu_a = 0.283 \qquad \textbf{(2.2)}$$

2.1.2 The von Mises yield criterion for steel.

Plasticity in metals -especially in steel- is characterized by a significant ductility and by not being affected by the hydrostatic state. This is the reason why shear stress is the major cause of yielding in these materials; the problem then is to determine which function of shearing stress governs, according to an isotropic yield criterion. Yielding occurs when:

$$f(s_1, s_2, s_3) = 0 \quad \text{or} \quad f(J_2, J_3) = 0 \qquad \textbf{(2.5)}$$

Being:

s_1, s_2, s_3 *Principal stress deviators*
J_1, J_2, J_3 *Invariants of stress tensor*

For that purpose, two yield criteria are used: the *Tresca yield criterion*, and the *von Mises yield criterion*. The first one proposes that steel starts yielding when the maximum shearing stress reaches a critical value, *k*, equal to a half part of the tensile stress f_y; and the latter -dated in 1913- works with the octahedral shearing stress, as an alternative to the maximum shearing stress. This value comes from the physical interpretation of the stress invariants:

$$\tau_{oct} = \sqrt{\frac{2}{3} J_2} = \sqrt{\frac{2}{3}} k \qquad \textbf{(2.6)}$$

which can be reduced to the form:

$$f(J_2) = J_2 - k^2 = 0 \qquad \textbf{(2.7)}$$

where *k* in this case, is the yield stress in the state of pure shear. Yielding will occur in a uniaxial tension test, when $\sigma_1 = \sigma_y$; $\sigma_2 = \sigma_3 = 0$. By replacing these two values into this last equation, it can be derived:

$$\sigma_y = \sqrt{3} \cdot k = 1.732 \cdot k \qquad \textbf{(2.8)}$$

Equation (2.7) clearly describes a circular cylinder circumscribed on the Tresca hexagon. For pressure-independent materials, the yield criterion has the following general form: $f(J_2, J_3) = 0$; then, the simplest mathematical expression, compatible with this condition, is equation (2.8). The intersection of the von Mises yield surface with the coordinate $\sigma_3 = 0$ draws a perfect ellipse, which corresponds to the following equation [see figure II.3]:

$$\sigma_1^2 + \sigma_2^2 - \sigma_1 \cdot \sigma_2 = \sigma_y^2 = 3k^2 \qquad \textbf{(2.9)}$$

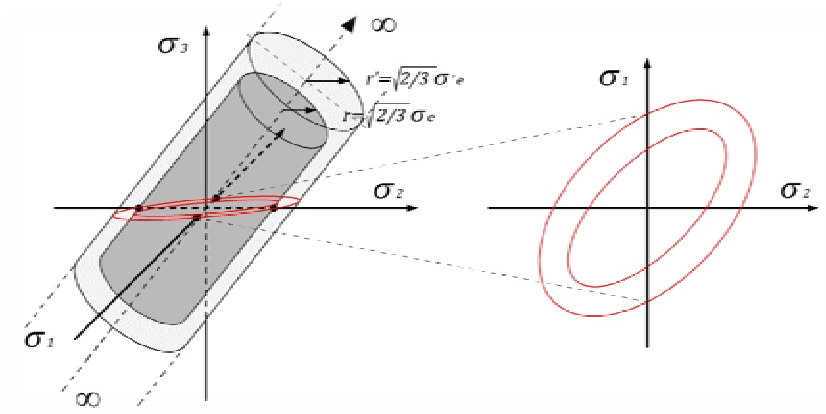

Fig. II.3 Von Mises cylindrical surface and its intersection with the (σ_1, σ_2) plane.

The radius of the cylinder is equal to $r = \sqrt{\frac{2}{3}}\,\sigma_e$

The intersection of the mentioned surface with the $(\sigma_x\ , \tau_{xy})$ plane also gives an ellipse as a result, whose equation is:

$$\sigma_x^2 + 3\tau_{xy}^2 = 3k^2 \qquad \textbf{(2.10)}$$

In conclusion, in order to describe the yield criteria of steel it is important to highlight four basic assumptions:

1. The material is isotropic.
2. The material behavior is independent of hydrostatic pressure. [$\sigma_h = \sigma_1 + \sigma_2 + \sigma_3$]
3. Yield stresses in uniaxial tension and in compression are equal.
4. Surfaces obtained are convex.

In concrete-filled tubes, steel is usually subjected to a biaxial state with a positive value for the component of hoop stress. Then, the resulting maximum vertical stresses f_{yt} and f_{yc} could be obtained through the following expressions, (Hatzigeorgiou, 2008):

$$f_{yt} = 0.5 \cdot \left(\sigma_h + \sqrt{4f_y^2 - 3\sigma_h^2}\right) \qquad \textbf{(2.11)}$$

$$f_{yc} = 0.5 \cdot \left(\sigma_h - \sqrt{4f_y^2 - 3\sigma_h^2}\right) \qquad \textbf{(2.12)}$$

2.1.3 Uniaxial stress state.

The description of the uniaxial stress-strain diagram, obtained from a pure compression test or a pure tension test is quite explicit to understand the global behavior of the material. The difference between the maximum axial load of the compressive and the tensile response is about 10%, and usually is not considered in literature. The steel behaves as a perfectly elastic material until reaching the limit stress value -known as yield limit stress, $\boldsymbol{\sigma_y}$; in addition, the material behaves linear up to the 80% of this yield stress, knowing this point as the *proportionally limit*, $\boldsymbol{\sigma_{pl}}$ [see figure II.1].

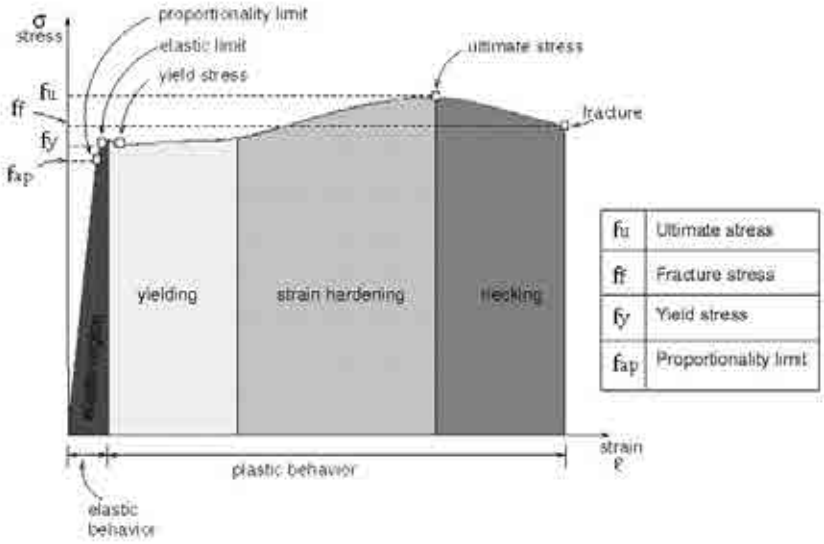

Fig. II.1 Idealized uniaxial stress-strain curve of steel.
The elastic region is linear until σ_{pl}, and elastic until σ_y.

Beyond the yield limit stress, the material shows a residual strain in case of being unloaded. This phase is known as the *plastic plateau* or the "yielding" period, during which the steel deforms almost without stress increment. The plastic period lasts over ten times more than the elastic one. For steel S355, the yield stress corresponds to a value of strain of 0.0017, and the end of the *yield plateau* coincides with a value of strain of 0.017. Once this value of plastic strain has been reached, the material starts a hardening period until reaching its ultimate stress; this behavior is typical of metals, and it consists in increasing the load-bearing capacity a 40% more before collapsing.

This last period after the ultimate stress is not usually considered in most structural analyses, since it deals with a clear descent of the mechanical strength until the final collapse.

The two elastic parameters described in Section 2.1.1 –the elastic Young's Modulus and the elastic Poisson's ratio- are relatively constant before the proportionality limit. Beyond this point, and up to the yield limit stress, their values evolve according to the following expressions, (Kuranovas, et al., 2009):

$$E_a^t = \frac{(f_y - \sigma_i)\cdot\sigma_i}{(f_y - f_{ap})\cdot f_{ap}}\cdot E_a \qquad \textbf{(2.3)}$$

$$\nu_a^t = 0.167\cdot\frac{(\sigma_i - f_{ap})}{(f_y - f_{ap})} + 0.283 \qquad \textbf{(2.4)}$$

2.1.4 Biaxial and Triaxial stress states.

It is important to consider that the behavior of steel under a biaxial state is slightly different from its behavior under a uniaxial stress state. The value of the maximum vertical yield stress under compression [$-\sigma_1$ in figure II.2] can be enhanced through an increase of lateral compressive stress [$-\sigma_2$][1]; in the same manner, it can be reduced by introducing lateral tension [$+\sigma_2$]. All the possible values of yield limit stress in the biaxial plane (σ_1, σ_2) describe a perfect elliptical curve; this curve coincides with the intersection of the normal plane to σ_3 with the cylindrical surface of the von Mises yield criterion –widely explained in the next Section.

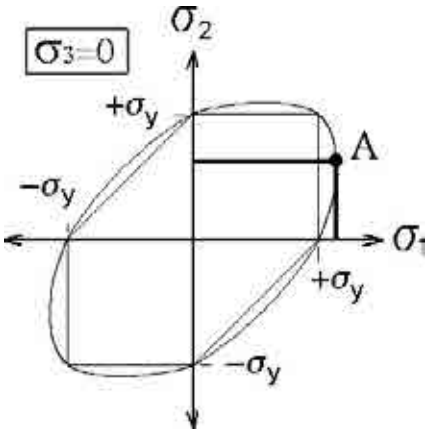

Fig. II.2 Elliptical curve of von Mises in the biaxial plane.
It corresponds to the intersection of the cylindrical surface with the (σ_1, σ_2) plane.

The von Mises yield criterion governs the stress state of cylindrical shells in CFT sections -which are usually biaxially stressed. This is the reason why they are not capable of reaching the maximum vertical stress, since part of this component is converted into hoop stress. In case of having also a third component, $\boldsymbol{\sigma_3}$, the structural response in the biaxial plane ($\boldsymbol{\sigma_1}, \boldsymbol{\sigma_2}$) would exactly the same.

2.2 Behavior of concrete.

2.2.1 General considerations about elemental behavior.

Contrary to steel, concrete is not an elastic perfectly-plastic material clearly. The *"elastic"* behavior of concrete is really limited to the 50% of its maximum compressive strength, and the stress-strain curve is far from being linear. However, the consideration of a first elastic and linear period until $\boldsymbol{0.5 \cdot f_{ck}}$ is widely accepted; after this linear period, there is another elastic-plastic nonlinear phase until the value of $\boldsymbol{f_{ck}}$. Beyond this point, concrete starts yielding through a surprising growth of strains with small or even negative stress increments.

The cohesive character of the material leads to analyze its plastic performance really different from that of steel. The assumption that concrete is a continuum material involves the use of a pressure-sensitive plasticity criterion such as the Drucker-Praguer -it will be widely explained in further Sections. Lateral expansion –and therefore, its consequent decrement of vertical stress- is caused

[1] See point A in figure II.2.

by the crushing of the cement paste between the aggregates of concrete, when it is subjected to high compressive stresses. We know that concrete expands much more than the value provided by Theory for its plastic range[2], and this phenomenon is due to crushing.

However, two mechanical parameters are also accepted for the elastic range; on the one hand, the initial elastic modulus, [$\boldsymbol{E_c}$], and, on the other hand, the elastic Poisson's ratio, [$\boldsymbol{\nu_c}$]. The first one can be calculated by using the accepted expression (2.12) from the ACI code (ACI, 1999), and the second one is a constant value which varies from 0.15 to 0.20, (Klink, 1975); a value of 0.18 has been considered in this work:

$$E_0 = 4700 \cdot \sqrt{f_{ck}} \qquad (2.13)$$

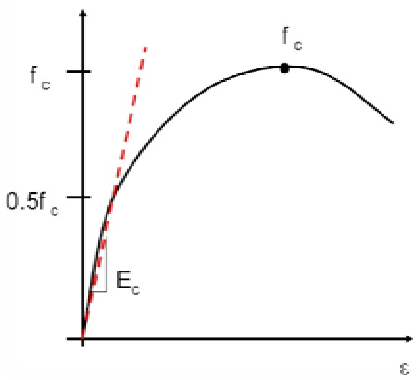

Fig. II.4 Initial elastic modulus of concrete.
The elastic modulus corresponds to stresses up to the 50% of f_{ck}.

From a value of a 50% of the maximum compressive stress, the stiffness of concrete starts an evolutionary damage process and the upslope is progressively relaxed, until reaching the final value of $\boldsymbol{f_c}$. A new softer proportional modulus is defined, instead of the initial one, and corresponding to the maximum compressive stress: the *Secant Young Modulus* –this value is commonly used in some applicative codes.

2.2.2 Uniaxial stress state.

The complete uniaxial stress-strain diagram for plain concrete is summarized in Fig. II.5: concrete behaves really different under tension than under compression. While under tension its behavior is almost completely elastic until the failure point F [see figure II.5], under compression, the material behaves elastic until stresses of 50% of the f_{ck} [point A]; from this point, the material shows a plastic behavior until the maximum compressive strength [at point C]. The compressive response beyond point C depends on concrete strength and hydrostatic conditions; usually, this response can be considered perfectly-plastic up to the beginning of the softening period in point D.

[2] The maximum theoretical value for the Poisson's ratio is $\nu'_c = 0.499$

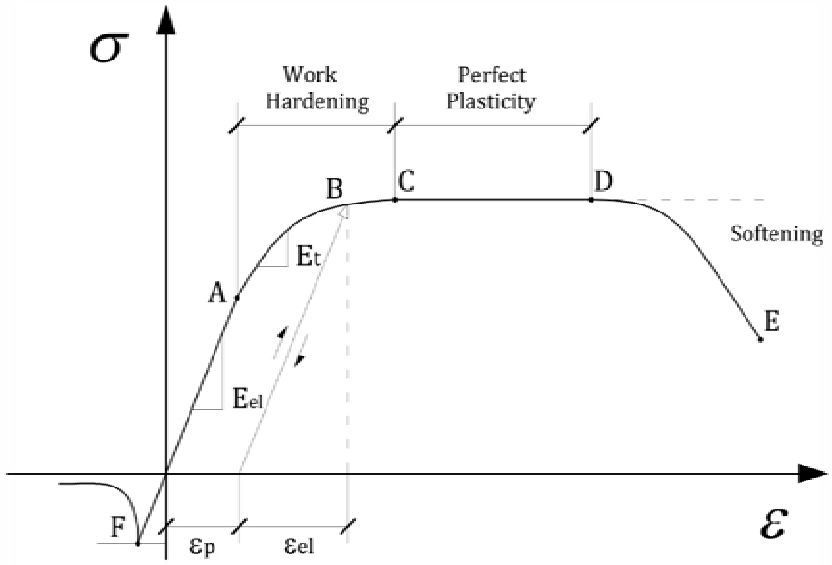

Fig. II.5 Idealized uniaxial stress-strain curve for plain concrete.
Tensile behavior is really different from compressive one.

Total strain at any point of the curve is obtained as a sum of the elastic strain [ε_{el}] and the plastic strain [ε_{pl}]. The difference between the nomenclature "*perfectly plastic"* and "*work-hardening"* for a material is its tolerance to the variation of permanent strain under a state of constant stress. In professional practice and applicative codes, it is assumed that concrete behaves perfectly-plastic under compression and elastic-brittle under tension. Thus, a yield criterion for plasticity under compression and a maximum stress for tension cutoff are assumed in order to define the failure surface. It is well-known that concrete shows a distinct behavior under states of high hydrostatic pressure; this consideration is really important in this study

The evolution of these curves is closely related with the volumetric expansion process, coming from the microcracking of the material. Before stresses of 30% of the f_c, microcracks do not take place; this is the reason why the available internal energy is less than the required energy in order to create new cracks. For stresses between the 30 and 50% of the f_c, first cracks appear between the aggregate of concrete, and keeping the load constant propagation of these cracks goes on clearly. In that case, internal energy of the material is larger than that required for cracking.

If concrete is unloaded from stresses about 50-70% of the f_c, the obtained stress-strain curve is clearly nonlinear and a slight hysteresis loop can be clearly observed, in case of reloading. Beyond the 70% of the maximum compressive stress, the unloading curve becomes strongly nonlinear and stiffness of the material becomes clearly damaged from this point.

By analyzing the volumetric strain, $\epsilon_v = \epsilon_1 + \epsilon_2 + \epsilon_3$, the change in volume is linear up to the 75% of f_c, (Babu, et al., 2005). From that point, the growth of volumetric expansion is nonlinear up to f_c, from where the direction of the volume increment reverses, starting a clear descent.

Concrete has an almost constant elastic Poisson's ratio up to the 70% of f_c (Persson, 1999). In this period, this value ranges from 0.15 to 0.22, as it has been commented before; beyond this point, lateral strains start growing quite quickly, by defining a new transversal ratio known as "*apparent Poisson's ratio"*. This new ratio can reach values from 0.80 to 0.90, even 1.0 (Loo, et al., 1990).

An approximated analytical expression to define the stress-strain curve shown before in figure II.5, was defined by (Popovics, 1973):

$$f_{ci} = f_c \cdot \frac{\varepsilon_i \cdot r}{\varepsilon_c \cdot \left[r - 1 + \left(\frac{\varepsilon_i}{\varepsilon_c}\right)^r\right]} \qquad \textbf{(2.14)}$$

where:

ε_c *Strain corresponding to the maximum value of compressive stress.*
f_c *Maximum compressive strength of concrete.*
r *Proportional ratio.*

by obtaining the parameter *r* through the following expression:

$$r = \frac{E_0}{\left(E_0 - \frac{f_c}{\varepsilon_c}\right)} \qquad \textbf{(2.15)}$$

being E_0, the initial modulus of elasticity of concrete mentioned in Fig. II.4.

2.2.3 Biaxial stress state.

In the past decades, various investigations have been carried out in reference to biaxial loading of concrete and microcrack propagation under this assumption: (Nelissen, 1972), (Tasuji, et al., 1978), etc. The first effect of being subjected to a biaxial state, is that all resistant capabilities become modified; for example, it has been proven that compressive maximum strength increases up to 25% more, in case of having a biaxial compressive state equivalent to $\sigma_2/\sigma_1 = 0.5$. Contrarily, this percentage is reduced when that proportion tends to a ratio of $\sigma_2/\sigma_1 = 1$. Thus, in those cases with a combined state of compression on one axis and tension on the other, the maximum compressive strength decreases linearly according to the applied tensile stress.

Another change in material properties refers to the ductility. Concrete subjected to a biaxial compressive state is clearly more ductile than under other assumptions, like under a uniaxial stress state only. Furthermore, in the nearby of the collapse, the material suffers a clear increase of volume; this inelastic volume growth is known as *dilatancy*. The maximum-strength envelope tends to be independent of the load path; for proportional loading, the failure of concrete under a biaxial state takes place according to the maximum-tensile-strain criterion.

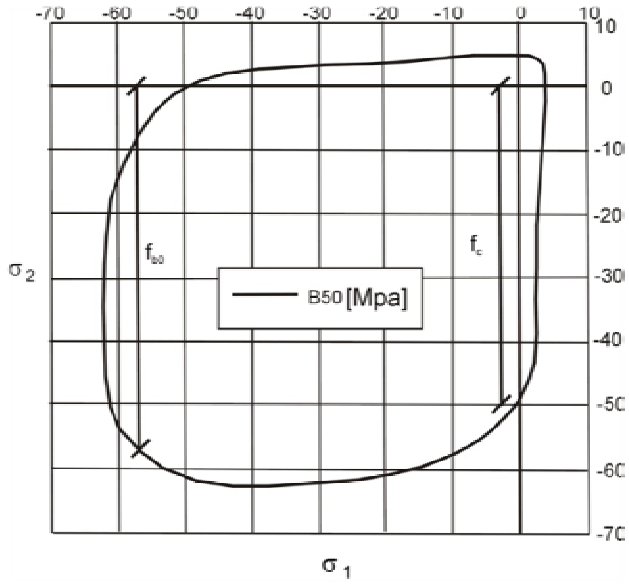

Fig. II.6 Biaxial stress envelope for 50MPa concrete.
Representative stresses are represented in the (σ_2, σ_1) plane.

2.2.4 Triaxial stress state.

Richart (Richart, et al., 1928) and Balmer (Balmer, 1949) carried out lots of different experimental tests of concrete subjected to triaxial compressive states. From all these experiments, the confined behavior of the material can be easily obtained, depending on hydrostatic state: quasi-brittle, plastic-softening or plastic-hardening. These behaviors are justified by the reduced possibility of bond cracking in situations of lateral pressure, and failure comes from crushing of the cement paste. Under triaxial state, concrete has a consistent failure surface which depends on the three principal stresses, and this surface, together with the elastic limit surface, can be represented in the three dimensional tensional space. A generalized expression for the stress-strain curve of confined concrete has been proposed by (Popovics, 1973), coming from function (2.14) [see figure II.7]:

$$f_{ci} = f_{cc} \cdot \frac{\varepsilon_i \cdot r}{\varepsilon_{cc} \cdot \left[r - 1 + \left(\frac{\varepsilon_i}{\varepsilon_{cc}}\right)^r\right]} \qquad \textbf{(2.16)}$$

where:

ε_{cc}	*Strain corresponding to the maximum value of confined stress.*
f_{cc}	*Maximum confined strength of concrete.*
r	*Proportional ratio.*

The parameter *r* can be obtained through:

$$r = \frac{E_c}{\left(E_c - \frac{f_{cc}}{\varepsilon_{cc}}\right)} \qquad \textbf{(2.17)}$$

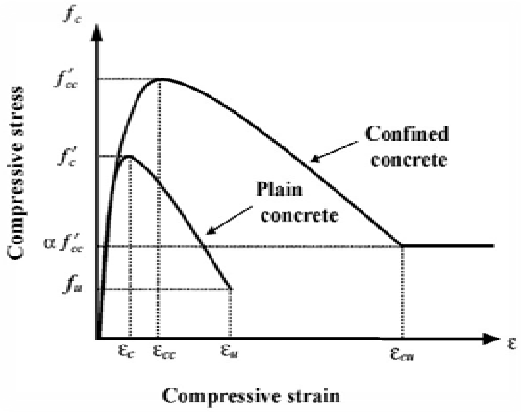

Fig. II.7 Stress-strain curves of plain and confined concrete.
(Susanta, et al., 2000)

However, also other researchers have proposed different approximate expressions in order to describe the behavior of confined concrete. One of them is Saenz (Saenz, 1964), who proposed the following approximation:

$$f_{ci} = \frac{E_c \cdot \varepsilon_{ci}}{1 + (R + R_E - 2)\left(\frac{\varepsilon_{ci}}{\varepsilon_{cc}}\right) - (2R - 1)\left(\frac{\varepsilon_{ci}}{\varepsilon_{cc}}\right)^2 + R\left(\frac{\varepsilon_{ci}}{\varepsilon_{cc}}\right)^3} \quad \textit{(2.18)}$$

where:

$$R = \frac{R_E(R_\sigma - 1)}{(R_\sigma - 1)^2} - \frac{1}{R_\varepsilon} \quad \textit{(2.19)}$$

$$R_E = \frac{E_c \cdot \varepsilon_{cc}}{f_{cc}} \quad \textit{(2.20)}$$

being $R_\sigma = 4$ and $R_\varepsilon = 4$.

In order to obtain the values of the maximum compressive strength in case of confined concrete, f_{cc}, there are lots of different criteria, too. The most used criterion is the one proposed by Richart in the beginning of the XXth Century (Richart, et al., 1928):

$$f_{cc} = f_c + m \cdot p \quad \textit{(2.21}$$

being p the lateral hydrostatic pressure and m a coefficient which can be approximated to 4.1 (Campione, et al., 2003). Mander (Mander, et al., 1988) also proposed an alternative formula for calculating the maximum confined compressive strength, modified some time later by O'Shea (O'Shea, et al., 1997):

$$f_{cc} = f_c \cdot \left(-1.288 + 2.172\sqrt{1 + \frac{7.46 \cdot p}{f_c}} - 2\frac{p}{f_c}\right) \quad \textit{(2.22)}$$

And finally, Attard (Attard, et al., 1996) also proposed another function for the same value:

$$f_{cc} = f_c \cdot \left(\frac{p}{f_t} + 1\right)^k \quad \textit{(2.23)}$$

$$k = 1.25 \cdot \left[1 + 0.062 \cdot \frac{p}{f_t}\right] \cdot f_c^{-0.21} \quad ; \quad f_t = 0.558 \cdot \sqrt{f_c} \qquad \textit{(2.24)}\ \textit{(2.25)}$$

To obtain the value of the ultimate confined strain, the most used formula is the one given by Popovics (Popovics, 1973):

$$\varepsilon_{cc} = \varepsilon_c \cdot \left[1 + 5 \cdot \left(\frac{f_{cc}}{f_c} - 1\right)\right] \qquad \textit{(2.26)}$$

In addition, Attard (Attard, et al., 1996) proposed also a different expression to get the same value, according to his investigations:

$$\varepsilon_{cc} = \varepsilon_c \cdot \left[1 + (8 + 0.05 \cdot f_c)\left(\frac{p}{f_t}\right)\right] \qquad \textit{(2.27)}$$

2.2.5 Yield criteria for concrete.

Under low hydrostatic states, concrete behaves according to the failure criteria, while under high pressures its response tends to follow the yield criteria. As it has been mentioned before in Section 2.2.4, concrete subjected to high hydrostatic stress states is capable of flowing and behaving as a perfectly-plastic material (Turgay, et al., 2009), while under uniaxial stress states the response is clearly governed by the failure criterion. In general, the existing literature refers to the term *"failure"* for the yielding behavior, as in case in reference to the fracture. For intermediate stress states, the failure criterion is sensitive to the hydrostatic pressure; this is the reason why the failure surface in concrete clearly differs from a cylinder on the hydrostatic axis. Thus, the shape of this surface will tend more to a cone, with its cross-sections completely symmetrical to the hydrostatic axis and not necessarily identical along this direction. The simplest mathematical surface to define this behavior is the perfect circular cone proposed by Drucker-Praguer, and it will be explained in the following sections.

2.2.5.1 Failure surface

The failure surface is represented by the three variables ξ, r, θ in the three-dimensional stress space ($\sigma_1, \sigma_2, \sigma_3$). The general form of this surface corresponds to the following expression:

$$f(I_1, J_2, J_3) = 0 \qquad \textit{(2.28)}$$

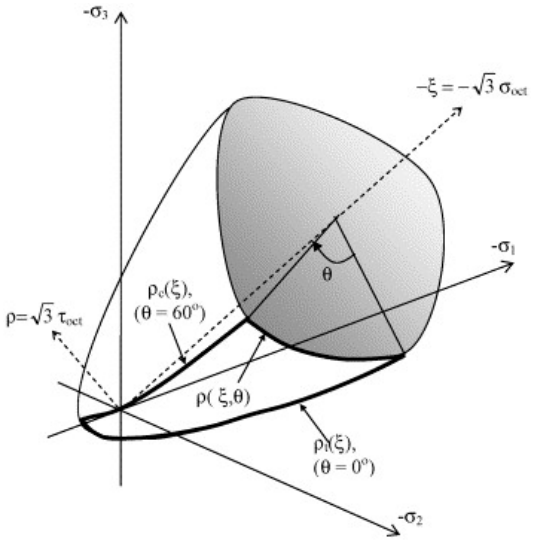

Fig. II.8 Geometrical interpretation of (ξ, r, θ) and $(\sigma_{oct}, \tau_{oct}, \theta)$

The conical form can be described by the shape of the surface in the meridian planes. The cross-sections of the failure surface coincide with the intersection curves between this surface and a deviatoric plane, normal to the hydrostatic axis with $\xi = constant$. The meridians of the failure surface are the intersection curves between this surface and a plane [called *meridian plane*, with θ = 0]. Normally, only the sector between θ = 0º and 60º is determined, and the other two are obtained by symmetry [see figure II.8]. Main characteristics of the failure surface of concrete are:

- Smoothness.
- Convexity for compressive stresses.
- Triangular shape for small compressions and circular for higher compressive stresses.

The two planes corresponding to θ = 0º and 60º are called the *tensile* and *compressive* meridians. The first corresponds to the case of having a concrete cylinder subjected to hydrostatic pressure in the radial direction, and a force in the vertical direction:

$$\sigma_r = \sigma_1 = \sigma_2 > \sigma_z = \sigma_3 \qquad \textbf{(2.29)}$$

This state corresponds to the compressive meridian, with a superimposed hydrostatic stress state and a higher compressive strength in the other direction as a result. Most resistant parameters of concrete are defined in this meridian [for example, f_c for a cylindrical specimen]. Another case is the tensile meridian, with a tensile force in the axial direction together with lateral pressure:

$$\sigma_r = \sigma_1 = \sigma_2 < \sigma_z = \sigma_3 \qquad \textbf{(2.30)}$$

There is a third meridian which is also used, known as the *shear meridian* [when θ = 30º].

Generally:

- Failure surfaces are curved, convex and smooth, and they depend directly on the hydrostatic component of stress I_1[3] or ξ[4].

[3] I_1 is the first stress invariant, coinciding with $I_1 = \sigma_1 + \sigma_2 + \sigma_3$.
[4] ξ is the axis where $\sigma_1 = \sigma_2 = \sigma_3$.

- r_t / r_c < 1, where *t* and *c* are the tensile and compressive meridians.
- The value of r_t / r_c increases with increasing hydrostatic pressures. It is about 0.5 near the π plane and 0.8 about a hydrostatic pressure of $\xi = -7f'_c$.
- In case of having pure hydrostatic loading, failure cannot occur.

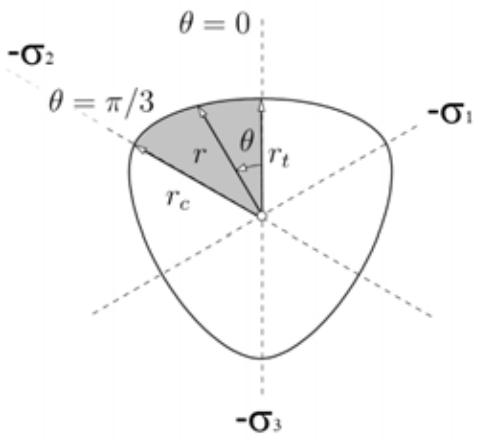

Fig. II.9 Deviatoric section of the failure surface.

2.2.5.2 Associated and Nonassociated Flow Rule

The concept of *plastic-potential function,* $g(\sigma_{ij})$ allows expressing the plastic flow in the following form:

$$d\epsilon_{ij}^{p} = d\lambda \frac{\partial g}{\partial \sigma_{ij}} \qquad \textbf{(2.31)}$$

where $d\lambda$ is a positive scalar factor that determines whether plastic deformations occur; if $d\lambda$ is different from zero, plastic deformation takes place. The equation $g(\sigma_{ij}) = const$ defines the surface of plastic potential, and the expression shown for $d\epsilon_{ij}^{p}$ implies that this vector is normally directed to the surface of plastic potential.

There is a case where the yield function and the plastic potential coincide in the following manner:

$$f = g \qquad \textbf{(2.32)}$$

then, the plastic-strain-increment can be rewritten as:

$$d\epsilon_{ij}^{p} = d\lambda \frac{\partial f}{\partial \sigma_{ij}} \qquad \textbf{(2.33)}$$

In this case, plastic flow takes place normally on the yield surface $\partial f / \partial \sigma_{ij}$ and it is called *associated flow rule* since the first becomes closely related to these surface; thus, under this assumption the yield criterion and the flow rule go hand in hand. This relation is valid for irreversible plastic materials, where plastic work cannot be recovered.

On the contrary, when the yield function does not coincide with the flow rule:

$$f \neq g \qquad \textit{(2.34)}$$

The case described by the relation (2.34) is known as *non associated flow rule*.

2.2.6 Elastic perfectly plastic models.

2.2.6.1 Mohr-Coulomb Criterion.

The Mohr-Coulomb criterion is based on the Mohr's criterion [1900], which postulate is derived from expression (2.35):

$$|\tau| = f(\sigma) \qquad \textit{(2.35)}$$

where the limit shearing stress τ in a plane is only dependent on the normal stress, σ, in the same plane at a specific point, and where the equation (2.36) is the failure envelope of the Mohr's circles - experimentally determined. According to this criterion, the failure of the material will occur for those states of stress in which the circle of Mohr is tangent to the envelope. The simplest form of the Mohr envelope is a straight line, known as the Coulomb's equation [Fig. II.10]:

$$|\tau| = c - \sigma \cdot tan\phi \qquad \textit{(2.36)}$$

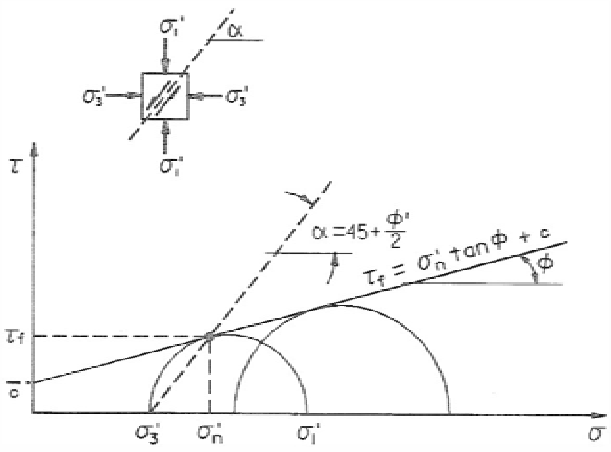

Fig. II.10 Coulomb's equation

where *c* is the cohesion of the material and ϕ, the internal-friction angle. By combining the Mohr's criterion with the Coulomb's equation, it can be derived the Mohr-Coulomb failure criterion. This postulate is very useful for approximating the failure of brittle-ductile materials like concrete, subjected to intermediate stress levels. Equation (2.36) can be expressed as:

$$\sigma_1 \frac{1 + sin\phi}{2c \cdot cos\phi} - \sigma_3 \frac{1 - sin\phi}{2c \cdot cos\phi} = 1 \quad \text{for } \sigma_1 \geq \sigma_2 \geq \sigma_3 \qquad \textit{(2.37)}$$

or, what is the same:

$$\frac{\sigma_1}{f'_t} - \frac{\sigma_3}{f'_c} = 1 \qquad \textit{(2.38)}$$

where:

$$f'_c = \frac{2c \cdot cos\phi}{1 - sin\phi} \tag{2.39}$$

$$f'_t = \frac{2c \cdot cos\phi}{1 + sin\phi} \tag{2.40}$$

The Mohr-Coulomb's criterion is a two-parameter model, defined by the combination of two different parameters, (c, ϕ), (f'_c, f'_t) or (f'_c, ϕ), etc. Sometimes to use the parameter *m* is useful, and it is defined by:

$$m = \frac{1 + sin\phi}{1 - sin\phi} = \frac{f'_c}{f'_t} \tag{2.41}$$

The use of *m* is helpful to obtain the value of the maximum compressive stress for concrete through the following expression:

$$m \cdot \sigma_1 - \sigma_3 = f'_c \qquad \sigma_1 \geq \sigma_2 \geq \sigma_3 \tag{2.42}$$

This means that the maximum value of compressive confined stress $[\sigma_3]$ is the result of adding the value of lateral pressure affected by a scalar coefficient *m* to the yield compressive stress $[f'_c]$. This coefficient has to be determined experimentally; from tests carried out by Richart (Richart, et al., 1928), a value for coefficient *m* can be approximated to 4.1.

By writing the Mohr-Coulomb's equation in terms of parameters r, ξ, θ:

$$f(r, \xi, \theta) = \sqrt{2} \cdot \xi \cdot sin\phi + \sqrt{3} \cdot r \cdot sin\left(\theta + \frac{1}{3} \cdot \pi\right) + r \cdot cos\left(\theta + \frac{\pi}{3}\right) sin\phi - \\ -\sqrt{6} \cdot c \cdot cos\phi = 0 \tag{2.43}$$

$$\text{with } 0 \leq \theta \leq \frac{1}{3}\pi$$

In the $\sigma_1, \sigma_2, \sigma_3$ coordinate system, this expression is represented by an irregular hexagonal pyramid with straight linear meridians and cross sections in the π plane, only defined by two dimensions, r_{co} and r_{to} [corresponding to θ = 0º and θ = 60º]. These two values can be easily obtained by replacing the following set of parameters, $\xi = 0, r = r_{to}, \theta = 0º$ and $\xi = 0, r = r_{co}, \theta = 60º$, in the expression of the failure surface. Alternatively, we have for the π plane:

$$r_{to} = \frac{2\sqrt{6} \cdot c \cdot cos\phi}{3 + sin\phi} = \frac{\sqrt{6} \cdot f'_c \cdot (1 - sin\phi)}{3 + sin\phi} \tag{2.44}$$

$$r_{co} = \frac{2\sqrt{6} \cdot c \cdot cos\phi}{3 - sin\phi} = \frac{\sqrt{6} \cdot f'_c \cdot (1 - sin\phi)}{3 - sin\phi} \tag{2.45}$$

It is well-known that the value f'_t does not coincide with the true value of the maximum tensile stress for concrete. For that reason, the Mohr Coulomb's criterion is usually extended with a tension cutoff in order to limit the maximum response of concrete subjected to tension.

2.2.6.2 Drucker-Praguer Criterion.

The Drucker-Praguer criterion consists in a smoother approximation of the Mohr-Coulomb surface, expressed as a simple modification of the von Mises yield Criterion[5]:

$$f(I_1, J_2) = \alpha \cdot I_1 + \sqrt{J_2} - k = 0 \qquad \textbf{(2.46)}$$

or in a similar way, by using the $(\boldsymbol{\xi}, \boldsymbol{r})$ system:

$$f(\xi, r) = \sqrt{6} \cdot \alpha \cdot \xi + r - \sqrt{2} \cdot k = 0 \qquad \textbf{(2.47)}$$

knowing that:

$$\xi = I_1/\sqrt{3} \quad \text{and} \quad r = \sqrt{2 \cdot J_2} \qquad \textbf{(2.48)}$$

One of the described ways to adjust the Mohr-Coulomb's hexagonal surface is by using the two parameters $\boldsymbol{\alpha}$ and *k*. In case of considering $\boldsymbol{\alpha} = \mathbf{0}$, then the latter expression can be reduced to the Drucker-Praguer one. Constants $\boldsymbol{\alpha}$ and *k* are related to cohesion and internal-friction angle of concrete through the following expressions, according to the theory of the flow rule of the Theory of Perfect Plasticity:

$$\alpha = \frac{tan\phi}{\sqrt{9 + 12 \cdot tan^2\phi}} \quad \text{and} \quad k = \frac{3c}{\sqrt{9 + 12 \cdot tan^2\phi}} \qquad \textbf{(2.49)}$$

It is curious to note how the failure function presented above, according to the Drucker-Praguer Criterion, is reduced to the Mohr-Coulomb Criterion for plane strain [with only two parameters].

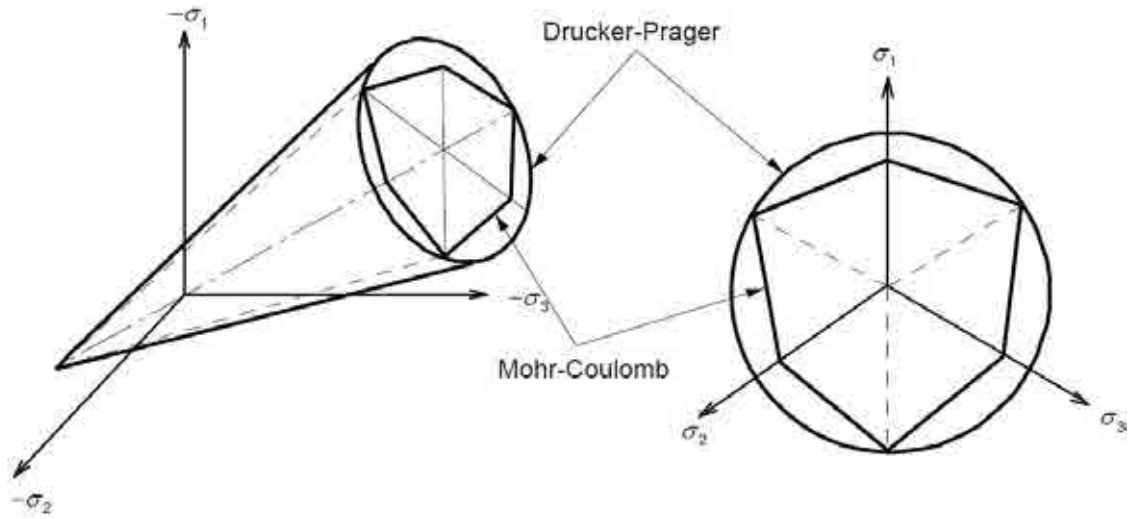

Fig. II.11 Graphical representation of the Drucker-Praguer yield surface.
This conical surface is the generalization of the Mohr-Coulomb's hexagonal surface.

[5] J_2 is the second invariant of a state of pure shear. $J_2 = 1/6 \cdot [(\sigma_1 - \sigma_2)^2 + (\sigma_2 - \sigma_3)^2 + (\sigma_3 - \sigma_1)^2]$

There are three criteria to define the general behavior under complex stress states for those materials which are considered perfectly-plastic. The first one consists in assuming that concrete behaves elastic until reaching its yield limit stress, and it is known as the *yield function*:

$$f(\sigma_{ij}) = k \qquad \textbf{(2.50)}$$

The second one is based on considering that plastic strain is infinite after yielding; in that situation, the stress state must always remain on the yield surface, and it is known as the *criterion of loading*:

$$df = \frac{\partial f}{\partial \sigma_{ij}} d\sigma_{ij} = 0 \qquad \textbf{(2.51)}$$

And the third criterion is the one in which the flow becomes permanent; it stops only when stresses are removed or have decreased below the yield limit stress. This last one is known as the criterion of *unloading*:

$$df = \frac{\partial f}{\partial \sigma_{ij}} d\sigma_{ij} < 0 \qquad \textbf{(2.52)}$$

The yield function $f(\sigma_{ij})$ is really significant when it is understood as a three-dimensional surface. This surface is defined in the three-dimensional stress space for isotropic materials, assuming that in those cases the fact of considering only principal stresses σ_1, σ_2 and σ_3 is allowed . This way, for a perfectly-plastic material, the yield function $f(\sigma_1, \sigma_2, \sigma_3) = k$ is a fixed surface in the stress space; in other words, each point inside the surface represents an elastic stress while each point on the surface represents a plastic stress.

Due to the unlimited character of plastic strain [ε_p] during flow, it is necessary to talk in terms of infinitesimal variations of strain [or strain increments, $d\epsilon_{ij}$]. As it has been explained before, the total strain increment is the result of the sum of elastic and plastic strain increments. The concepts of loading, unloading and neutral loading can be easily understood when f is interpreted as a surface in the 3-D space, and σ_{ij} and $d\sigma_{ij}$ the stress, and the stress increment vectors. For a perfectly-plastic material, this surface is completely fixed, while for a work-hardening material it expands and changes the shape depending on hardening. For a solid made of a work-hardening material in a plastic stress state, any additional infinitesimal loading $d\sigma_{ij}$ will produce only elastic strain if the vector $d\sigma_{ij}$ is directed inwards from the surface f [*unloading*]. Otherwise, it will produce both plastic and elastic strains, if that vector is directed outwards from that surface [*loading*]. If the increment $d\sigma_{ij}$ lies in the tangent plane to the loading surface, it produces only elastic strain [*neutral loading*]. For a perfectly-plastic behavior of a material, this stress point cannot be outside the yield surface. For that reason, the condition that defines the appearance of plastic flow [*criterion for loading*] is:

$$f(\sigma_{ij}) = k \quad \text{and} \quad df = \frac{\partial f}{\partial \sigma_{ij}} d\sigma_{ij} = 0 \qquad \textbf{(2.53)}$$

And the *criterion for unloading* is:

$$f(\sigma_{ij}) = k \quad \text{and} \quad df = \frac{\partial f}{\partial \sigma_{ij}} d\sigma_{ij} < 0 \qquad \textbf{(2.54)}$$

For a work-hardening material, at any stage of loading beyond the initial yield surface, a subsequent yield surface is developed. So, the case of perfect-plasticity is the limiting case of no work hardening.

2.2.7 Elastic-Hardening Plastic Models.

2.2.7.1 Concrete Damage Plasticity Model [CDP]

There are other material models for concrete based on a plastic hardening rule, combined with a damage criterion. These models reproduce the softening behavior after the peak of load faithfully, and they are known as CDP [Concrete Damage Plasticity]. This idea was introduced by Kachanov (Kachanov, 1958) and further was developed by Rabotnov (Rabotnov, 1969) and other researchers (Jankowiak, et al., 2005); it is based on a constitutive equation with scalar isotropic damage, adopting the following form:

$$\bar{\sigma} = (1 - d) \cdot E_0^{el} : (\varepsilon - \varepsilon^{pl}) = E^{el} : (\varepsilon - \varepsilon^{pl}) \qquad \textbf{(2.55)}$$

where:

σ	*Cauchy stress tensor*
d	*Scalar stiffness degradation*
ε	*Strain tensor*
E_0^{el}	*Undamaged (initial) elastic stiffness*

Therefore, $\boldsymbol{E^{el}}$ is the damaged elastic stiffness tensor. The effective stress tensor is defined as:

$$\bar{\sigma} = E_0^{el} : (\varepsilon - \varepsilon^{pl}) \qquad \textbf{(2.56)}$$

where:

ε^{pl}	*Plastic strain*

The variable which represents the degradation of the material is expressed as:

$$d = d(\bar{\sigma}, \tilde{\varepsilon}^{pl}) \qquad \textbf{(2.57)}$$

And it is governed by a stress tensor $\bar{\boldsymbol{\sigma}}$ and a hardening (softening) variable $\tilde{\boldsymbol{\varepsilon}}^{\boldsymbol{pl}}$. The Cauchy stress tensor is related to the effective stress tensor $\bar{\boldsymbol{\sigma}}$, through the same scalar degradation parameter $(\boldsymbol{1 - d})$:

$$\sigma = (1 - d) \cdot \bar{\sigma} \qquad \textbf{(2.58)}$$

Damage states in tension and compression are characterized independently by two hardening variables, $\tilde{\boldsymbol{\varepsilon}}_{\boldsymbol{t}}^{\boldsymbol{pl}}$ and $\tilde{\boldsymbol{\varepsilon}}_{\boldsymbol{c}}^{\boldsymbol{pl}}$, in reference to equivalent plastic strains under tension and under compression, respectively. Cracking and crushing in concrete are represented by increasing values of the hardening (softening) variables. These variables control the evolution of the yield surface and the degradation of the elastic stiffness.

The yield function represents a surface in the effective stress space which determines the states of failure or damage. For the plastic-damage model, the yield function arrives at:

$$f(\bar{\sigma}, \tilde{\varepsilon}^{pl}) \leq 0 \qquad \textbf{(2.59)}$$

And plastic flow is governed by a flow potential function $\boldsymbol{g}(\bar{\boldsymbol{\sigma}})$, according to the nonassociative flow rule:

$$\dot{\varepsilon}^{pl} = \dot{\lambda}\frac{\partial g(\bar{\sigma})}{\partial \bar{\sigma}} \tag{2.60}$$

The fundamental group of the constitutive parameters consists in four values which identify the shape of the flow potential surface and the yield surface. In the CDP model, the Drucker-Praguer hyperbolic function is accepted for the flow potential *g* in the following form:

$$G = \sqrt{(f_c - m \cdot f_t \cdot tan\beta)^2 + \bar{q}^2} - \bar{p} \cdot tan\beta - \sigma \tag{2.61}$$

where:

f_c	*Cauchy stress tensor*
f_t	*Scalar stiffness degradation*
β	*Strain tensor*
m	*Undamaged (initial) elastic stiffness*
$\bar{q}$	*Mises equivalent effective stress.*
$\bar{p}$	*Effective hydrostatic stress*

and knowing that:

$$\bar{p} = -\frac{1}{3} \cdot \bar{\sigma} \cdot I \tag{2.62}$$

and

$$\bar{q} = \sqrt{\frac{3}{2}\bar{S} \cdot \bar{S}} \tag{2.63}$$

where:

$\bar{S}$	*Deviatoric part of the effective stress tensor*

The nonassociative flow rule, which is used here, requires the definition of a loading surface; the plastic-damage model uses a yield condition, based on the loading function proposed by Lubliner and Oller (Lubliner, et al., 1989) in the following form:

$$f = \frac{1}{1-\alpha} \cdot (\bar{q} - 3 \cdot \alpha \cdot \bar{p} + \theta(\tilde{\varepsilon}^{pl})\langle \bar{\sigma}_{max} \rangle - \gamma\langle -\bar{\sigma}_{max} \rangle) - \bar{\sigma}_c(\tilde{\varepsilon}_c^{pl}) \tag{2.64}$$

The shape of the loading surface in the deviatoric plane is determined by the parameter $\boldsymbol{\gamma}$, while the determination of the parameter α is based on the Kupfer's curve in the biaxial plane (Kupfer, et al., 1979). $\bar{\boldsymbol{\sigma}}_{\boldsymbol{max}}$ is the algebraically maximum eigenvalue of $\bar{\boldsymbol{\sigma}}$, and the Macauley bracket $\langle \boldsymbol{x} \rangle$ is defined by:

$$\langle x \rangle = \frac{1}{2}(|x| + x) \tag{2.65}$$

and the function of $\boldsymbol{\theta}(\tilde{\boldsymbol{\varepsilon}}^{\boldsymbol{pl}})$:

$$\theta(\tilde{\varepsilon}^{pl}) = \frac{\bar{\sigma}_c(\tilde{\varepsilon}_c^{pl})}{\bar{\sigma}_t(\tilde{\varepsilon}_t^{pl})}(1-\alpha) - (1+\alpha) \tag{2.66}$$

Where $\bar{\boldsymbol{\sigma}}_{\boldsymbol{c}}$ and $\bar{\boldsymbol{\sigma}}_{\boldsymbol{t}}$ are the effective tensile and compresive cohesion stresses. The parameter α is defined by:

$$\alpha = \frac{(f_{b0}/f_c) - 1}{2(f_{b0}/f_c) - 1} \tag{2.67}$$

being:

f_{b0}	*Compressive strength under biaxial loading*

As the parameter α depends on the biaxial compressive stress, this factor will be necessarily obtained experimentally. Thus, the behavior of concrete depends only on four constitutive parameters, together with the tensile and compressive uniaxial or biaxial curves. In addition, a value for parameter $\boldsymbol{\gamma}$ has to be also defined, based on the existing triaxial compressive tests of concrete. According to Lubliner (Lubliner, et al., 1989), the value of $\boldsymbol{\gamma}$ can be approximated through:

$$\gamma = \frac{3(1-\rho)}{2\rho + 3} \qquad \textbf{(2.68)}$$

where:

$$\rho = \frac{(\sqrt{J_2})_{TM}}{(\sqrt{J_2})_{CM}} \text{ at a given state } \bar{p} \qquad \textbf{(2.69)}$$

being:

J_2	*Second invariant of stress*
TM	*Tensile Meridian* $\sigma_1 > \sigma_2 = \sigma_3$
CM	*Compressive Meridian* $\sigma_1 = \sigma_2 > \sigma_3$

Typical values of $\boldsymbol{\rho}$ range from 0.64 to 0.80.

From experimental curves, it is possible to determine the dependence between stress-cracking strain ($\tilde{\boldsymbol{\varepsilon}}_{\boldsymbol{t}}^{\boldsymbol{ck}}$) in uniaxial tension and stress-crushing strain ($\tilde{\boldsymbol{\varepsilon}}_{\boldsymbol{c}}^{\boldsymbol{in}}$) in uniaxial compression. In order to define the material behavior, it is necessary to identify the shape of the flow potential and the loading surfaces; these two surfaces can be determined completely by the four parameters commented before: $\boldsymbol{\beta}, \boldsymbol{m}, \boldsymbol{f}$ **and** $\boldsymbol{\gamma}$:

$$f(\beta, m, f, \gamma) \qquad \textbf{(2.70)}$$

Apart from all previous considerations concerning to the plastic range, it is also supposed an elastic period until the 30% of $\mathbf{f_c}$ under compression, and the 70% of $\mathbf{f_t}$ under tension.

The evolution of $\boldsymbol{d_c}$ and $\boldsymbol{d_t}$ depending on cracking and crushing strains, has to be determined separately. On the one hand, the stress degradation under compression is linear or parabolic while the plastic descent under tension is clearly exponential. The two figures shown below, illustrate the two plastic hardening behaviors:

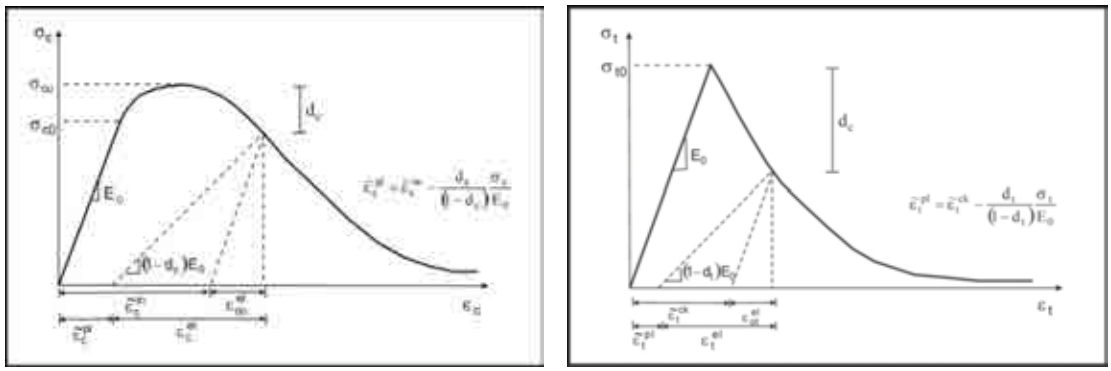

a) b)

Fig. II.12 Degradation of concrete under compression [a] and under tension [b].
The first one tends to be parabolic, while the second one is exponential.

2.2.8 Experimental determination of the stress-strain curve and the evolution of damage.

2.2.8.1 Uniaxial stress state.

In order to determine the stress-strain curves under tension and compression for plain concrete, cylindrical specimens of 300 mm height and 150 mm width are usually used. In substitution, cubic specimens of 150x150x150 mm can also be employed, by applying some correlative equivalent expressions. The accepted value for the maximum compressive strength $\boldsymbol{f_{ck}}$ corresponds to the maximum compressive stress by using these mentioned cylindrical specimens; in case of testing cubic specimens instead, the maximum compressive strength would be calculated by using the following expression proposed by (Viso, et al., 2008):

$$f_{ck} = \sigma_{1,cub} \cdot \beta = \sigma_{1,cub} \cdot \sqrt{\frac{L}{L + L_c}} \qquad \textbf{(2.71)}$$

where:

$\sigma_{1,cub}$	*Principal vertical stress of the cubic specimen.*
β	*Corrective factor*
L	*Width of the cubic specimen tested.*
L_c	*Constant value depending on material. From experiments,* L_c = 300 mm

On the one hand, a value of 0.913 has been assumed for the corrective factor $\boldsymbol{\beta}$, coming from experimental tests. On the other hand, an approximate value of 300 mm has been used for the parameter $\boldsymbol{L_c}$, assuming this value for plain concrete.

The experimental uniaxial stress-strain curves, used in this research to determine the evolution of stress up to $\boldsymbol{f_{ck}}$, are the ones defined by (Kaar, et al., 1978) for all kind of concrete strengths. In diagrams of figure II.13, it can be observed how sharper is the failure of each specific concrete, as higher is its compressive strength. This is the reason why ductility is directly related to the maximum compressive strength; however, it is also important to highlight that the significant descending slope of the softening period [with almost no residual stress] occurs only in those uniaxial stress states. Softening behavior depends on the hydrostatic stress state directly, and the plastic hardening evolutionary law behaves really different depending on lateral pressure [this effect will be widely explained in the following Section, corresponding to triaxial stress states].

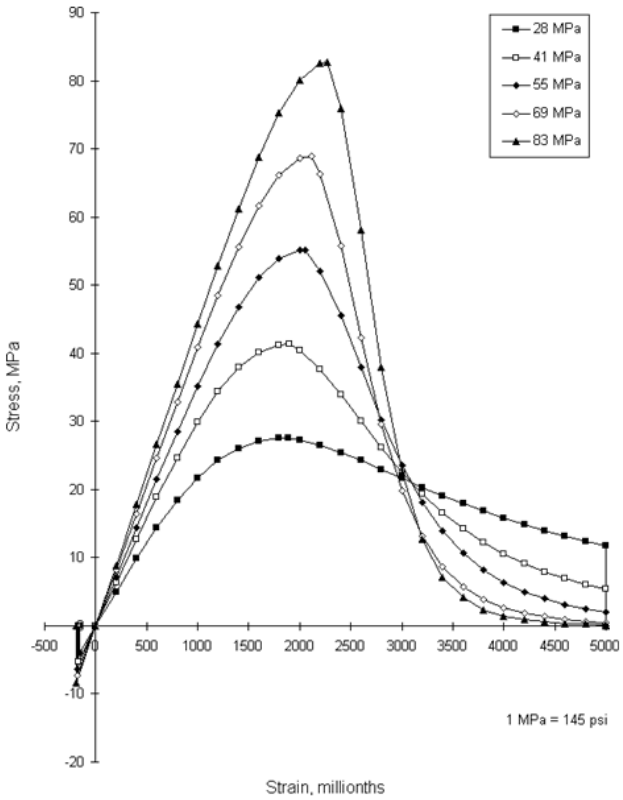

Fig. II.13 Uniaxial stress-strain curves for different concrete strengths.
These are the curves considered by the American ACI, (Kaar, et al., 1978).

Apart from defining the uniaxial stress-strain curves in order to determine the input parameters for the damaged plasticity model for concrete [DPC], it is also necessary to consider two evolutionary laws for compressive and tensile evolutionary damage ratios. These parameters represent the stiffness degradation of concrete during the loading process, from a stress point corresponding to the 50% of the $\boldsymbol{f_{ck}}$. The parameter known as *damage ratio* [$\boldsymbol{d_c}$] ranges from 0 to 1 [being 1, undamaged, and 0, completely damaged]. This value can be obtained through a set of cyclic compressive tests, based on loading and unloading. From experimental curves, it can be clearly observed how the ascending branch is degraded as reloading progresses. Obviously, the stiffness degradation depends not only on the axial plastic strain, but also on the hydrostatic stress state, as it is expressed by the expression (2.57):

$$d = d(\bar{\sigma}, \tilde{\varepsilon}^{pl}) \qquad \textbf{(2.57)}$$

In uniaxial stress states, this degradation depends only on axial plastic strain, and it can be easily standardized according to the concrete strength, depending on ductility and residual stress. From the experimental tests carried out by Karsan and Jirsa (Karsan, et al., 1969), the stiffness degradation corresponding to a 30MPa concrete at the peak of load is about a 20%, growing up to a 60% in the period corresponding to residual stress -with values about 0.45$\boldsymbol{f_{ck}}$.

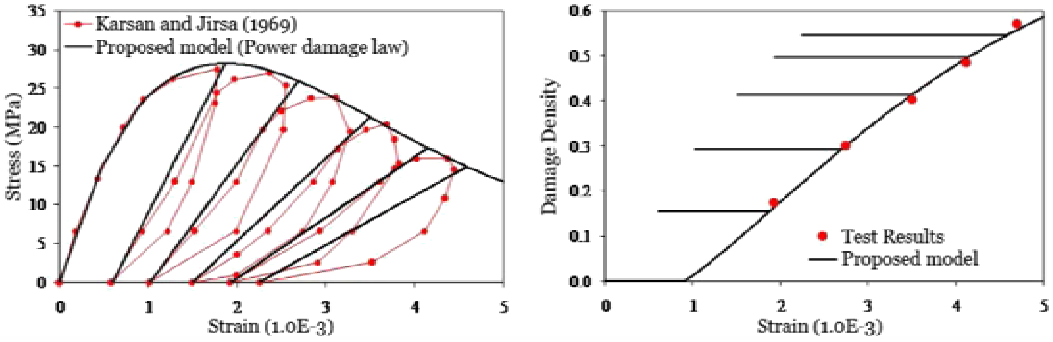

Fig. II.14 Uniaxial evolutionary damage ratio laws for 30MPa concrete.
Curves obtained experimentally by (Karsan, et al., 1969)

In figure II.14, it can be clearly seen how concrete core is affected by a process of degradation; the proportional modulus decreases progressively according to the mentioned scalar ratio, $\boldsymbol{d_c}$, and by following the expression:

$$E'_c = (1 - d) \cdot E_c \qquad \textit{(2.72)}$$

where $\boldsymbol{E'_c}$ is the damaged elastic modulus of concrete.

2.2.8.2 Triaxial stress state.

Very different from the uniaxial case is the triaxial stress state. The evolution of stress up to the maximum compressive limit $\boldsymbol{f_{ck}}$ for plain concrete -or $\boldsymbol{f_{cc}}$ for confined concrete- is determined by the shape of the failure surface; the confined curve is similar to the first one. From the peak of load, the evolution and the shape of the stress-strain curve during the softening period depends on the hydrostatic stress state basically. The values of the descending branch slope [Z] and the residual stress [α] have to be experimentally determined, in order to be capable of describing the post-peak behavior.

Depending on lateral pressure, compressive strength of concrete after the peak of load can decrease linearly or by following a parabolic function instead -as it has been previously explained in Section 2.2.9.1. In order to make the model much simpler, a basic linear function proposed by Susantha (Susanta, et al., 2000) has been used to represent the softening period in this investigation. Under high hydrostatic states, concrete does not suffer from softening thanks to the lateral pressure -this case would be the one with no descending branch, corresponding to a state of perfect plasticity, $\boldsymbol{\alpha = 1.0}$. The lower is lateral pressure, higher is the strength loss.

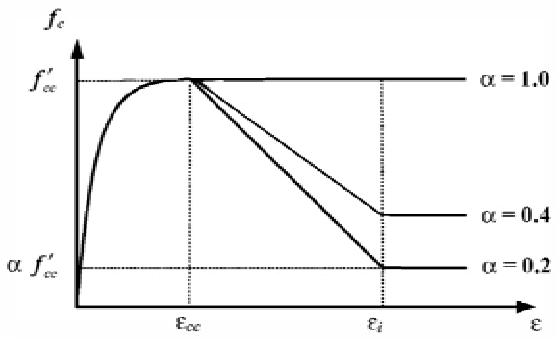

Fig. II.15 Determination of [Z] and [α] from experimental tests.
(Susanta, et al., 2000)

Confinement effect on concrete has a clear effect on the softening period, since lateral pressure clearly minimizes and delays the process of microcracking:

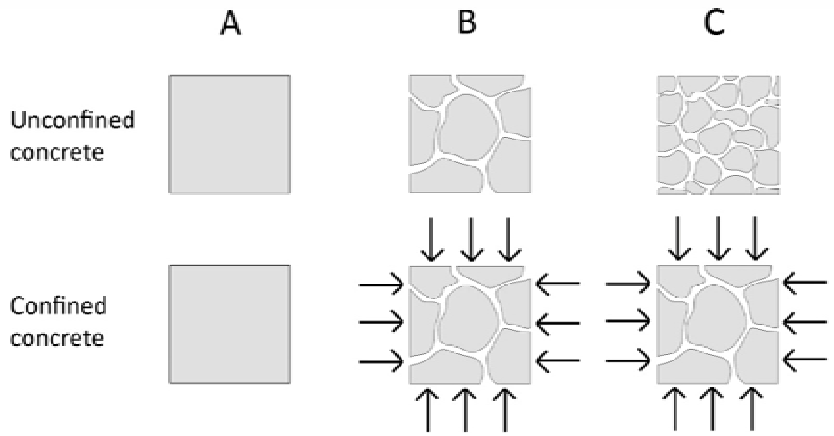

Fig. II.16 Influence of lateral pressure on softening.
Hydrostatic pressure minimizes the degradation process of concrete during the softening period.

Several investigations have focused their efforts on describing a general model, capable of reproducing the post-peak descending branch with accuracy. Susantha (Susanta, et al., 2000) obtained some universal experimentally-based expressions, with the clear objective of providing designers some simple criteria to predict softening in confined concrete. These expressions were all based on experimental tests done by other researchers before, in reference to circular and square concrete-filled tubes. Values of [Z] and [α] were obtained from the regularization of a set of experimental curves, as it is shown in figure II.17:

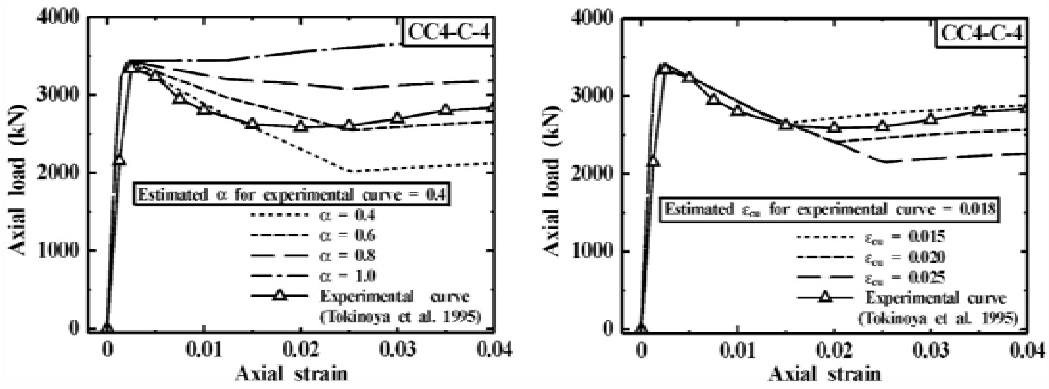

Fig. II.17 Determination of [Z] and [α] from experimental tests.
(Susanta, et al., 2000)

In general, the linear function corresponding to the descending slope:

$$Z = \frac{(1-\alpha)\cdot f'_{cc}}{(\varepsilon_i - \varepsilon_{cc})} \qquad \textbf{(2.73)}$$

Final expressions proposed by Susantha and Ge, and based on experiments, are the following:

For **circular-shaped** sections:

$$Z = \begin{cases} 0 & si\ \ R_t\left(f'_c/f_y\right) \le 0.006 \\ 1.0x10^5 \cdot R_t\left(f'_c/f_y\right) \cdot 600 & si\ R_t\left(f'_c/f_y\right) \ge 0.006\ y\ \ f_y \le 283MPa \\ 1.0x10^5 \cdot R_t\left(f'_c/f_y\right) \cdot 6000 & si\ \ R_t\left(f'_c/f_y\right) \ge 0.006\ y\ \ f_y \ge 336MPa \\ \left(\frac{f_y}{283}\right)^{13.4}\left[1.0x10^5 \cdot R_t\left(f'_c/f_y\right) \cdot 600\right] & si\ \ R_t\left(f'_c/f_y\right) \ge 0.006\ y\ 283 \le\ f_y \le 336MPa \end{cases} \quad \textbf{(2.74)}$$

being $R_t = \sqrt{3(1-\nu^2)} \cdot \left(f_y/E_a\right) \cdot (D/2t)$ for circular steel tubes.

and the ultimate plastic strain always coincides with an approximated value of $\varepsilon_{cu} = 0.025$.

For **rectangular and square-shaped** sections:

$$Z = \begin{cases} 0 & si\ \ R\left(f'_c/f_y\right) \le 0.0039 \\ 23400 \cdot R\left(f'_c/f_y\right) - 91.26 & si\ \ R\left(f'_c/f_y\right) > 0.0039 \end{cases} \quad \textbf{(2.75)}$$

$$\varepsilon_{cu} = \begin{cases} 0.04 & si\ \ R\left(f'_c/f_y\right) \le 0.0042 \\ 23400 \cdot R\left(f'_c/f_y\right) - 91.26 & si\ \ R\left(f'_c/f_y\right) > 0.0039 \\ 23400 \cdot R\left(f'_c/f_y\right) - 91.26 & si\ \ R\left(f'_c/f_y\right) > 0.0039 \end{cases} \quad \textbf{(2.76)}$$

being this case $R = (b/t) \cdot \sqrt{12 \cdot (1-\nu^2)/4\pi^2} \cdot \sqrt{f_y/E_a}$ for rectangular steel tubes.

Softening period is also related with the evolution of damage during the loading process. While the stiffness degradation advances quickly in uniaxial states [hand in hand with the loading process], in confined concrete this increment is clearly delayed. Actually, Luccioni together with his collaborators (Luccioni, et al., 2005) demonstrated that under high hydrostatic states damage is postponed or kept almost constant. These researchers carried out several tests with FRP-encased[6] specimens, comparing the obtained results with those coming from experiments about CFT sections. The conclusion is that the damage evolutionary law obtained from a cyclic loading test of CFT sections is much more severe than in FRP-encased concrete. This is caused by the elastic rigidity of FRP composites: these polymeric shells perform really well under circumferential tensile stresses, preventing concrete from early microcracking (Karabinis, et al., 2002).

In figure II.18, the experimental curve obtained from a cyclic loading uniaxial compression test is shown, corresponding to a FRP-encased tubular section; this experiment has been carried out by Mirmiran (Mirmiran, et al., 2000). In figure II.18, this curve is compared with that coming from a FE analysis, based on the Drucker-Praguer yield criterion. It can be easily noted that the difference between the two curves is not significant; the divergence lies basically in the evolution of damage, since the FE model follows an elastic perfectly-plastic model in which stiffness degradation is not

[6] FRP: Fiber Reinforced Polymer shells.

considered. Similarity between the two curves has much to do with the high confinement effect on concrete core confined by FRP-composites, in comparison with the unconfined.

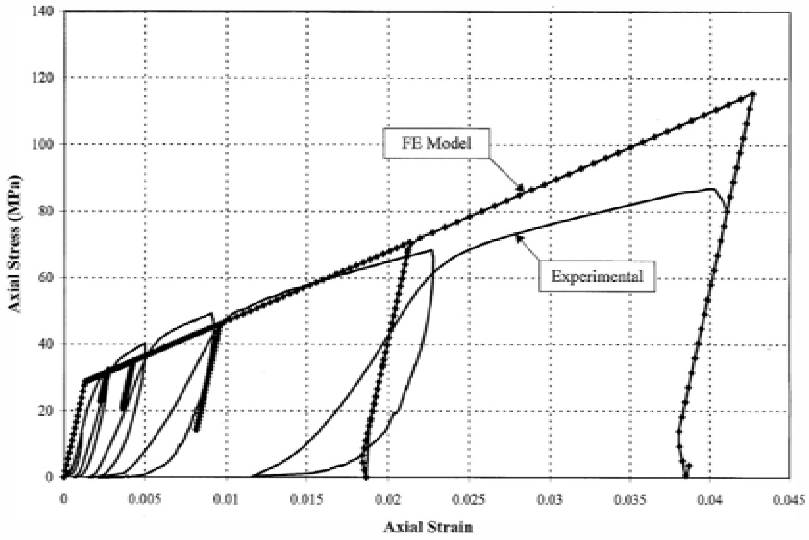

Fig. II.18 Comparison between the curves from the FE model and the experimental test.

2.3 Structural response of CFT sections under compression.

2.3.1 Confinement effect.

In circular concrete-filled tube sections, the horizontal component of the maximum lateral pressure provided by the tube to the core is equal to the maximum tensile force that steel can resist. Contrarily, vertical components of pressure are compensated themselves thanks to the circular geometry. According to Timoshenko [(Timoshenko, 1970), pages 28 to30], and Figure II.19:

$$f_r \cdot (D - 2t) = (\nu_e' - \nu_a) \cdot 2t \cdot f_y \qquad \textbf{(2.77)}$$

Therefore:

$$f_r = \beta \cdot \left(\frac{2t}{D - 2t}\right) \cdot f_y \qquad \textbf{(2.78)}$$

As it is shown in figure II.19, circular sections distribute lateral pressure uniformly along the perimeter of the core. This way, and owing to geometrical reasons, the tube becomes subjected to a biaxial state of circumferential tensile stress, and vertical compression (Bergman, et al., 1995).

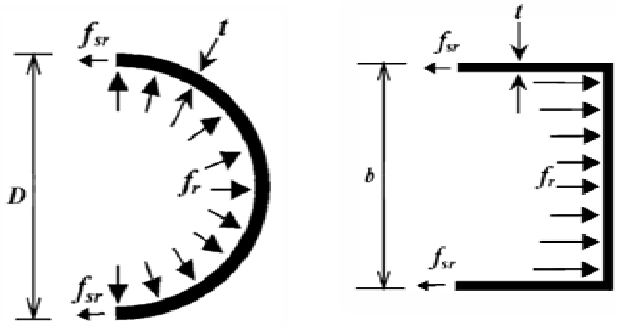

Fig. II.19 Stress distribution on concrete core due to confinement effect.
Distribution of pressure is different, depending on the shape.

A circular shape changes the uniform distribution of pressure into a pure tensile stress in the wall-thickness of the tube, with no bending stresses; this fact optimizes the performance of the tube and maximizes the confinement effect on the core. On the contrary, lateral pressure on rectangular plates of square-shaped tubes implies the appearance of bending stresses; needless to say that axial rigidity of the plates is much higher than its flexural stiffness. Therefore, the difference in the distribution of pressure on the core leads to lower confinement levels in square-shaped tubes.

2.3.2 Available simplified design methods.

There are several simplified methods to determine the maximum compressive strength of concrete-filled tubes. Some of them come from applicative codes and others from specialized researchers: from the first group, Simplified Method proposed by Eurocode 4 (EN1994-1-1, 1990) is presented below; belonging to the second group, the most representative method is the Unified Theory proposed by Shantong Zhong in 1998, (Zhong, et al., 1998).

2.3.2.1 Simplified Method of Eurocode 4.

The maximum plastic design load of a composite section in general -or *"squash" load*, (Bergman, et al., 1995), can be calculated through the expression provided by Eurocode 4[7]:

$$N_{pl,Rd} = \frac{A_a f_y}{\gamma_a} + \frac{A_s f_{sk}}{\gamma_s} + \frac{A_c f_{ck}}{\gamma_c} \qquad \textbf{(2.79)}$$

Or the same expression in terms of design strengths:

$$N_{pl,Rd} = A_a f_{yd} + A_s f_{sd} + A_c f_{cd} \qquad \textbf{(2.80)}$$

being:

A_a, A_s, A_c	*Area of the different components*
f_y, f_{sk}, f_{ck}	*Characteristic material strengths.*
$\gamma_a, \gamma_s, \gamma_c$	*Safety factors for materials [1.1 for steel, 1.15 for reinforcements and 1.50 for concrete]*

In circular concrete-filled tubes, concrete strength can be increased as a consequence of the confinement effect provided by the tube; in the same manner, axial capacity of steel has to be slightly reduced, owing to its biaxial stress state. Generally, the axial response of a CFT section can be enhanced about a 15% more than its nominal strength, only thanks to consider the effects derived from confinement. Slenderness is a decisive factor in order to determine the magnitude of this increment; for columns with a non-dimensional slenderness over 0.50, this enhancement should be neglected. Eccentricity is the second decisive parameter in determining the maximum axial load; this eccentricity cannot exceed the value of $d/10$, in order to consider confinement, being d the outer diameter of the tubular section.

Then, the maximum load of a circular concrete-filled tube is defined by EC-4 (EN1994-1-1, 1990):

[7] only for short columns.

$$N_{pl,Rd} = A_a \eta_a f_{yd} + A_s f_{sd} + A_c f_{cd} \left[1 + \eta_c \frac{t}{D} \frac{f_y}{f_{ck}}\right] \quad \textbf{(2.81)}$$

being:

$$If \quad 0 < e \leq {}^{D}/_{10} \rightarrow \eta_c = \eta_{co} \cdot \left(1 - \frac{10e}{D}\right) \quad \textbf{(2.82)}$$

$$\eta_a = \eta_{co} + (1 - \eta_{ao}) \cdot \frac{10e}{D} \quad \textbf{(2.83)}$$

$$If \quad e > {}^{D}/_{10} \quad \rightarrow \eta_c = 0 \quad \textbf{(2.84)}$$

$$\eta_a = 1 \quad \textbf{(2.85)}$$

knowing that[8]:

$$\eta_{co} = 4'9 - 18'5\bar{\lambda} + 17\bar{\lambda}^2 \quad \text{but} \quad \eta_{10} \geq 0 \quad \textbf{(2.86)}$$

$$\eta_{ao} = 0'25(3 + 2\bar{\lambda}) \quad \text{but} \quad \eta_{20} \leq 1 \quad \textbf{(2.87)}$$

The squash load of a composite section, $N_{pl,Rd}$, is the maximum plastic load resisted by a short column. Nevertheless, buckling effects in slender columns may be significant; in this case, the maximum axial capacity can be calculated by following two different procedures. The first is based on analyzing the column by considering second-order effects and imperfections; the second uses the simplified method proposed by the Eurocodes which obtains the maximum load capacity of the column through a coefficient χ, as in case of steel sections [in Eurocode 3].

2.3.2.2 Unified Theory [Zhong]

The Unified Theory proposed by Zhong, (Zhong, et al., 1998) is based on the assumption that both materials forming a composite section work together as new material. Thus, concrete and steel are not considered with their own mechanical properties, since a new theoretical composite material is introduced. This way, the properties of these new materials and all its correlations come from experimental tests done by several researchers. It can be said that the behavior of CFT sections has unity, continuity and relativity.

[8] Being $\bar{\lambda}$ the non-dimensional slenderness ratio of the composite section, $\bar{\lambda} = \sqrt{N_{pl,Rk}/N_{cr}} \leq 0.5$

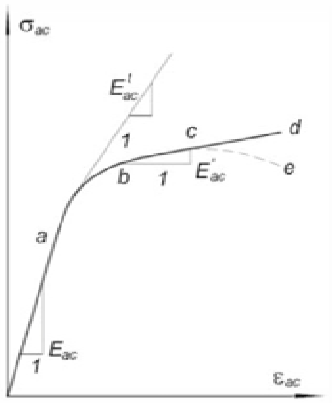

Fig. II.20 Idealization of the composite stress-strain curve.
The Unified Theory considers a new "composite" material, made of steel and concrete.

The Unified Theory for compression states can be summarized through the following equation, in order to determine the validity of a section:

$$N_{Ed} \leq 1{,}4\varphi N_0 \tag{2.88}$$

where:

N_{Ed} *Applied Axial Load*
N_0 *Axial plastic capacity of the section*
φ *Buckling coefficient*

The expression proposed by (Zhong, et al., 1998) to obtain the value of the initial axial load is the following:

$$N_0 = A_{ac} \cdot f_{ac} \tag{2.89}$$

being:

A_{ac} *The total area of the composite section,* $A_{ac} = A_c + A_a$

and the composite compressive strength:

$$f_{ac} = (1.212 + Bk_2\xi_0 + Ck_2^2\xi_0^2) \cdot f_{ck} \tag{2.90}$$

$$\xi_0 = \frac{A_a \cdot f_y}{1.1 \cdot A_c \cdot f_{ck}} \tag{2.91}$$

for circular sections:

$$B = 1.1759 f_y / 235 + 0.974 \tag{2.92}$$

$$C = -0.1038 f_{ck} / 20 + 0.309 \tag{2.93}$$

$$k_2 = 1.0 \tag{2.94}$$

for rectangular sections:

$$B = 1.131 f_y / 235 + 0.723 \tag{2.95}$$

$$C = -0.07 f_{ck} / 20 + 0.0262 \tag{2.96}$$

$$k_2 = \text{from } 0.71 \text{ to } 0.74 \qquad \textit{(2.97)}$$

The determination of coefficient φ is directly related to the slenderness of the column, ranging from 0.35 to 1.0[9].

2.3.3 Influence of the loading process.

In the determination of the maximum plastic squash load, the fact of considering the way of loading is strictly necessary. Although in the Eurocodes this consideration is not directly mentioned, the axial response of a CFT section can be very different depending on the way of applying the load. In the European code only the general expression (2.81) is presented, assuming that both components are loaded simultaneously. In the following figure II.21 three different possible hypotheses of loading are represented: [a] only the concrete is loaded, [b] both components are simultaneously loaded, and [c] only the steel is loaded.

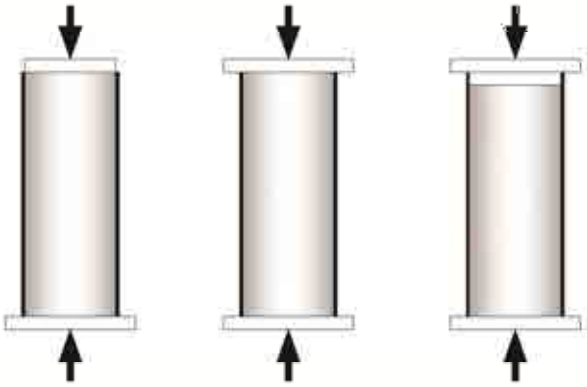

a) b) c)

Fig. II.21 Different ways of loading.

The way of loading the composite section is crucial to determine the compressive squash load.

To reproduce the value of the maximum axial load predicted by the Eurocodes using the expression (2.81), it is necessary to load both components at the same time [case b]. Under this assumption, both materials expand laterally according to their respective Poisson's ratios [first elastic, afterwards plastic]. While the elastic Poisson's ratio of steel is higher than that of concrete, confinement effect does not take place; once concrete starts to expand laterally beyond the value of its plastic Poisson's ratio [0.49] due to dilatancy, the core becomes quickly triaxially compressed. In the first case [a] of figure II.21, concrete expands laterally more than steel from the beginning, as the latter is loaded thanks to the friction forces of the interface only. As it can be derived from figure II.22, the maximum axial load in this first case is slightly higher than in the second one [as concrete is confined from the first instant]. Finally, in the third case [c], only the outer steel tube is strictly loaded, starting its lateral deformation independently from the core. This fact leads to act by separately; thus, concrete is not involved in loading unless shear stresses could be transferred through inner connectors.

[9] for short columns, it takes the value of 1.0.

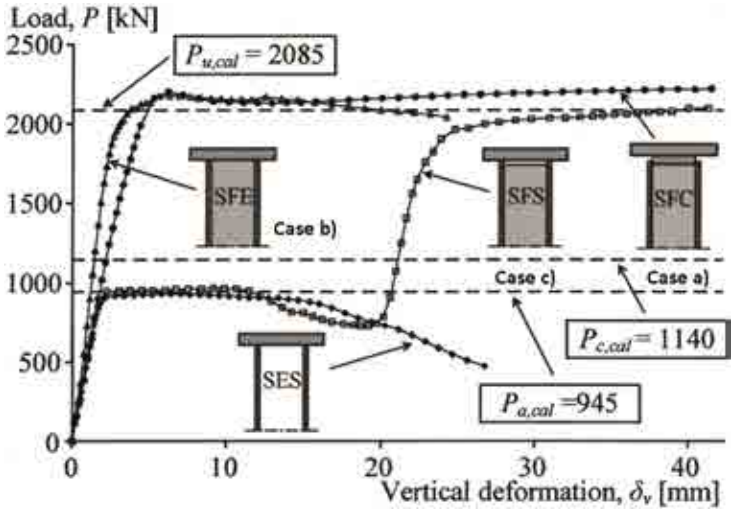

Fig. II.22 Load-deformation curves according to different ways of loading.
Curves shown come from experimental results carried out by Schneider (Schneider, 1998)

In figure II.22, the difference between the maximum values of axial load becomes explicit. The curves corresponding to cases [a] and [b] go hand in hand until the plastic hardening period; otherwise, case [c] reaches a low value of compressive load, decreasing until a value of vertical deformation about 20 mm. The fact that specimen [c] does not involve concrete until this advanced percentage of strain clearly shows that shear transference on the interface cannot be supposed without connectors. In a situation like this, it is necessary to calculate specific shear connectors to guarantee the load transference between the two components:

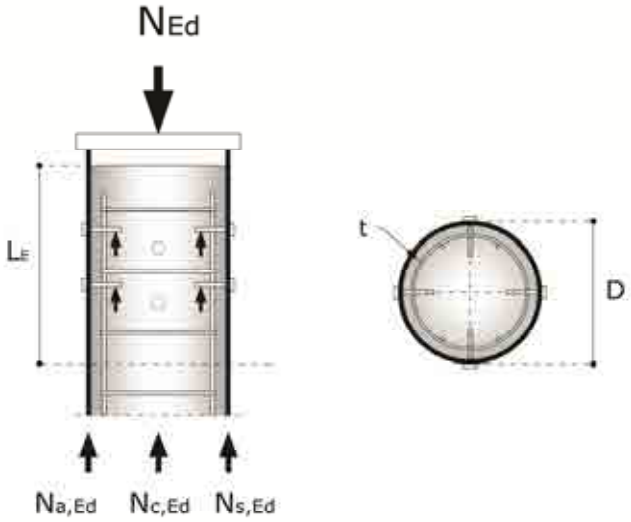

Fig. II.23 Practical example of shear connectors.
They must be placed preferably in the nearby of the loaded face.

To guarantee a correct bond and the load transference between components, and assuming that steel is only component loaded, it is necessary to introduce shear connectors on the interface, being the chemical and physical adherence not enough. Contrary, even being friction forces sufficient to guarantee the load transfer [by considering a maximum of 0.55 N/mm² of tangential stresses in

circular CFT sections], the sliding of the tube respect to the core could be really significant in the nearby of the loaded face. Dunberry (Dunberry, et al., 1987) demonstrated that this sliding could occur in a specific equivalent length from the loading face, which value coincides approximately with:

$$L_E \leq \begin{Bmatrix} 2D \\ L/3 \end{Bmatrix} \quad \textbf{(2.98)}$$

being D the diameter of the tube, and L its length.

Then, the shear force which will be absorbed through the interface is the difference between the axial capacity of concrete and the axial capacity of steel:

$$V_{L,Ed} = N_{c,Ed} - N_{a,Ed} = \frac{N_{Ed}}{N_{pl,Rd}} \cdot \left[N_{pl,c} - N_{pl,a}\right] \quad \textbf{(2.99)}$$

The maximum tangential stress which can be resisted by the interface according to EC-4, goes from τ_{Rd} = 0.40 N/mm^2 in rectangular CFT sections up to τ_{Rd} = 0.55 N/mm^2 in circular sections, (Hicks, et al., 2002). Therefore, the maximum shear force per column meter which can be absorbed is the product of this value by the inner surface of the tube:

$$V_{Rd} = 2 \cdot \tau_{Rd} \cdot \pi \cdot (R - t) \quad \textbf{(2.100)}$$

And the shear force absorbed by mechanical connectors [$V_{sc,Rd}$] can be easily calculated by subtracting the value of V_{Rd} from $V_{L,Ed}$, and knowing the capacity of a single connector. This way, it is possible to determinate the number of necessary connectors, n:

$$V_{sc,Rd} = V_{L,Ed} - V_{Rd} \quad \textbf{(2.101)}$$

$$n = V_{Rd} / P_{Rd} \quad \textbf{(2.102)}$$

where n is the number of connectors, and P_{Rd} the load resisted by a single connector.

2.4 Experimental and Numerical investigations about CFT sections under compression.

In the past recent decades, several experimental and numerical studies have been carried out in reference to concrete-filled tubes and other derived typologies, due to their improved ductility and strength, especially in seismic areas. Their complex behavior has motivated several researchers to further in them, supported by a growing interest shown by the engineering community and industry.

2.4.1 Studies about circular and rectangular concrete-filled tubes.

As explained in the previous paragraph, a wide collection of experimental and numerical results has been published in reference to the behavior of concrete-filled tubes. Most studies deal with the response under pure compression of these sections, since this is one of their most important

strengths. Numerous papers in reference to compression of CFT sections[10] are presented in the list shown below, chronologically from the eighties:

Researcher	Year	Main Purpose
(Morino, et al., 1984)	1984	Eccentricity of applied load, CFT experimental.
(Sakino, et al., 1985)	1985	Axial response, CFT experimental analysis
(Ge, et al., 1992)	1992	Geometric proportions in axial response, CFT experimental.
(Kilpatrick, 1994)	1994	Geometric proportions in axial response, CFT experimental.
(Uy, et al., 1996)	1996	Eccentricity of applied load, CFT experimental.
(Muñoz, et al., 1997)	1997	Eccentricity of applied load, CFT experimental.
(Schneider, 1998)	1998	Large strain response, CFT experimental tests.
(O'Shea, et al., 2000)	2000	Axial response of thin-walled CFT, exsperimental analysis.
(Susanta, et al., 2000)	2000	Axial response of circular / rectangular CFT, experimental.
(Elremaily, et al., 2002)	2002	Cyclic loading, CFT experimental analysis-
(Hu, et al., 2003)	2003	Axial response, CFT experimental tests.
(Naguib, et al., 2003)	2003	Creep, CFT numerical analysis.
(Han, et al., 2003)	2003	Pre-load on steel tubes, CFT experimental analysis-
(Liu, et al., 2003)	2003	Axial response of rectangular CFT, experimental analysis.
(Hu, et al., 2003)	2003	Axial response of circular / rectangular CFT, experimental.
(Fujimoto, et al., 2004)	2004	Eccentricity of applied load, CFT experimental.
(Giakoumelis, et al., 2004)	2004	Axial response of circular, CFT experimental analysis-.
(Liu, 2005)	2005	Axial response of rectangular CFT, experimental-.
(Kwon, et al., 2005)	2005	Long-term behavior, CFT experimental tests.
(Eid, et al., 2006)	2006	Confinement effectiveness, CFT numerical analysis.
(Ellobody, et al., 2006)	2006	High-strength concrete behavior, CFT numerical analysis.
(Liu, 2006)	2006	Axial response of rectangular CFT, experimental analysis.
(Yu, et al., 2007)	2007	Axial response, CFT experimental analysis-
(Choi, 2007)	2007	Axial response of circular, CFT experimental analysis-.
(Kuranovas, et al., 2007)	2007	Axial response of Hollow CFT, analytical
(El Fattah, 2008)	2008	Eccentricity of applied load, CFT experimental.
(Andrade de Oliveira, et al., 2009)		Confinement effectiveness, CFT experimental tests.
(Gajalakshmi, et al., 2011)	2011	Axial response of circular CFT, experimental.
(Almadini, 2011)	2011	Axial response of circular / rectangular CFT, experimental.

All these studies refer to short columns only, without considering slenderness effects. To achieve the maximum load-bearing capacity of columns, slenderness is a crucial factor to take into account; since this work refers only to short columns under pure compression in order to simplify and focus the analysis, the list of investigations presented before only deals with this hypothesis. As a consequence of the inherent complexity of these sections, their structural response has been progressively comprehended during these last decades, mainly thanks to experimental tests. Thanks to the available numerical tools and the large amount of published experimental tests, today it is already possible to describe the behavior of CFT sections only numerically, with quite accurate precision.

Derived from the extended use of these sections in some of the tallest structures of seismic areas, such as Hong Kong, Singapore or San Francisco, an increasing interest about the specificities of their behavior has emerged. This is the reason why we can find so much varied studies, ranging from local buckling to pre-loading effects or the influence of geometry and shape on confinement

[10] some of them used in this investigation for calibration purposes

effect. It can be said that, nowadays, the behavior of CFT sections under compression is really well understood by the engineering community; now the interest focuses on describing the performance of new typologies derived from CFT, capable of improving their structural response.

Some of the investigations presented before have become authentic references for new researchers, for their renowned quality and precision. This is the case of (Hu, et al., 2003), (Schneider, 1998), (O'Shea, et al., 2000) and (Susanta, et al., 2000). Due to the importance of the behavior of concrete in the global compressive response, two of the previously mentioned studies deal with concrete strength and its softening period. O'Shea, Bridge and Susantha focused their efforts on describing the increment of strength and ductility of the concrete filling, in case of circular and rectangular steel tubes. As it can be observed in figure II.24, the results obtained by O'Shea contribute to know about the confinement ratio on high-strength concretes [of 50 and 100 MPa strengths, suitable for heavily loaded columns]. Some years after, also (Liang, 2009) investigated about the performance of high-strength concrete-filled tubes specifically.

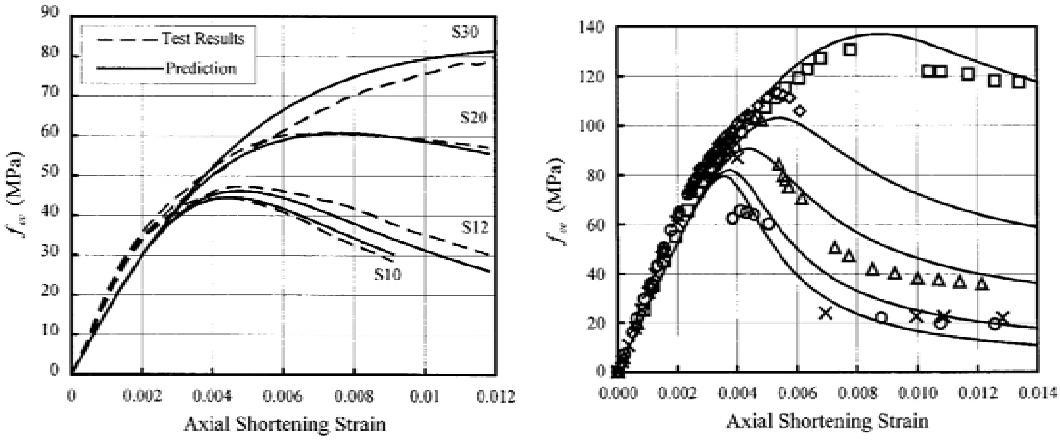

Fig. II.24 Stress-strain experimental curves of high-strength concrete specimens.
(O'Shea, et al., 2000)

On the contrary, Susantha and Ge studied the post-peak behavior of the triaxially loaded concrete of the filling. Their conclusions are really interesting not also for describing and understanding the axial response of CFT sections, but also for defining the plastic softening behavior of concrete under states of high hydrostatic pressures [Figure II.25].

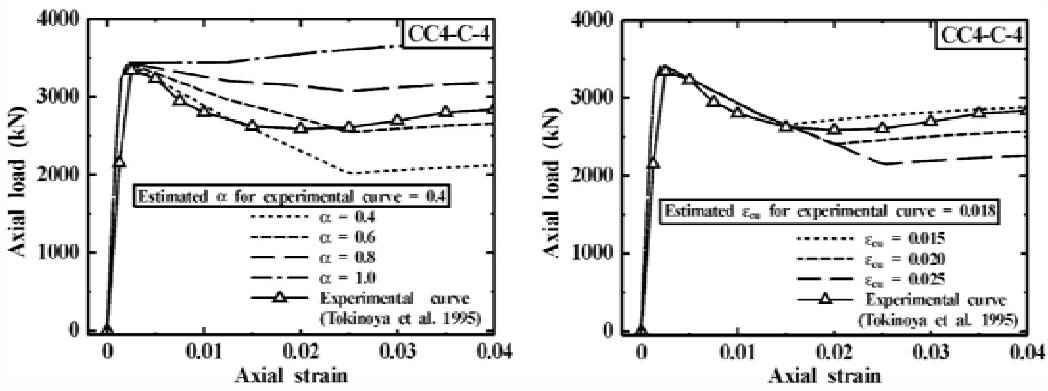

Fig. II.25 Analysis of the post-peak behavior of concrete.
(Susanta, et al., 2000)

Susantha superimposed the experimental curves from other researchers with those coming from his own numerical model of concrete behavior, in order to determine the descending branch slope after the peak of load [Z], and the residual stress after softening [α]. These two values were defined depending on geometry and material strengths, since these two variables clearly govern the hydrostatic state of the core. Curiously, from Susantha's results, it can be observed that really thick-walled tubes do not show almost descending branch; in consequence, the softening period does not take place.

The two mentioned works related with the behavior of concrete deal with short deformation axial loading, enough to describe and calculate the confinement effect provided by the tube; other researchers were also interested in reaching the collapse of these sections, in order to describe their complete ductility. This is the case of (Schneider, 1998), (Choi, 2007), (Yu, et al., 2007) or (Liu, 2006), who carried out several tests with the main purpose of getting the collapse.

a) b) c) d)

Fig. II.26 Failure modes of different circular CFT sections.
(Yu, et al., 2007)

Yu (Yu, et al., 2007) carried out different experimental tests according to diverse ways of loading. For each case, different failure modes were clearly described by following always the same process: the failure of steel first and the collapse of concrete afterwards -by forming a plane of 45º. Figure II.26 shows a set of four different specimens after the collapse, assuming different ways of loading: [a] both materials simultaneously loaded, [b] concrete loaded first, [c] steel loaded first and [d] only concrete loaded -as it is represented in Fig. II.27.

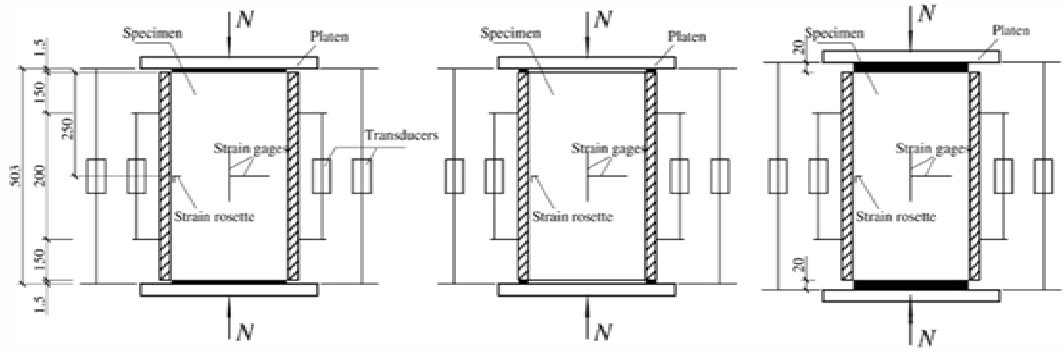

b) c) d)

Fig. II.27 Scheme of the loading ways used in the test.
(Yu, et al., 2007)

As it has been explained in Section 2.3.3 before, the way of loading is really decisive not only for the failure mode, but also for the maximum axial strength. This influence was well quantified by (Yu, et al., 2007) and others, as it is shown in figure II.28; the elastic modulus, the peak of load and also the softening period are affected by the way in which load is applied. The curves shown in figure II.28.a represent the load-strain diagrams for one single specimen, loaded in different ways:

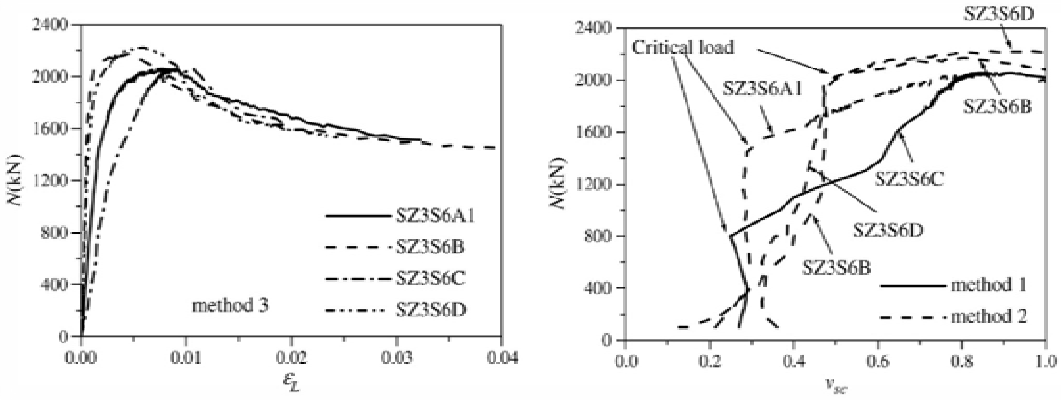

a) Load-strain curves b) Poisson's ratio curves

Fig. II.28 Load-strain diagrams depending on the way of loading.
(Yu, et al., 2007)

Using a collection of experiments, (Choi, 2007) described the mode of failure of CFT sections, depending on the mentioned different ways of loading; in the nearby of the collapse of all CFT sections and independently on the D/t ratio, the steel of the tube tends to suffer from local buckling during the hardening period. In case of having one or two embedded faces, the failure mode of circular-shaped CFT sections follows always the same pattern: the well-known *"elephant foot"* mode of failure [Fig. II.29]:

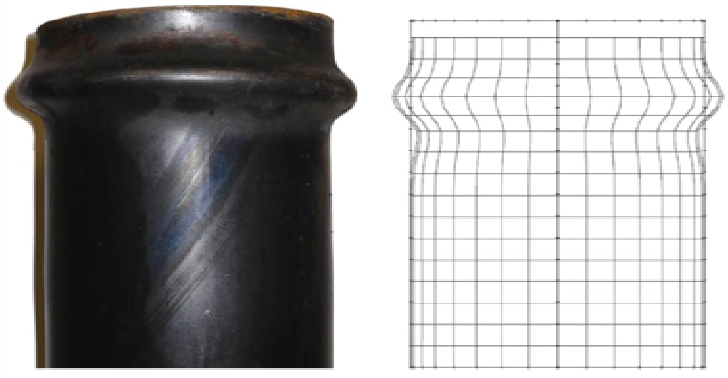

Fig. II.29 Failure mode known as "*elephant foot*", typical in circular CFT sections.
(Choi, 2007)

Besides, lots of specific studies have been also done, related with rectangular and square-shaped CFT sections, such as that carried out by (Liu, et al., 2003). He tested 22 rectangular high-strength specimens under compression. In this case, the investigation focused not only on the increment of compressive strength, but also on the failure modes of different shaped sections. As it has been

explained before, rectangular CFT sections suffer from local buckling effects much earlier than circular sections. An important lack of bending stiffness of the plates leads to a significant deformability in the two cross-sectional axes, a fact that clearly defines the failure mode of the tube; these buckling modes are really different in square-shaped than in rectangular sections, as it was clearly demonstrated by (Liu, et al., 2003) [Fig. II.30].

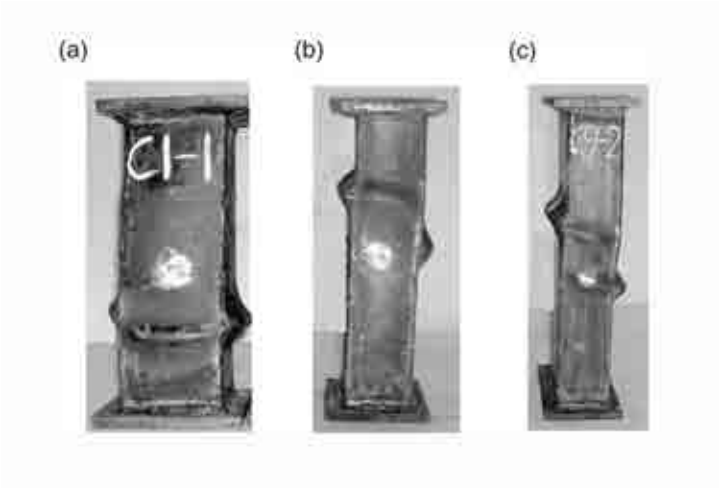

Fig. II.30 Failure modes of different rectangular and square-shaped CFT sections.
Case [a]: B/H=1, Case [b]: B/H=1.5, Case [c]: B/H=2.0. (Liu, et al., 2003)

Needless to say, that the failure mode not only depends on the geometry of the section, but also on boundary conditions. In case of having the specimen pinned at the two loading faces, the failure appears at the middle of its height; in case of embedding only the supporting face, failure then takes place in the nearby of the base.

One of the researchers who have focused his efforts on large deformation axial loading of CFT sections, apart from studying the failure mode, is Schneider (Schneider, 1998). In his paper dated in 1998, there is a collection of different curves coming from large deformation axial loading analyses. To carry out studies of load-strain curves beyond the peak of load is not usual in the existing literature, but nevertheless it is extremely useful to understand the structural capacity of these sections. Figure II.31 shows a set of different load-strain curves published by Schneider, with all singular points where local buckling occurs before the collapse.

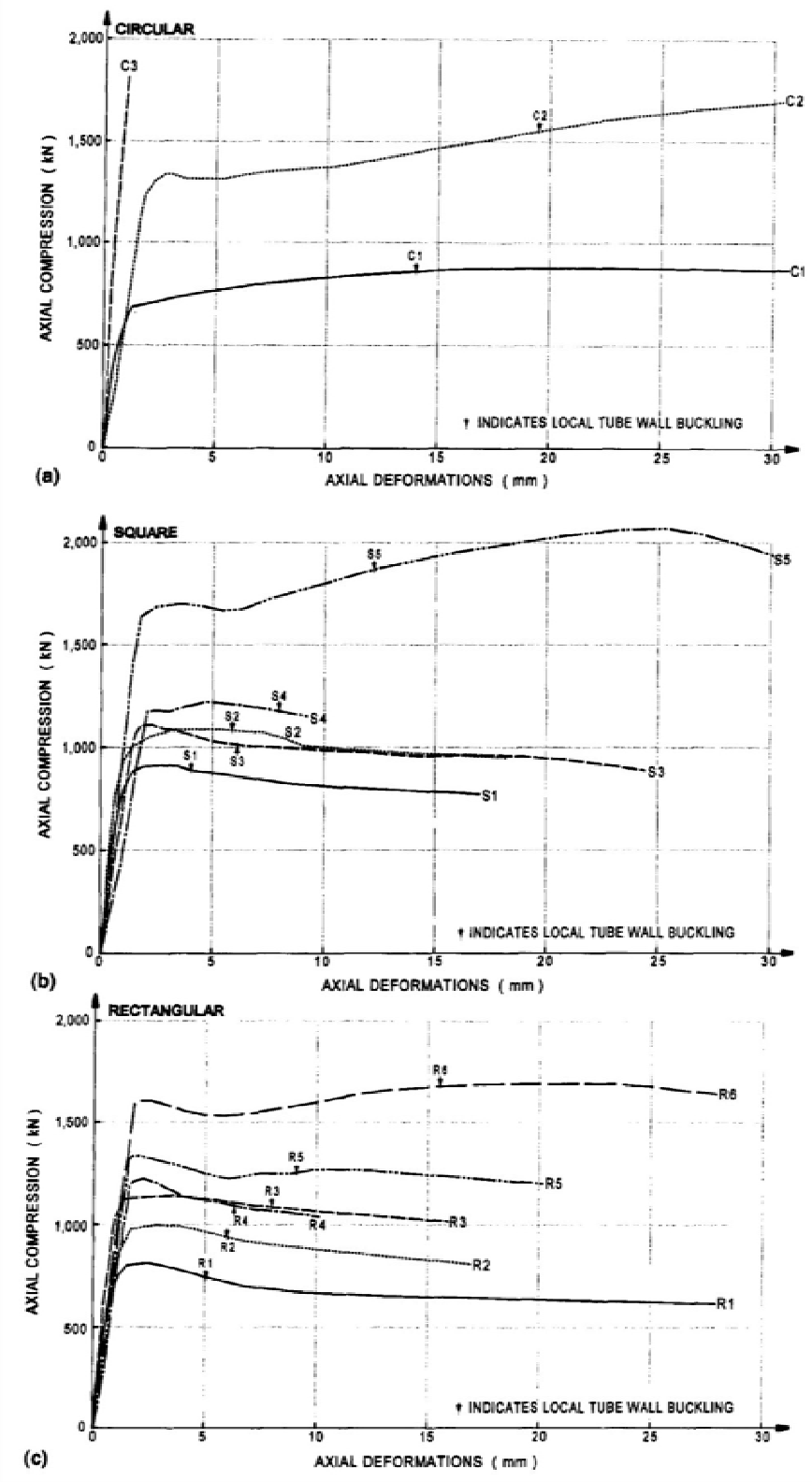

Fig. II.31 Large deformation axial loading tests of CFT sections.
(Schneider, 1998)

2.4.2 Studies about improved typologies derived from CFT sections.

2.4.2.1 Concrete-filled Double Skin Tubes [CFDST[11]]

A first variation of concrete-filled tubes was the introduction of an extra tube inside the core, by generating a new typology: *"concrete-filled double skin tubes"*. This recent typology shows several advantages in comparison with traditional CFT sections, in terms of load-bearing capacity and prevention from buckling. Furthermore, the sandwiched concrete filling becomes also severely confined by the two steel tubes. As in case of single CFT sections, these new sections have been investigated by numerous researchers in these recent years; some of them are (Elchalakani, et al., 2002), (Tao, et al., 2004), (Zhao, et al., 2010) and (Uenaka, et al., 2012). The crescent interest in this typology is derived from their extraordinary applicability, especially in case of heavily loaded columns or bridge piers, located in seismic areas.

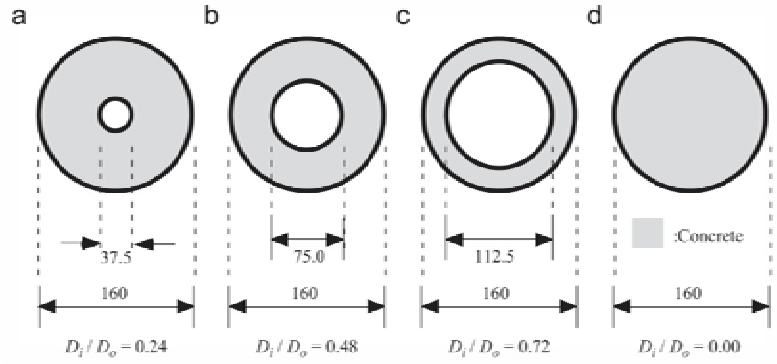

Fig. II.32 Different CFDST typologies proposed.
(Uenaka, et al., 2012)

Researchers from the Monash University were the first to propose and analyze these typologies; Mohammed Elchalakani (Elchalakani, et al., 2002) and Xiao-Ling Zhao (Zhao, et al., 2010) carried out the first numerical and also experimental studies about concrete-filled double skin tubes. One of the most important strengths of CFDST sections is their improved ductility, as the stiffness degradation of the sandwiched concrete is clearly delayed. This is the reason why some of the existing literature about these sections focused on compression tests under large deformation axial loading. As an example, figure II.33 reproduces the behavior of a CFDST until the collapse, carried out by Elchalakani:

[11] Concrete-Filled Doube Skin Tubular sections.

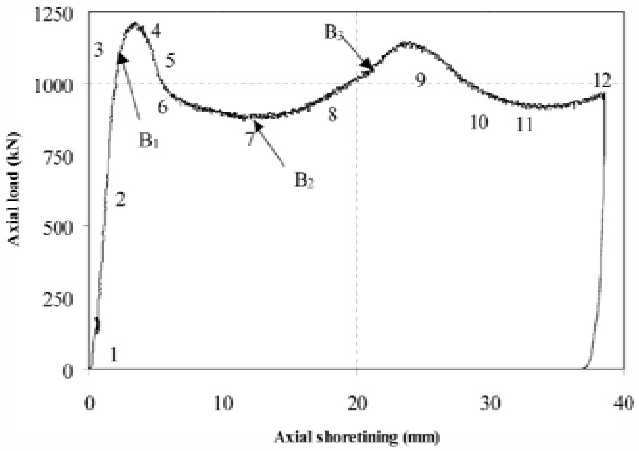

Fig. II.33 Large deformation axial loading test of a CFDST section.
(Elchalakani, et al., 2002)

The analysis done by (Elchalakani, et al., 2002) does not only consist in double skin circular concrete-filled tubes, but also in rectangular-shaped sections and their combinations. The tensional state of components is really different under the assumption of combining a circular outer tube and a rectangular inner tube, than the other way around. It is important to point out that the hoop stress of the inner tube is completely opposite to that of the outer: while the first becomes circumferentially compressed, the latter is circumferentially tensioned according to figure II.34:

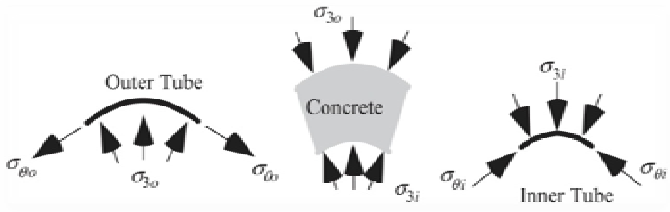

a) Outer tube b) Inner tube

Fig. II.34 Hoop stress in outer tube [a] and inner tube [b].
Elchalakani et al. (2003).

From experimental tests done by Kojiro Uenaka (Uenaka, et al., 2012), it is evident that tensional states of the inner and the outer tube are opposite. In the biaxial diagrams shown below, it can be observed how $\boldsymbol{\sigma_\theta}$ stresses are negative in the first case[12] [figure II.35.a], and positive in the second case [Fig. III.35.b]. The fact of being compressed makes the inner tube susceptible of inward buckling, especially in case of rectangular-shaped sections. This effect was studied by (Elchalakani, et al., 2002) and others, as the principal mode of failure of these sections. Just for this reason, it is convenient to propose the inner profile always thicker than the outer one in order to prevent from buckling.

[12] As in case of simple CFT sections, where circumferential stress is negative, owing to volumetric expansion of concrete.

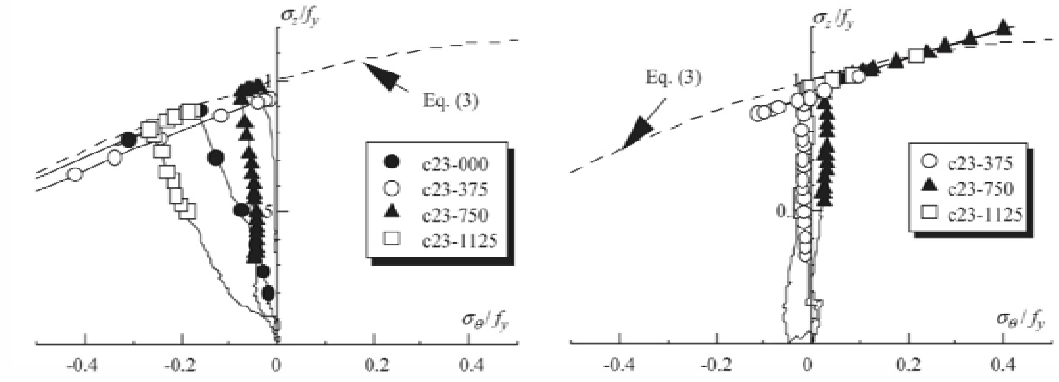

a) b)

Fig. II.35 Stress path in the biaxial plane $(\sigma_\vartheta, \sigma_z)$ of the outer tube [a] and inner tube [b].
(Uenaka, et al., 2012)

One of the most interesting qualities of CFDST sections is the natural fire protection of the inner tube provided by sandwiched concrete, in contrast to the outer tube. In unstiffened CFT sections, the steel is located on the perimeter of the section, being not completely protected against fire as a consequence; this is the reason why many applicative codes require the introduction of reinforcement bars in concrete filling. Thus, what is an apparent disadvantage for CFT sections, can be partially solved by CFDST sections.

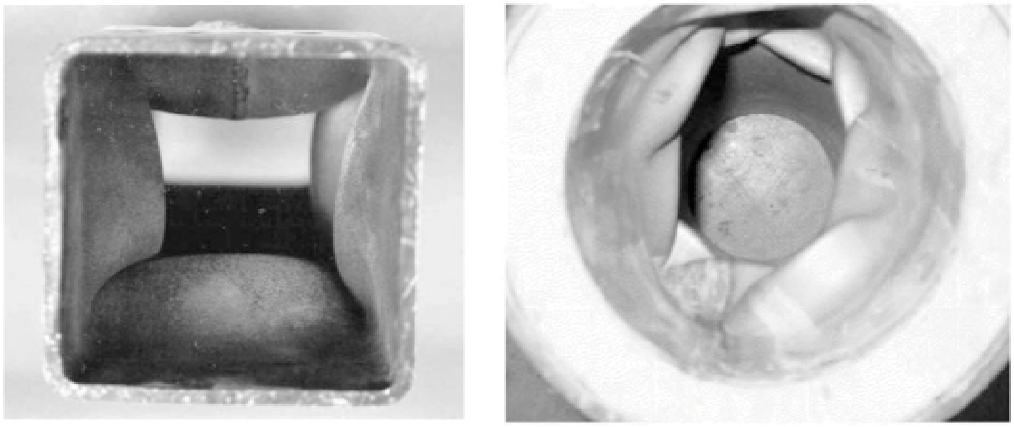

[a] [b]

Fig. II.36 Local buckling of the inner tube, owing to biaxial compression.
(Elchalakani, et al., 2002)

While inward buckling is relatively clear in case of rectangular CFDST sections [case a) of figure II.36], this effect is more complex in case of circular sections [case b) of figure II.36]. Failure takes place in the tube which is more vulnerable -normally the inner, owing to its compressive biaxial state. However, in most cases where both loading faces are completely embedded, the failure follows also the mentioned mode known as *"elephant foot"* [see figure II.37].

Fig. II.37 Collection of tested CFDST specimens with circular and square inner tubes.
(Elchalakani, et al., 2002)

In figure II.37, it can be seen how the collapse goes always after plastic buckling, by following the *"elephant foot"* mode. Depending on the thickness of the tubes, local buckling appears in the nearby of the base or in the middle-height of the samples.

2.4.2.2 Concrete-filled tubes stiffened with bars.

Since one of the most determining factors in reaching the maximum axial load of CFT sections is the deformability of the plates [especially in case of rectangular and square-shaped sections], several derived solutions have appeared in order to improve their flexural stiffness. By improving the rigidity of the plates, concrete of the core becomes more confined, enhancing at the same time the load-bearing capacity of the composite section. This is the reason why different proposals in the line of improving the stiffness of the plates have been proposed these recent years; the first typology is summarized in this Section: CFT sections stiffened with bars.

One of the most studied ways of improving the confinement of concrete filling in a rectangular CFT section is the introduction of stiffening bars in the core. The most important problem of square and rectangular concrete-filled tubes is the excessive deformability of the plates, which clearly limits the confinement effect on concrete core. In order to improve the confinement effect, several researchers have proposed different solutions, based on introducing some individual steel bars at the four edges of the section, fixed at the mid-span of the plates.

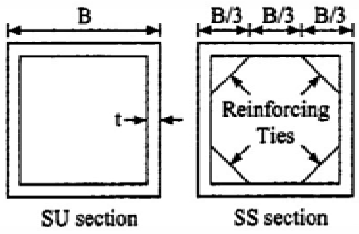

[a] [b]

Fig. II.38 Square-shaped CFT section with and without stiffening bars.
[case a) and b) respectively]
Sections proposed by (Hu, et al., 2003)

Some of the most outstanding researchers who have studied the influence of stiffening bars inside concrete-filled tubes, numerically and experimentally, are: (Huang, et al., 2002), (Hu, et al., 2003), (Liu, et al., 2002), (Nassem Baig, et al., 2006) and (Cai, et al., 2009). The first four have carried out a set of experimental tests on square concrete-filled tubes, with and without stiffening bars; the last one has done a wide analytical study about elastic deformability of the plates, assuming that the four edges are completely restricted against rotation. Results of all these investigations clearly show an important increment in axial load, as a result of the stiffening effect over the plates:

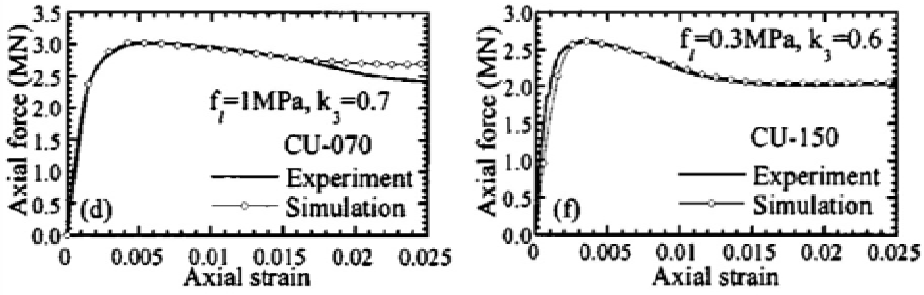

Fig. II.39 Load-Strain diagrams coming from experimental compression tests.
Square-shaped CFT sections, CU-070 and CU-150, without stiffening bars, (Hu, et al., 2003).

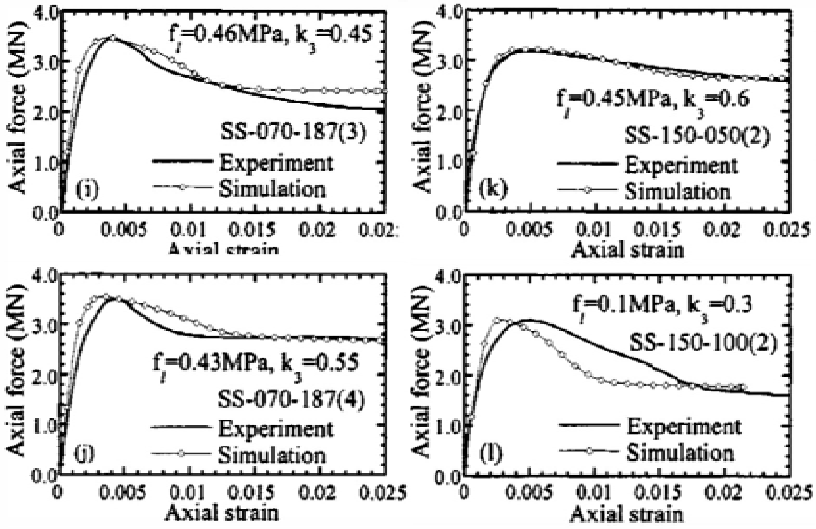

Fig. II.40 Load-Strain diagrams coming from experimental compression tests.
The same sections from figure II.36, but stiffened with bars: SS-070-187(3)/187(4) and SS-150-050(2)/100(29), (Hu, et al., 2003).

From the results presented by (Liu, et al., 2002), it is derived that the structural response of rectangular CFT sections with stiffening bars tends to be similar to the behavior of circular sections. The confinement effect on concrete through the increment of rigidity of the plates has a considerably influence on its maximum resistant strength, as it can be noted in figures II.39 and II.40. The only important disadvantage of introducing these plates is the execution process: as it has been exposed by (Liu, et al., 2002), welding of the bars at the inner face of the plates becomes a complex and slow process, especially for those sections relatively small.

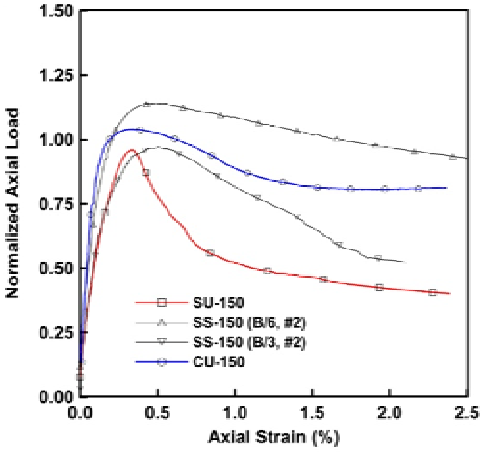

[a] [b]

Fig. II.41 Concrete-filled tubes stiffened with plates
[a] Welding of the proposed stiffening bars at the edges of the tube.
[b] Load-strain curves obtained from experimental tests, with and without stiffening bars, (Liu, et al., 2002)

Obviously, the introduction of these bars in the tube not only improves the confinement effect on the core, but also increases the ductility of the whole section as it can be observed in the curves of figure II.41.b. The softening of concrete after the peak of load is really less important in those cases which include the bars, and also the stiffness degradation of the material diminishes as a consequence. This effect can be observed in figure II.41.b: the red curve corresponds to the specimen SU-150, a square-shaped concrete-filled tube of 300 mm width and 2mm thick, while the blue curve corresponds to a circular specimen of 300 mm diameter, and also 2mm thick. These two tubular specimens are clearly thin-walled, with a B/t ratio over the specified limit of $\mathbf{90} \cdot \boldsymbol{\varepsilon}^2$ proposed by the *Eurocodes* in order to avoid local buckling effects in the plates. The two other curves refer to other specimens stiffened with bars, welded at different heights of B/3 and B/6 from the supporting face. The reduction of the softening period in concrete is explicit in both cases, being much more important in the case of SS-150 [B/6].

Other studies exist in reference to the effects of introducing stiffening bars in partially encased composite columns in order to enhance the confinement effect of the concrete filling. One of these relevant studies is the one carried out by Prickett and Driver in the University of Alberta, Canada (Prickett, et al., 2006).

2.4.2.3 Concrete-filled tubes stiffened with plates

Other new typology derived from CFT sections and much less investigated than those based on stiffening bars, is the one known as *reticulated concrete-filled tubes*: CFT sections with transversal stiffening plates embedded in the core. In addition, these extra plates are usually restricted to buckling by concrete, simultaneously. These sections have not been widely investigated, although they seem to provide exceptional qualities in terms of strength, but especially of ductility. The researchers who have carried out investigations about these typologies are the Japanese T. Yamao (Yamao, et al., 2002) and Wang Zhanfei (Zhanfei, et al., 2011). They propose the introduction of cruciform stiffening plates in the bases of circular and square concrete-filled tubes of bridge piers, especially those located in seismic areas. The existing investigations are numerical and experimental, in reference to dynamic forces by using hysteretic and monotonic tests. The importance of these stiffened sections, according to these two Japanese engineers, comes from the

important increase in ductility. They are especially thought for heavily loaded columns -really useful for those pillars of civil structures like bridges.

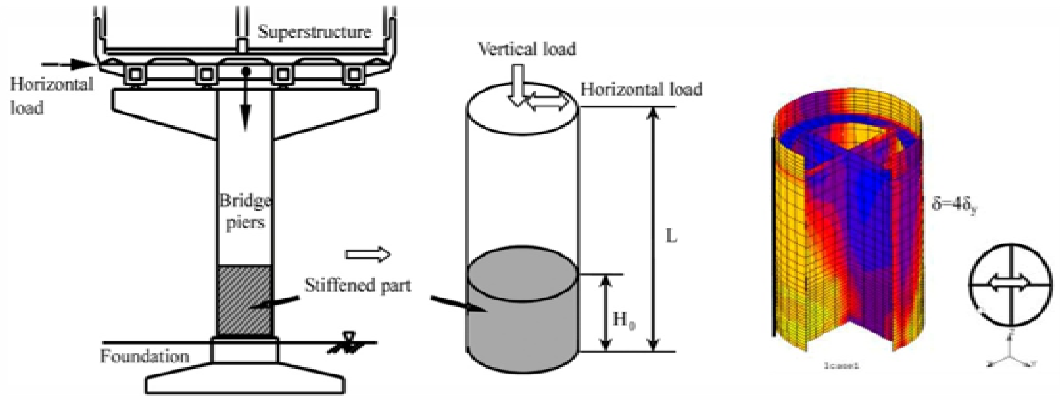

Fig. II.42 Circular cruciform sections in the base of bridge piers, with stiffening plates.
(Zhanfei, et al., 2011)

As it has been previously commented, these studies refer to cyclic loading tests of combined axial and lateral forces, with the aim of determining the behavior of these sections in front of seismic loading. The observed ductility in all cases is considerable, and the stiffness degradation of concrete remains almost constant during the loading-unloading process, beyond the peak of load. This behavior is exceptionally useful in order to lengthen the collapse of large columns subjected to dynamic forces, especially those of seismic areas. The minimization of damage in concrete provided by cruciform sections is a direct consequence of its condition of being contained in individual cells. Obviously, this solution is proposed for the bases of importany columns, since most important appear just in this point.

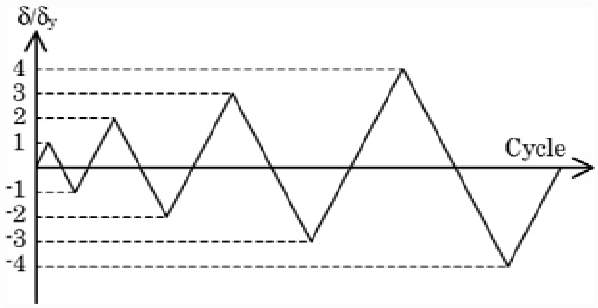

Fig. II.43 Horizontal loading regime applied to specimens.
(Zhanfei, et al., 2011)

In the diagrams shown in figure II.44 below, it can be clearly seen how degradation of the stiffness of concrete beyond the peak of load in case (a) is almost inexistent, while in case (b) and especially in case (d), it takes a significant role. These four cases presented in figure II.41 represent four different solutions to improve the ductility of the connection of bridge piers to foundations, in order to improve the structural response in front of seismic forces. The first one (a) corresponds to the reticulated concrete-filled tube section [with two plates embedded in the core]; the second one (b) corresponds to the case of several short stiffening plates on the internal perimeter of the tube, with the aim of preventing the shell from local buckling; the third one (c) corresponds to a concrete-

filled tube section, surrounded by a thicker steel tube; and the last one [case d)], the simplest case, refers to a concrete-filled tube without reinforcement.

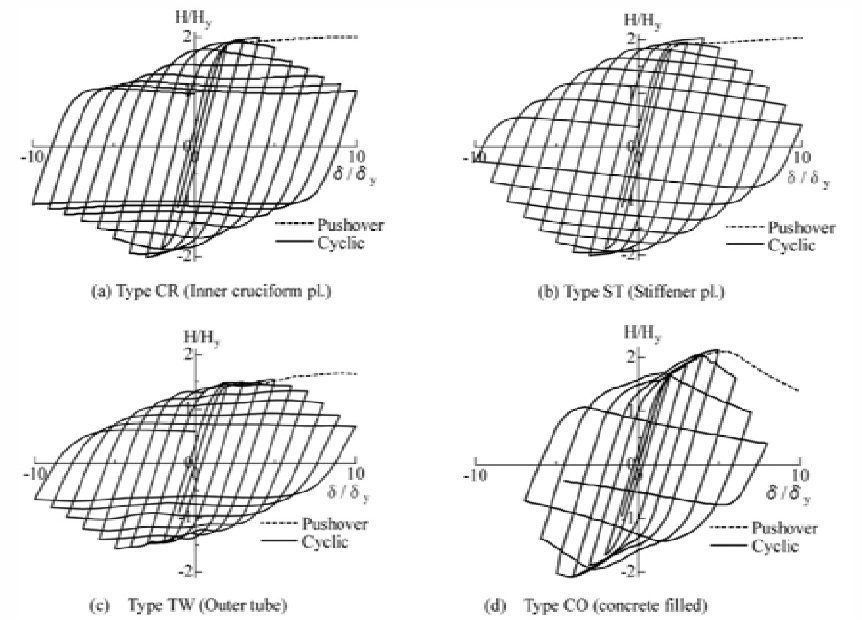

Fig. II.44 Curves of horizontal load depending on horizontal strain of four different specimens experimentally tested.
(Zhanfei, et al., 2011)

This solution based on the introduction of stiffening plates has been studied recently by (Yamao, et al., 2002). They have carried out an experimental investigation, based on cyclic hysteretic tests, by subjecting the specimens to axial and lateral forces simultaneously similar to the procedure used by Zhanfei. The difference between circular and rectangular sections is that the increment of ductility of the second group is less important than this increment in the first one. Although plates of rectangular tubes become stiffened by inner plates, ductility in this case is poorer compared to the ductility observed in circular tubes.

Other possible option would be to achieve the stiffening of the plates through a set of reduced buttresses, welded to the inner surface of the tube, as it was proposed by (Yamao, et al., 2002) [see figure II.45]. This proposal has a clear influence on the degradation of stiffness of the core, as it is derived from diagrams of figure II.46, but it does not improve the shear response of the composite section.

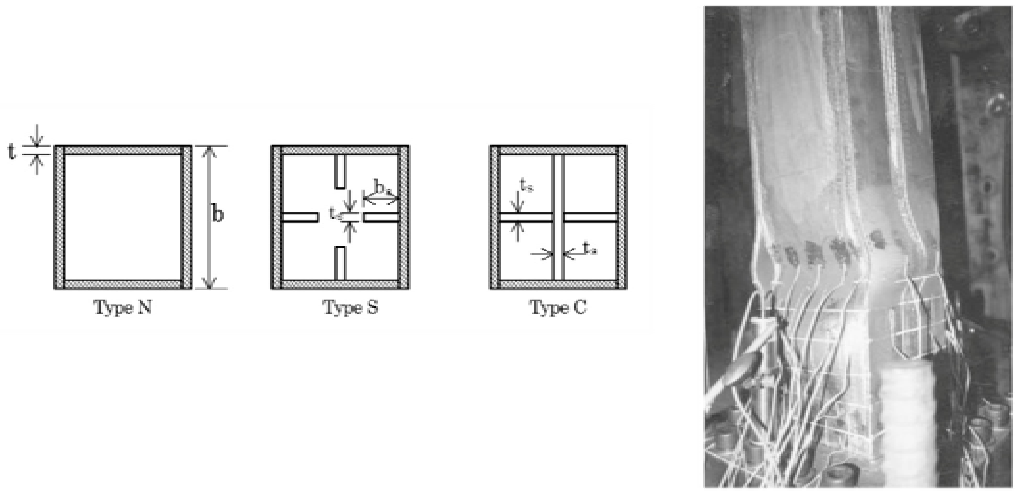

Fig. II.45 Different typologies of rectangular sections with stiffening plates.
Failure mode of a CFT section, stiffened with plates at the base.
(Yamao, et al., 2002)

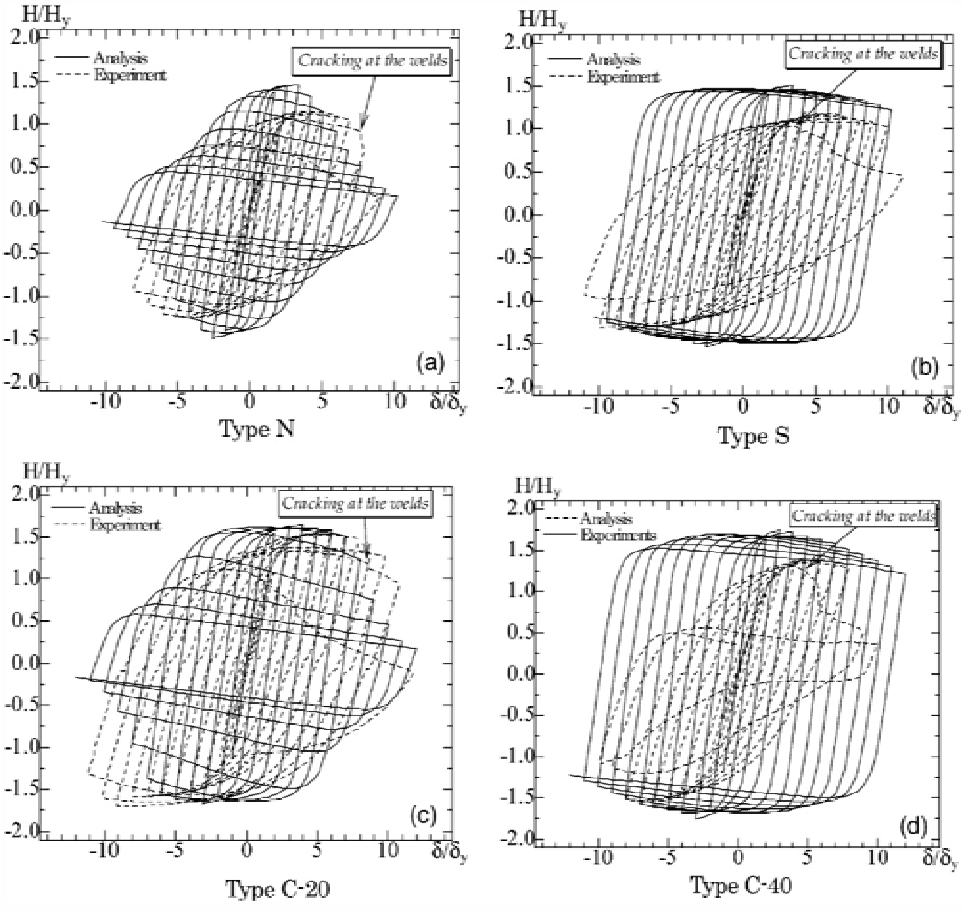

Fig. II.46 Curves of horizontal load depending on strain obtained for typologies shown in figure II.45
(Yamao, et al., 2002)

Chapter III

ELASTIC ANALYSIS OF CONCRETE-FILLED TUBES UNDER COMPRESSION

※※※

This Chapter pretends to present an elastic and analytical analysis of concrete-filled tubes under compression. Obviously, its content does not constitute main body of this work, but it has played a necessary role to develop this research; thus, this is the reason why this study has been included in the text.

The analysis has been separated into two different Sections, one in reference to circular CFT sections and the other related with square-shaped concrete-filled tubes.

An analytical approach is presented for circular sections, according to the Theory of Classical Elasticity; in addition, the obtained expressions have been calibrated thanks to the incremental method, by updating material properties and strengths at each loading step.

This approach is accompanied in the following Sections by the elastic buckling analysis of cylindrical shells and rectangular plates subjected to uniform axial loading. This analysis has been decisive to understand the results provided by the FE models later, although in most cases the plates are thick-walled.

※※※

Chapter III

ELASTIC ANALYSIS OF CONCRETE-FILLED TUBES UNDER COMPRESSION

3.1 Concrete filled tubes under compression.

3.1.1 Nature of the problem.
3.1.2 “Composite section” means “symbiosis” of two materials.
3.1.3 Influence of contact properties
3.1.4 Influence of the way of loading.
3.1.5 Influence of boundary conditions.
3.1.6 Influence of geometry.
3.1.7 Influence of the coordinate system.

3.2 Elastic analysis of circular concrete filled tubes under compression.

3.2.1 Description of behavior.
3.2.2 Approach to the problem [according to Theory of Classical Elasticity].
  3.2.2.1 Elastic approach to the squash load in case [a]: to load the concrete core only.
  3.2.2.2 Elastic approach to the squash load in case [b]: to load both components together.
  3.2.2.3 Elastic approach to the squash load in case [c]: to load the steel tube only.
3.2.3 Practical application of the incremental method to verify the analytical method.
3.2.4 Influence of local buckling in circular CFT sections.
  3.2.4.1 Analysis of buckling of cylindrical shells owing to axial loading.
  3.2.4.2 Analysis of buckling of cylindrical shells owing to axial loading and lateral pressure.
3.2.5 Resistant advantages of introducing stiffening plates in circular CFT sections.

3.3 Elastic analysis of rectangular concrete-filled tubes under compression.

3.3.1 Differences in behavior from circular-shaped sections.
3.3.2 Influence of local buckling in square-shaped CFT sections.
  3.3.2.1 Buckling analysis of rectangular plates owing to axial loading.
3.3.3 Influence of slenderness of the plate on the amplitude of local buckling.
3.3.4 Resistant advantages of introducing stiffening plates in rectangular CFT sections.

3.1 Concrete filled tubes under compression.

3.1.1 Nature of the problem

The final purpose of this Chapter is to carry out an analytic and elastic approach of circular and rectangular-shaped concrete-filled tubes subjected to compression, according to the Classical Theory of Elasticity. The problem is clearly tridimensional, involving non-linear behaviors coming from materials and geometry; consequently, some elemental expressions have been proposed, with the final purpose of approximating the maximum compressive load of these sections analytically.

As it can be derived from the Theory of Elasticity, the problem in rectangular and circular sections is clearly characterized by its axial-symmetry. This fact implies double symmetry on the two axes of the section, by reducing considerably the complexity of the elastic formulation. This is the reason why this problem can be condensed into a bi-dimensional analysis, assuming that the column is infinite and that both materials remain always in contact[1]. This assumption makes possible to carry out an analytic study of these typologies, starting with two of the three coordinates involved in the 3-D problem only.

As instability plays a crucial role on results in thin-walled plates, an elastic buckling approach of cylindrical shells and rectangular plates will be also presented in this Chapter. Needless to say that boundary conditions and the way of loading have also a decisive influence in the buckling response.

3.1.2 "Composite section" means "symbiosis" of two materials.

There is no doubt that the term "composite" is applied to sections which are formed by two or more different materials. This means that both components have to work together to give a unique global response in front of specific forces. In case of composite sections made of concrete and steel generally, it is evident that both materials need to be located so that their resistant qualities can be maximized; in concrete-filled tubes, not only their compressive strengths are fully exploited, but also they can be even improved in case of concrete. This is a clear example of a mechanical symbiosis between two materials, appealing to the coalition between two different organisms in wild nature, in where both parts make profit of it.

When we talk about composite sections, we assume that mechanical properties of these sections differ from those of concrete or steel: composite sections behave really different. The combination of both parts generates new mechanical properties, such as a new elastic modulus or a new Poisson's coefficient. Consequently, we can say that a conjunction of two materials generates "*new constitutive behaviors*", being considered as "*new theoretical materials*" (Martínez Calzón, et al., 1978). This investigation pretends to describe the behavior of these two materials acting together, especially the case of concrete contained by a recipient made of steel.

3.1.3 Influence of contact properties.

In order to guarantee the advantages provided by this mechanical symbiosis, it is crucial to have a perfect interaction between the two materials involved. Providing that both materials have to work together, the responsibility of assuring a global response lies entirely on contact surfaces. This contact is composed by two different components: one normal component which defines whether

[1] This aspect will be commented in further Sections.

concrete is in contact or not to the tube, and a tangential component which defines the value of friction forces of the interface.

With the aim of proposing a simplified and analytic resolution to the problem, it is necessary to neglect the possibility of frictional sliding, as well as any initial gap between components. This way, both materials are supposed as working together from the beginning, independently of the method used to guarantee this contact -thanks to simple adherence or by using physical connectors.

3.1.4 Influence of the way of loading.

Other decisive factor on the compressive response of composite sections -especially in concrete-filled tubes- is the way of loading, going hand in hand with the capacity of transferring load through the interface, as it has been widely commented in Section 2.3.3.

It is radically different to load only the concrete of the core [case a) of Fig. II.21] than loading both materials simultaneously [case b) of figure II.21] or loading only the steel tube [case c) of Fig. III.21]. In the second and the third cases, contact properties of the interface become crucial in order to guarantee the transference of tangential stresses, while in the first case this contact is relatively less important. Loading only the concrete core [a] guarantees a correct bond between concrete and steel from the beginning, owing to lateral expansion of the first. This is not so evident in the second case [b], where both materials are loaded simultaneously by resisting different percentages of axial load; this is basically the reason why tangential stresses of the interface are really important under this assumption. Finally, in case [c] the transference of load becomes even more decisive, since the unique material which is loaded is the steel. In that case, the tube expands laterally according to its Poisson's ratio, and the core is loaded only if connectors are finally disposed.

3.1.5 Influence of boundary conditions.

In the list of starting conditions to carry out this analysis, we can find also boundary conditions, obviously. As it has been commented in Section 4.1.1, the proposed typologies accomplish the condition of axial-symmetry; this condition allows solving the problem through a bi-dimensional "slice" of the column, capable of deforming on the radial axis but completely restricted against displacement and rotation on the symmetry plane. In conclusion, far from considering the two loading faces completely embedded, this analysis proposes the study of a theoretical slice of the section, as a part of a theoretical infinite column.

3.1.6 Influence of geometry.

The behavior of circular CFT sections is really different from the behavior of those square-shaped, as it is widely explained in Chapter VI of this text. Assuming that a bi-dimensional elastic simplification is enough accurate for the case of circular sections, the irregular distribution of stress in a square-shaped cross-section implies a much more complex analysis. This is basically the reason why the analytical approach is presented for circular CFT sections only.

3.1.7 Influence of the coordinate system.

With the final objective of reducing the complexity of the problem, it is convenient to work with a specific coordinate system which can work efficiently with the needs of the process. For square and rectangular sections, it is obvious that the coordinate system used is the Cartesian, with the three coordinates x, y, z. In contrast, for those geometries generated by a revolution axis, the most suitable coordinate system is the Cylindrical [Fig. III.1], where the three Cartesian coordinates,

x, y, z, are replaced by r [radial], θ [circumferential] and z [vertical]. This way, all circular stresses and strains can be expressed in a simpler way. Then, the cylindrical coordinate system has been used only for circular CFT sections, while the Cartesian system has been used for the rest.

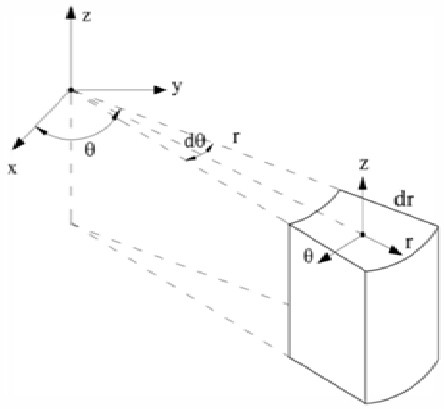

Fig. III.1 Cylindrical coordinate system.
A cylindrical coordinate system has been used for circular-shaped CFT sections.

3.2 Elastic analysis of circular concrete-filled tubes under compression.

3.2.1 Description of behavior.

In circular concrete-filled tube sections, the transference of load from one component to the other during the loading process plays a decisive role in the comprehension of their structural compressive behavior. As it has been commented in other Chapters before, the behavior of each material forming the composite section is considerably different: on the one hand, steel behaves completely linear until the 80% of its yield limit stress, whereas concrete shows basically a non-linear response, with the initiation of its plastic hardening period at a value of the deformation of the 50% of its characteristic compressive strength.

3.2.2 Approach to the problem [according to Theory of Classical Elasticity].

According to the criteria commented in the previous Section, three analytical approaches have been proposed in this Chapter, regarding the loading cases [a], [b] and [c] of figure II.21 presented before. In all cases, friction forces have not been considered: the first case is simple, as it considers that concrete is the only loaded component, while steel is circumferentially stressed. Contrarily, the second case is much more complex, since it requires considering the compatibility of deformations, being both materials simultaneously loaded. And in the third case, the steel is the only loaded component.

For the three different hypotheses of loading, two different assumptions can be done: the first considers that no friction forces and adherence exist between the steel tube and the core. Thus, perfect longitudinal sliding of components is allowed, but without no possibility of transferring load. Under the second assumption, contact in the interface between both materials is considered perfect, so that they work together with full compatibility of deformations, independently of how this contact is achieved.

3.2.2.1 Elastic approach to the squash load in case [a]: to load the concrete core only.

In case [a] of loading circular CFT sections [see Fig. III.2], where the only loaded component is concrete, a simplified bi-dimensional analysis in the cross-sectional plane is possible thanks to the axial-symmetry of the problem and to the uniformity of lateral pressure provided by the tube. This analysis can be easily done only under the assumption that friction forces do not act on the interface and that both materials are perfectly in contact. Otherwise, both components would be quickly loaded, and the analysis would become really more complex.

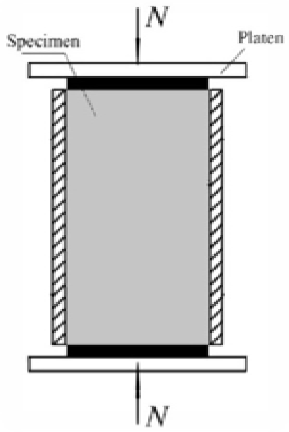

Fig. III.2 Case [a] of loading, only concrete core is loaded
No friction forces on the interface have been considered.

Under this loading assumption, and considering no friction forces on the interface, we can say that the horizontal component of lateral pressure is equal to the maximum circumferential tensile force, resisted by the tube [equation (3.1)]. Contrarily, vertical components of this pressure are compensated themselves thanks to the effect of circular geometry. This way, concrete expands laterally owing to dilatancy, providing to the tube a tensile circumferential stress state. According to (Susantha, et al., 2000), the apparent Poisson ratio [ν'_e] of damaged concrete at the peak of load can be obtained by using the following expressions (3.1) and (3.2) [both expressions have been obtained experimentally]:

$$\nu_e = 0.2312 + 0.3582 \cdot \nu'_e - 0.1524 \cdot \left[\frac{f_c}{f_y}\right] + 4.843 \cdot \nu'_e \cdot \left[\frac{f_c}{f_y}\right] - 9.169 \cdot \left[\frac{f_c}{f_y}\right]^2 \qquad \textbf{(3.1)}$$

$$\nu'_e = 0.881 \cdot 10^{-6} \cdot (D/t)^3 - 2.58 \cdot 10^{-4} \cdot (D/t)^2 + 1.953 \cdot 10^{-2} \cdot (D/t) + 0.4011 \qquad \textbf{(3.2)}$$

Thus, and according to figure III.3, lateral pressure of the core to the tube is expressed by:

$$f_r = \beta \cdot \left(\frac{2t}{D-2t}\right) \cdot f_y \qquad \textbf{(3.3)}$$

Where β is defined as the difference between the Poisson's ratio of concrete and steel:

$$\beta = \nu'_e - \nu_a \qquad \textbf{(3.4)}$$

being:

f_r *Lateral pressure on concrete core.*
ν'_e *Apparent Poisson's ratio of concrete [normally between 0.80 and 1.00]*

ν_a *Plastic Poisson's ratio of steel [0.50]*
D *Outer Diameter*
t *Thickness of the steel tube.*
β *Coefficient of lateral expansion,* $(\nu_e' - \nu_a)$.

This assumption can only be done, assuming that pressure is uniformly distributed over the perimeter of the core as a consequence of the circular geometry:

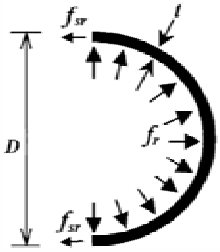

Fig. III.3 Pressure is uniformly distributed on concrete core.
The uniformity and the axial-symmetry of the problem make this 2-D analysis possible.

In case of CFT sections with large D/t ratios [formed by relatively thin plates] this approach is not valid, as local buckling of the tube occurs. Knowing the value of the maximum lateral pressure on the core, the increment of compressive strength experimented by concrete can be calculated through the expression (2.19), proposed by Richart (Richart, et al., 1928). Then, the maximum compressive strength of concrete can be obtained through:

$$f_{cc} = f_c + m \cdot f_r \qquad \textbf{(2.19)}$$

being *m* a scalar coefficient ranging from 4.0 to 4.1, and defined experimentally by Richart.

In this case, concrete of the core is triaxially compressed, while the steel of the tube becomes only circumferentially tensioned[2], so that the axial response of the first could be calculated through the previous expression; the axial response of steel is neglected, since no friction forces are considered. Then, the squash load of the composite section would be:

$$N_{pl,Rd} = A_c \cdot f_{cc} \qquad \textbf{(3.5)}$$

$$N_{pl,Rd} = A_c \cdot \left[f_c + m \cdot \beta \cdot \left(\frac{2t}{D - 2t} \right) \cdot f_y \right] \qquad \textbf{(3.6)}$$

In case of disposing connectors on the interface or considering friction forces between components instead, the previous analytical approach would not be valid since the steel would resist also part of the axial load from the beginning. In case of assuming a perfect bond between components, it would be necessary to propose another more complex analysis, closer to case [b] of loading, as it has been commented before.

[2] Thanks to not considering friction forces between components.

3.2.2.2 Elastic approach to the squash load in case [b]: to load both components together.

By analyzing the situation of loading the two components simultaneously, it is also convenient to consider a perfect bond on the interface; however, a perfect compatibility of vertical deformations must be also assumed, contrarily to the case commented in the previous Section. Nevertheless, all the expressions proposed in this approach are obtained so that sliding or friction forces are not considered; otherwise, few differences on results would be detected.

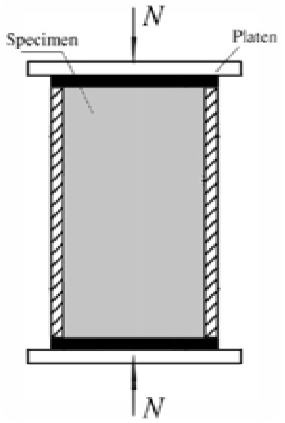

Fig. III.4 Case [b] of loading, both components loaded simultaneously.
A perfect bond between components is assumed.

The proposed approach starts with the assumption of two cylinders, one solid [concrete] and the other hollow, but thick-walled [steel tube]; the two cylinders are axially loaded as it is shown in Fig. III.4. They are not subjected to radial pressures, and temperature is considered constant or without significant influence on the system. Assuming that the initial Poisson's ratio is different for each component, contact pressure quickly appears on the interface as a consequence of the existing difference in radial and circumferential strains of both materials. Therefore, the concrete core becomes subjected to a triaxial stress state: apart from vertical stress, radial and circumferential components also appear, owing to its perfect unity with the tube. The criterion for determining if a stress state is triaxial or not is based on the proportion between components: if radial and circumferential stresses are infinitely small compared with those vertical, it deals with a uniaxial case.

The height of both cylinders $[L_c, L_a]$ is known and at the same time, equivalent. They are axially loaded, considering that heights and strains are completely identical. This way, the axial strain of both materials is equivalent, by following the principle of compatibility of deformations:

$$\varepsilon_{z,c} = \varepsilon_{z,a} \tag{3.7}$$

In a triaxial stress state and according to the Hooke's Law, axial strains of the two cylinders take the following form:

$$\varepsilon_{z,i} = \frac{\sigma_{z,i} - \nu_i\left(\sigma_{r,i} + \sigma_{\theta,i}\right)}{E_i} \tag{3.8}$$

replacing the particularized expression (3.8) in the equation (3.7):

$$\frac{\sigma_{z,c} - \nu_c\left(\sigma_{r,c}\{\rho\} + \sigma_{\theta,c}\{\rho\}\right)}{E_c} = \frac{\sigma_{z,a} - \nu_a\left(\sigma_{r,a}\{\rho\} + \sigma_{\theta,a}\{\rho\}\right)}{E_a} \tag{3.9}$$

where:

$\sigma_{r,c}\{\rho\}$ *Radial stress in the ρ coordinate*
$\sigma_{\theta,c}\{\rho\}$ *Circumferential stress in the ρ coordinate*

From Classical Theory of Elasticity[3], it can be derived that radial and circumferential stresses in a cylinder take the following form [according to the Lamé equations]:

$$\sigma_r\{\rho\} = A - B \cdot \frac{1}{\rho^2} \quad \text{and} \quad \sigma_\Theta\{\rho\} = A + B \cdot \frac{1}{\rho^2} \tag{3.10}$$

being the coefficients A and B:

$$A = \frac{p_{inn} \cdot r^2 - p_{out} \cdot R^2}{(R^2 - r^2)} \quad \text{and} \quad B = \frac{(p_{inn} - p_{out}) \cdot r^2 \cdot R^2}{(R^2 - r^2)} \tag{3.11}$$

p_{inn} *Inner pressure of the cylinder*
p_{out} *Outer pressure of the cylinder*
R *Outer radius*
r *Inner radius*

and the sum of radial and circumferential stresses is independent of the radius:

$$\sigma_r\{\rho\} + \sigma_\Theta\{\rho\} = 2 \cdot A \tag{3.12}$$

Since stresses are independent of the radius, the expression shown before is valid for any value of the radius $\{\rho\}$. Assuming that during the construction process the system is not subjected to internal or external pressures, a new equation can be obtained through introducing expressions (3.11) and (3.12) in equation (3.9),:

$$\frac{\sigma_{z,c}}{E_c} + \frac{2 \cdot \nu_c \cdot p_c \cdot R_c^2}{E_c \cdot (R_c^2)} = \frac{\sigma_{z,a}}{E_a} - \frac{2 \cdot \nu_a \cdot p_c r_a^2}{E_a \cdot (R_a^2 - r_a^2)} \tag{3.13}$$

where:

p_c *Contact pressure.*

In equation (3.13) there are three unknown values: $\sigma_{z,c}$, $\sigma_{z,a}$ and p_c. This is the reason why it is necessary to look for two more equations, in order to convert this undetermined system into determined. The second equation can be obtained from the static equilibrium, by considering that axial stresses are distributed uniformly in the cross section:

$$F = \pi \cdot \sigma_{z,c} \cdot R_c^2 + \pi \cdot \sigma_{z,a} \cdot (R_a^2 - r_a^2) \tag{3.14}$$

using this last equation, two different expressions can be obtained:

[3] (Timoshenko, et al., 1961)

$$\sigma_{z,c} = \frac{F \cdot E_c - 2 \cdot \pi \cdot p_c \cdot \left(\nu_c \cdot R_c^2 \cdot E_a \cdot \frac{A_a}{A_c} + \nu_a \cdot r_a^2 \cdot E_c\right)}{(A_c \cdot E_c + A_a \cdot E_a)} \quad \textbf{(3.15)}$$

$$\sigma_{z,a} = \frac{F \cdot E_a - 2 \cdot \pi \cdot p_c \cdot \left(\nu_c \cdot R_c^2 \cdot E_a + \nu_a \cdot r_a^2 \cdot E_c \cdot \frac{A_c}{A_a}\right)}{(A_c \cdot E_c + A_a \cdot E_a)} \quad \textbf{(3.16)}$$

Up to now, axial stresses have been obtained depending on one unknown variable only, p_c [contact pressure], since the other parameters are already known. This is the reason why to obtain a third equation will be necessary to solve the problem. This third equation will be obtained by using the assumption that contact before deformation persists -in the ideal system to which we are referring. While the gap between both materials is zero in the beginning,($R_c = r_a$), after deformation we have:

$$\Delta r_a = \Delta R_c \quad \textbf{(3.17)}$$

Δr_a *Increment of inner radius, steel tube.*
ΔR_c *Increment of outer radius, concrete core.*

In case of losing the contact bond between the two surfaces, contact pressure would vanish and the triaxial stress state would be converted into a uniaxial state.
According to Partaukas (Partaukas, et al., 2007):

$$\Delta\rho = \rho \cdot \varepsilon_\theta\{\rho\} \quad \textbf{(3.18)}$$

ρ *Radius*
$\Delta\rho$ *Increase of radius*
$\varepsilon_\theta\{\rho\}$ *Circumferential strain in the coordinate* ρ

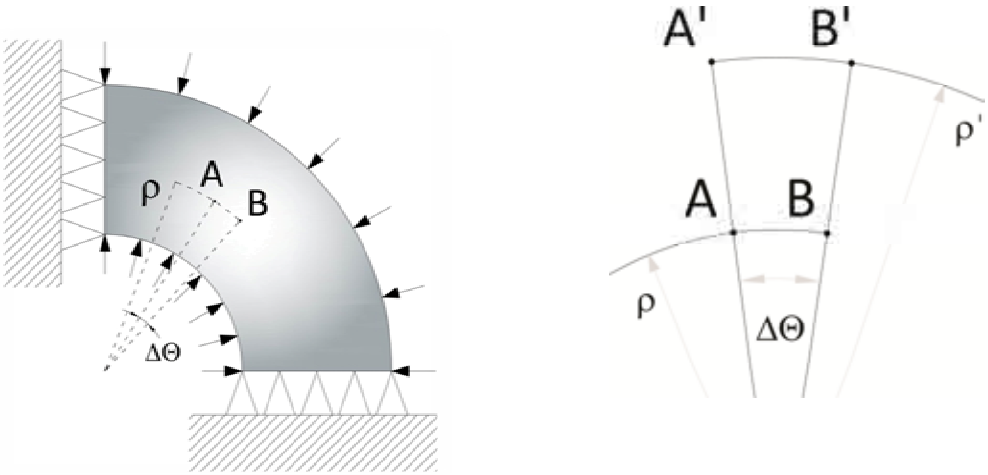

Fig. III.5 Deformational scheme of a loaded hollow cylinder.
In the presented analysis, inner and outer pressures have been neglected.

From the argument shown before:

$$\varepsilon_{\Theta}^{\rho} = \frac{A'B' - AB}{AB} = \frac{\rho' \cdot d\Theta - \rho \cdot d\Theta}{\rho \cdot d\Theta} = \frac{\Delta\rho}{\rho} \qquad \textbf{(3.19)}$$

Then, by replacing the value $\rho = R_c$ and $\rho = r_a$ for each case in the equation (3.17):

$$\Delta R_c = R_c \cdot \varepsilon_{\Theta,c}\{R_c\} \quad \text{and} \quad \Delta r_a = r_a \cdot \varepsilon_{\Theta,a}\{r_a\} \qquad \textbf{(3.20)}$$

being $\varepsilon_{\Theta,c}\{R_c\}$ and $\varepsilon_{\Theta,a}\{r_a\}$ the circumferential strains in the coordinates R_c and r_a:

$$r_a \cdot \varepsilon_{\Theta,a}\{r_a\} - R_c \cdot \varepsilon_{\Theta,c}\{R_c\} = 0 \qquad \textbf{(3.21)}$$

Then, by replacing the circumferential strains by their specific values, and according to the tridimensional Hooke's law, we can obtain:

$$\frac{r_a}{E_a} \cdot \left[\sigma_{\Theta,a}\{r_a\} - \nu_a \cdot \left(\sigma_{r,a}\{r_a\} + \sigma_{z,a}\right)\right] - \frac{R_c}{E_c} \cdot \left[\sigma_{\Theta,c}\{R_c\} - \nu_c \cdot \left(\sigma_{r,c}\{R_c\} + \sigma_{z,c}\right)\right] = 0 \qquad \textbf{(3.22)}$$

And both radial and circumferential stresses in the two cylinders can be defined by using the Lamé equations (3.10):

$$\sigma_{r,c}\{R_c\} = -p_c \qquad \textbf{(3.23)}$$

$$\sigma_{\Theta,c}\{R_c\} = -p_c \qquad \textbf{(3.24)}$$

$$\sigma_{r,a}\{r_a\} = \frac{-p_c \cdot r_a^2 \cdot R_a^2}{(R_a^2 - r_a^2) \cdot r_a^2} - \frac{p_c \cdot r_a^2}{R_a^2 - r_a^2} = -p_c \qquad \textbf{(3.25)}$$

$$\sigma_{\Theta,a}\{r_a\} = \frac{p_c \cdot r_a^2 \cdot R_a^2}{(R_a^2 - r_a^2) \cdot r_a^2} - \frac{p_c \cdot r_a^2}{R_a^2 - r_a^2} = p_c \cdot \frac{R_a^2 + r_a^2}{R_a^2 - r_a^2} \qquad \textbf{(3.26)}$$

and introducing these expressions in equation (3.22):

$$\frac{r_a}{E_a} \cdot \left(\frac{p_c \cdot (R_a^2 + r_a^2)}{R_a^2 - r_a^2} + \nu_a \cdot p_c - \nu_a \cdot \sigma_{z,a}\right) - \frac{R_c}{E_c} \cdot \left(-p_c + \nu_c \cdot p_c - \nu_c \cdot \sigma_{z,c}\right) = 0 \qquad \textbf{(3.27)}$$

Finally, a system composed by 3 equations and 3 unknown variables can be obtained:

$$\begin{cases} \sigma_{z,c} = \dfrac{F \cdot E_c}{\pi \cdot (b_c + b_a)} - \dfrac{2 \cdot p_c \cdot E_c \cdot b_a}{b_c + b_a} \cdot d & \textbf{(3.28)} \\ \sigma_{z,a} = \dfrac{F \cdot E_a}{\pi \cdot (b_c + b_a)} + \dfrac{2 \cdot p_c \cdot E_a \cdot b_c}{b_c + b_a} \cdot d & \textbf{(3.29)} \\ p_c = \dfrac{-a_c \cdot \sigma_{z,c} + a_a \cdot \sigma_{z,a}}{c_c + c_a} & \textbf{(3.30)} \end{cases}$$

Where parameters **a, b, c** and **d** are defined by:

$$a_c = \frac{\nu_c \cdot R_c}{E_c} \quad ; \quad a_a = \frac{\nu_a \cdot r_a}{E_a} \quad ; \quad b_i = E_i \cdot (R_i^2 - r_i^2) \tag{3.31}$$

(3.32)

(3.33)

$$c_{i,0} = \frac{R_i^2 + r_i^2}{b_i} - \frac{\nu_i}{E_i} \quad ; \quad c_c = c_{i,0} \cdot R_c \quad ; \quad c_a = c_{i,0} \cdot r_a \quad ; \quad d = \frac{\nu_c \cdot R_c^2}{b_c} + \frac{\nu_a \cdot r_a^2}{b_a} \tag{3.34}$$

(3.35)

(3.36)

Finally, the previous system can be expressed depending on the force *F* and the set of variables shown before, by replacing the value of p_c:

$$\left\{ \begin{array}{l} \sigma_{z,c} = \dfrac{F \cdot E_c \cdot [2 \cdot a_a \cdot E_a \cdot d - (c_c + c_a)]}{2 \cdot \pi \cdot d \cdot (a_c \cdot E_c \cdot b_a + a_a \cdot E_a \cdot b_c) - \pi \cdot (b_c + b_a) \cdot (c_c + c_a)} \\ \sigma_{z,a} = \dfrac{F \cdot E_a \cdot [2 \cdot a_c \cdot E_c \cdot d - (c_c + c_a)]}{2 \cdot \pi \cdot d \cdot (a_c \cdot E_c \cdot b_a + a_a \cdot E_a \cdot b_c) - \pi \cdot (b_c + b_a) \cdot (c_c + c_a)} \\ p_c = \dfrac{F \cdot [E_c \cdot a_c - E_a \cdot a_a]}{2 \cdot \pi \cdot d \cdot (a_c \cdot E_c \cdot b_a + a_a \cdot E_a \cdot b_c) - \pi \cdot (b_c + b_a) \cdot (c_c + c_a)} \end{array} \right\} \tag{3.37}$$

(3.38)

(3.39)

The equations of vertical stress in both components $[\sigma_{z,c}, \sigma_{z,a}]$ and the equation of contact pressure, p_c, have been expressed depending on a set of different known parameters. It is important to point out that these expressions are strictly based on an elastic formulation, so that the application of these equations for concrete implies accepting an elastic approach for a problem, essentially plastic.

Finally, the expressions of circumferential and radial stresses can be also easily obtained, by replacing the value of p_c in equations (3.23) to (3.26):

$$\left\{ \begin{array}{l} \sigma_{r,c} = \dfrac{-F \cdot [E_c \cdot a_c - E_a \cdot a_a]}{2 \cdot \pi \cdot d \cdot (a_c \cdot E_c \cdot b_a + a_a \cdot E_a \cdot b_c) - \pi \cdot (b_c + b_a) \cdot (c_c + c_a)} \\ \sigma_{\Theta,c} = \dfrac{-F \cdot [E_c \cdot a_c - E_a \cdot a_a]}{2 \cdot \pi \cdot d \cdot (a_c \cdot E_c \cdot b_a + a_a \cdot E_a \cdot b_c) - \pi \cdot (b_c + b_a) \cdot (c_c + c_a)} \\ \sigma_{r,a} = \dfrac{-F \cdot [E_c \cdot a_c - E_a \cdot a_a]}{2 \cdot \pi \cdot d \cdot (a_c \cdot E_c \cdot b_a + a_a \cdot E_a \cdot b_c) - \pi \cdot (b_c + b_a) \cdot (c_c + c_a)} \\ \sigma_{\Theta,a} = \dfrac{F \cdot k_a \cdot [E_c \cdot a_c - E_a \cdot a_a]}{2 \cdot \pi \cdot d \cdot (a_c \cdot E_c \cdot b_a + a_a \cdot E_a \cdot b_c) - \pi \cdot (b_c + b_a) \cdot (c_c + c_a)} \end{array} \right\} \tag{3.40}$$

(3.41)

(3.42)

(3.43)

being k_a a proportional ratio between the radiuses of the steel tube:

$$k_a = \frac{(R_a^2 + r_a^2)}{(R_a^2 - r_a^2)} \tag{3.44}$$

r *Inner radius.*

Finally, and with the objective of calibrating the obtained expressions, the unknown variables can be particularized for solid circular concrete-filled tubes, assuming that both components are initially in contact:

$$r_a = R_c \qquad \textbf{(3.45)}$$

$$r_c = 0 \qquad \textbf{(3.46)}$$

$$t = R_a - R_c \qquad \textbf{(3.47)}$$

This way, the maximum compressive load of a concrete-filled tube by supposing both components simultaneously loaded and with no sliding forces on the interface, could be calculated through the expressions (3.37) to (3.38), in reference to the vertical stress of components.

3.2.2.3 Elastic approach to the squash load in case [c]: to load the steel tube only.

By assuming the last case [c] and also neglecting friction forces on the interface, two options are possible. First possibility is to have both components initially together, without connectors on the interface: under this assumption, each material deforms separately [more steel that concrete] and confinement effect never occurs. The second possibility is to suppose a perfect bond between the two components, without sliding on the interface, so that both materials work absolutely together.

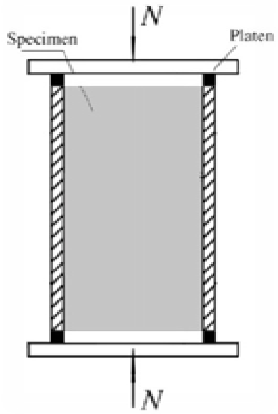

Fig. III.6 Case [c] of loading, only the steel tube is loaded
A perfect bond between the two components is assumed.

By considering the first assumption, only the steel tube is loaded with no confining pressure or load transference to the core; steel expands according to its Poisson's ratio [0.289], while concrete remains completely unloaded. This way, the contact between the two components vanishes from the beginning. Thus, the maximum axial load of the section would be the plastic compressive capacity of the steel tube only, as it works alone.

Otherwise, under the second assumption, both materials are simultaneously loaded thanks to the perfect interaction between them, so that the composite section behaves similar to the case [b], where both materials are loaded together from the beginning. Thus, the maximum compressive load would be obtained by following the same approach.

Different would be the hypothesis of assuming a friction coefficient and a certain capacity of sliding between components. Then, the elastic analysis would become really more complex, and the FE method would be a necessary alternative.

3.2.3 Practical application of the incremental method to verify the analytical method.

For calibration purpose, an incremental iterative manual analysis has been carried out for a specific CFT section in order to validate the expressions proposed before. This way, although concrete clearly has a plastic behavior, an elastic manual approach is presented below by updating its mechanical properties depending on hydrostatic pressure and strain.

With the objective of describing the axial response of CFT sections analytically, and to calibrate the expressions of Section 3.2.2.2, experimental results of specimen CC4-A-4[4] have been used. This specimen is a circular-shaped CFT section with 148.9 mm diameter and 2.96 mm wall-thickness. Experimental results have been compared to the analytical ones, coming from an incremental elastic procedure. Material nonlinearities and effects of confinement on concrete core have been updated at each load increment in order to obtain the most accurate results as possible, close to those results obtained experimentally.

Table III.1. Material and geometrical features of CC4-A-4

Section	D*	t*	f_c**	f_{y}**
CC4-A-4	**148.9**	**2.90**	**40.5**	**283**

All values expressed in mm* and N/mm^2**.

It is important to point out that all the expressions proposed before come from the assumption that both components are jointly bound, and that sliding does not occur in the interface as it has been mentioned in several occasions before:

$$\varepsilon_z = \varepsilon_{z,c} = \varepsilon_{z,a} \qquad \textbf{(3.48)}$$

The constitutive laws for materials used in this analysis correspond to those simplified models explained in Chapter II; the behavior of the triaxially compressed concrete has been replaced by a simple pressure-sensitive curve (2.16) proposed by Popovics (Popovics, 1973), and mentioned in Section 2.2.4. Contrarily, for the behavior of steel, the uniaxial stress-strain curve together with the evolution of the Poisson's ratio and the Young's modulus in the elastic-plastic range have been used [expressions (2.3) and (2.4)] proposed by Kuranovas (Kuranovas, et al., 2009). The behavior of steel has been considered elastic perfectly-plastic: until the 80% of its yield limit stress, the material is governed by a linear function from which point it changes to parabolic up to yielding [expression (2.4)]. To simulate the plastic flow of steel, the von Mises yield criterion has been implemented, according to equation (2.9).

The value of f_{cc} corresponding to the maximum confined compressive strength of concrete in expression (2.19) has been modified at each load step, depending on lateral pressure provided by the tube and according to the Poisson's ratio of concrete, which is given by the expression (3.49) proposed by Susantha and Ge (Susantha, et al., 2000):

$$\nu'_e = 0.881 \cdot 10^{-6} \cdot (D/t)^3 - 2.58 \cdot 10^{-4} \cdot (D/t)^2 + 1.953 \cdot 10^{-2} \cdot (D/t) + 0.4011 \qquad \textbf{(3.49)}$$

[4] Results presented by (Susantha, et al., 2000).

With the objective of solving a nonlinear problem through an incremental elastic approach, the load has been applied in 40 different partial steps. These steps have been introduced as vertical strain increments in order to control the tensional state of the components. The increments have been considered larger at the beginning [as it corresponds to a linear period] and smaller later, in order to be as much accurate as possible [ranging from 0.00022 to 0.000055]. The objective is to update the mechanical properties of materials as often as possible to get a realistic curve. In the table III.2, the results of this incremental analysis are shown by different steps.

To obtain the parameter F [Axial Force] in equations (3.37) to (3.43), the following expression has been calculated by updating also the values of E_{ci}, E_{ai} and ε_i at each different load step:

$$F_i = A_c \cdot \varepsilon_i \cdot E_{ci} + A_a \cdot \varepsilon_i \cdot E_{ai} \qquad \textbf{(3.50)}$$

Table III.2. Results obtained from the implementation of the incremental method.

STEP	ε_i	pc0	Δpc	pc	Δσz,c	σz,c	Δσz,a	σz,a	Δσθ,a	σθ,a	σ_{mises}
Eq.			[3.37]		[3.35]		[3.36]		[3.41]		
1	0.000220	0.00	0.21	0.21	6.57	6.57	44.90	44.90	-5.51	-5.51	42.41
2	0.000440	0.21	0.21	0.43	6.47	13.04	44.68	89.58	-5.49	-11.00	84.61
3	0.000660	0.21	0.21	0.64	6.18	19.22	43.87	133.44	-5.39	-16.39	126.05
4	0.000880	0.21	-0.19	-0.19	5.67	24.89	40.15	173.60	4.80	4.80	176.05
5	0.000990	-0.19	-0.19	-0.37	2.20	27.09	18.15	191.75	4.76	9.56	196.70
6	0.001045	-0.19	-0.11	-0.48	0.85	27.94	7.78	199.53	2.81	12.37	205.99
7	0.001100	-0.11	-0.13	-0.61	0.93	28.88	7.15	206.68	3.28	15.65	214.93
8	0.001155	-0.13	-0.15	-0.76	0.86	29.74	7.02	213.70	3.97	19.62	224.15
9	0.001210	-0.15	-0.18	-0.94	0.79	30.53	6.62	220.33	4.50	24.11	233.32
10	0.001265	-0.18	-0.15	-1.09	0.75	31.27	5.24	225.56	3.81	27.92	240.74
11	0.001320	-0.15	-0.13	-1.22	0.76	32.03	4.33	229.89	3.33	31.25	247.00
12	0.001375	-0.13	-0.12	-1.33	0.75	32.79	3.61	233.50	2.97	34.22	252.35
13	0.001430	-0.12	-0.10	-1.44	0.74	33.53	2.97	236.47	2.65	36.87	256.90
14	0.001485	-0.10	-0.09	-1.53	0.73	34.26	2.43	238.91	2.37	39.25	260.75
15	0.001540	-0.09	-0.08	-1.61	0.71	34.97	1.99	240.89	2.13	41.38	264.02
16	0.001595	-0.08	-0.07	-1.69	0.69	35.67	1.61	242.51	1.92	43.30	266.80
17	0.001650	-0.07	-0.07	-1.76	0.68	36.34	1.31	243.82	1.74	45.04	269.18
18	0.001705	-0.07	-0.06	-1.82	0.66	37.00	1.06	244.88	1.58	46.62	271.21
19	0.001760	-0.06	-0.06	-1.87	0.64	37.64	0.86	245.73	1.45	48.07	272.96
20	0.001815	-0.06	-0.05	-1.93	0.62	38.25	0.69	246.42	1.33	49.39	274.47
21	0.001870	-0.05	-0.05	-1.97	0.60	38.85	0.55	246.98	1.22	50.61	275.79
22	0.001925	-0.05	-0.04	-2.02	0.58	39.42	0.44	247.42	1.13	51.74	276.94
23	0.001980	-0.04	-0.04	-2.06	0.56	39.98	0.35	247.77	1.05	52.79	277.95
24	0.002035	-0.04	-0.04	-2.10	0.54	40.51	0.28	248.05	0.98	53.76	278.84
25	0.002090	-0.04	-0.04	-2.13	0.52	41.03	0.21	248.26	0.91	54.68	279.64
26	0.002145	-0.04	-0.03	-2.16	0.50	41.53	0.16	248.42	0.86	55.54	280.35
27	0.002200	-0.03	-0.03	-2.20	0.48	42.01	0.12	248.55	0.82	56.36	281.00
28	0.002255	-0.03	-0.03	-2.23	0.46	42.48	0.09	248.63	0.79	57.14	281.59
29	0.002310	-0.03	-0.03	-2.26	0.45	42.92	0.06	248.69	0.77	57.91	282.14
30	0.002365	-0.03	-0.03	-2.29	0.43	43.36	0.03	248.72	0.78	58.70	282.68

31	0.002420	-0.03	-0.04	-2.33	0.42	43.77	0.01	248.74	0.98	59.68	283.33
32	0.002475	-0.04	-0.03	-2.35	0.41	44.18	-0.01	248.72	0.70	60.37	283.77
33	0.002530	-0.03	-0.02	-2.38	0.39	44.57	-0.02	248.70	0.58	60.95	284.12
34	0.002585	-0.02	-0.02	-2.40	0.37	44.94	-0.03	248.67	0.50	61.45	284.41
35	0.002640	-0.02	-0.02	-2.41	0.35	45.30	-0.04	248.63	0.43	61.88	284.66
36	0.002695	-0.02	-0.01	-2.43	0.34	45.64	-0.04	248.58	0.38	62.27	284.87
37	0.002750	-0.01	-0.01	-2.44	0.32	45.96	-0.05	248.54	0.34	62.61	285.05
38	0.002805	-0.01	-0.01	-2.45	0.31	46.27	-0.05	248.49	0.31	62.92	285.20
39	0.002860	-0.01	-0.01	-2.46	0.30	46.57	-0.05	248.44	0.28	63.20	285.34
40	0.002915	-0.01	-0.01	-2.47	0.28	46.85	-0.05	248.40	0.25	63.45	285.46

The values which are in red correspond to those steps where the contact pressure is compressive, so that confinement effect over the core can occur. Being:

p_c	*Contact pressure*
ε	*Axial strain*
$\Delta\sigma_{z,c}$	*Increment of vertical stress in concrete. This value is obtained from equation (3.35)*
$\sigma_{z,c}$	*Vertical stress in concrete.*
$\Delta\sigma_{z,a}$	*Increment of vertical stress in steel. This value is obtained from equation (3.36)*
$\sigma_{z,a}$	*Vertical stress in steel. This value is obtained from equation (3.35)*
$\Delta\sigma_{\theta,a}$	*Increment of circumferential stress in steel. This value is obtained from equation (3.41)*
$\sigma_{\theta,a}$	*Circumferential stress in steel*

From the analytical study presented before, the following stress-strain curve [Fig. III.7] is obtained up to the yield limit stress of 283 MPa for steel [specimen CC4-A-4]. Note the difference in the sensibility of the steps as strain increases, in order to be capable of describing the nonlinear compressive response. Nonlinearity appears at approximately about the 70% of the maximum yield stress, from which point the Poisson's ratio of concrete grows and the proportional modulus decreases. The final value of the yield limit stress [equivalent stress] of steel is slightly higher than the maximum known value, 283 MPa, mainly owing to the impossibility of assuming a proportional modulus for steel completely zero [it has been considered a really small value instead].

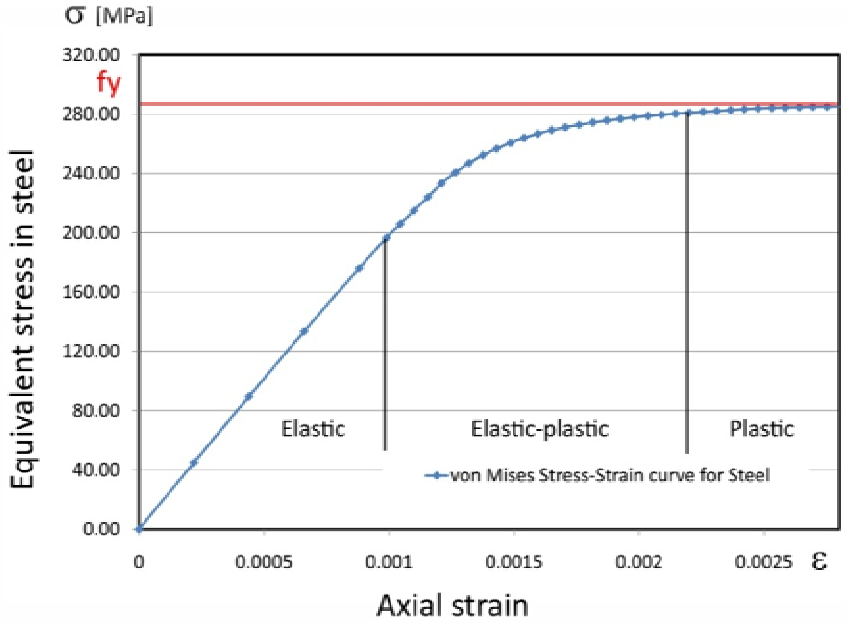

Fig. III.7 Evolution of the equivalent stress in the steel tube.

Steps are reduced when plasticity takes place.

In the diagram of figure III.8, the evolution of the Poisson's ratio adopted for both materials in the analysis is shown, although in case of concrete this value is known as the *apparent Poisson's ratio.* Before stresses of approximately the 50% of the maximum compressive stress of concrete, the material expands transversally according to its elastic Poisson's ratio [0.18-0.20]. Beyond this point, the volumetric expansion grows even more, by increasing this ratio and reaching values higher than 0.50, even 0.80-1.00 of apparent Poisson's ratio. Volumetric expansion of concrete is caused by internal micro-cracking of the cement paste [see Chapter IV of this text and also literature as (Susantha, et al., 2000)].

During this process, steel expands laterally by following its elastic Poisson's ratio [0.289] until a value of 0.5 during plasticity [blue curve]. Since lateral deformation of concrete is more significant than that of steel, the first becomes triaxially compressed by the tube [red curve].

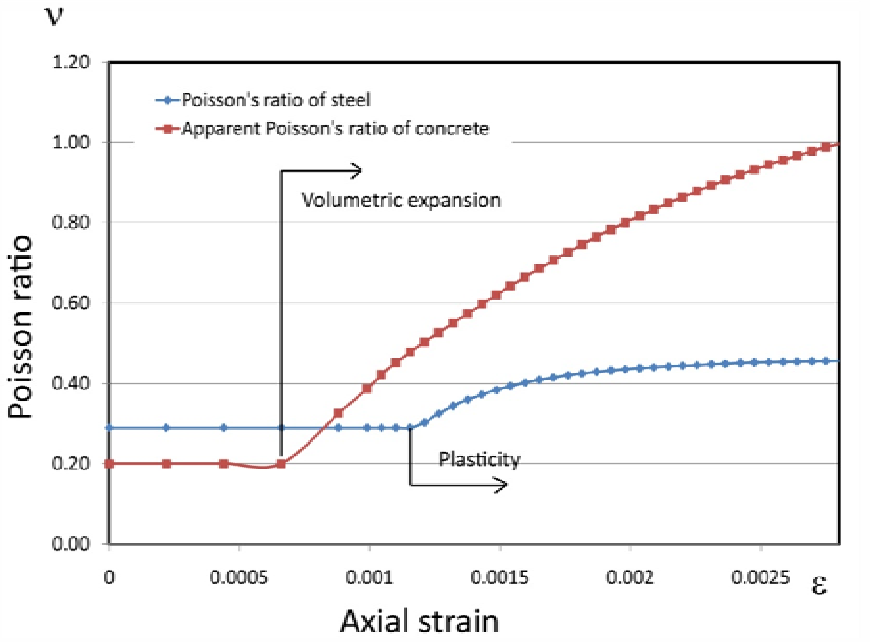

Fig. III.8 Evolution of Poisson's ratio considered for both materials.
(Apparent Poisson's ratio in concrete)

As a consequence of the lateral expansion of concrete, the steel tube becomes biaxially stressed. The tube is circumferentially tensioned and axially compressed simultaneously; this fact reduces its maximum vertical strength owing to the von Mises yield criterion [see figure III.9]. The appearance of circumferential stresses in the tube wall-thickness coincides with the initiation of compressive stresses [$p_c < 0$] in the interface [step 5 of Table III.2]. The reason, why before the 5th step the pressure in the interface is positive, is that in the first stages of loading the tube expands more than concrete of the core. At this stage, the latter becomes circumferentially tensioned.

It is important to point out that the maximum vertical stress of steel does not coincide with its yield limit yield stress [stopping approximately at the 85% of its value], owing to the biaxial state of the tube [$\sigma_1 < 0, \sigma_2 > 0$]. Instead of considering some circumferential compressive stresses in steel during the first stage of loading, owing that steel deforms laterally more than concrete, no chemical or physical adherence has been assumed in the interface.

In figure III.10, the confined stress-strain curve considered in the analysis for concrete is represented, coming from the postulates of Richart. A triaxial stress state on concrete implies an improvement of its maximum compressive strength, according to the well-known expression proposed by Richart (Richart, et al., 1928) and mentioned before. Up to the 50% of its maximum compressive stress, the material can be considered almost linear and elastic; from that point, the proportional modulus decreases progressively and the material behaves completely plastic.

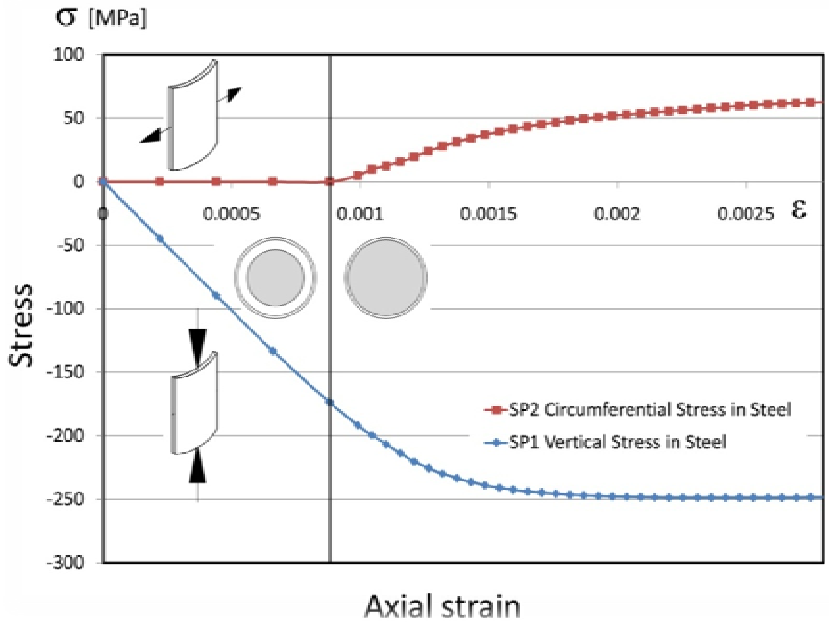

Fig. III.9 Circumferential and vertical stresses obtained in steel.
Curves obtained from the incremental analysis, updating the mechanical parameters.

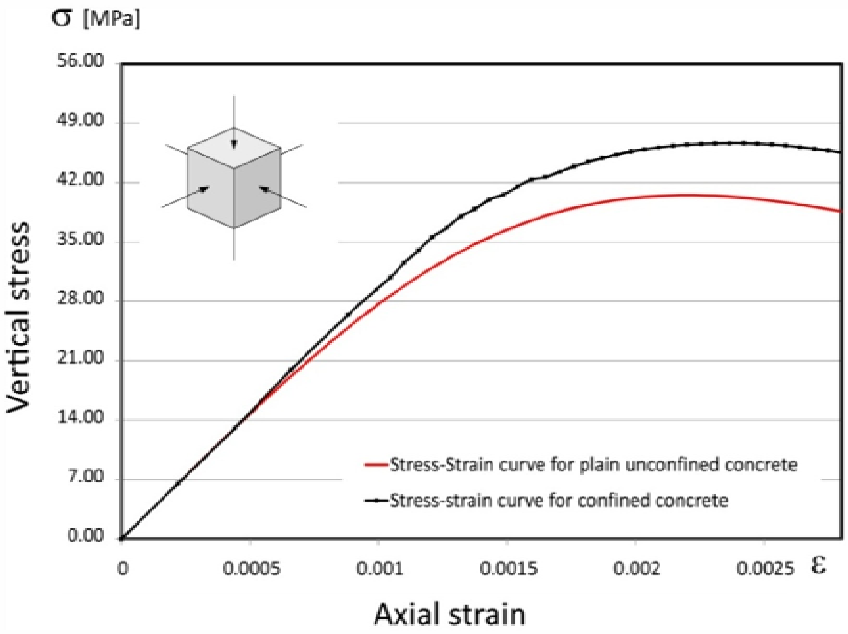

Fig. III.10 Stress-strain curves used for plain and confined concrete of 40 MPa strength.
The curve for confined concrete is pressure-dependant, according to (Richart, et al., 1928).

The maximum compressive confined strength reached by concrete must be determined by the formula of Richart, by using the maximum lateral pressure obtained on the core. Main part of the effective confinement effect on concrete core takes place when steel is already yielding, and this fact implies considering a proportional modulus for steel of zero during this period; since this assumption is not possible in an incremental analysis, the stepping process has been stopped at the 40th. Lateral pressure at this step tends to 2.50 MPa derived from the analysis, being each increment zero or almost zero. Thus, the strength of confined concrete would go on enhancing up to its maximum value f_{cc}, while the von Mises stress of steel would remain constant. Therefore, to determine the maximum vertical strength reached by concrete in the incremental analysis, the formula provided by Richart (Richart, et al., 1928) has been used [as a consequence, vertical stress of concrete will reach a value of 50.60 MPa by keeping the steel tube yielding, instead of the value 46.85 shown in the 40th step of Table III.2].

Finally, the results obtained from this incremental analysis are summarized below:

Table III.3 Comparison of the obtained results.

Method	Axial load*	$f_{z,cc}$**	$f_{z,y}$**	φ	
Incremental	**1080.0**	**50.60**	**243.0**	**1.25**	Albert Albareda, 2012
Experimental	**1147.7**	**53.46**	**226.4**	**1.32**	(Susantha, et al., 2000)

Values expressed in kN* and N/mm^2**.

Being:

$f_{z,cc}$ *Maximum confined vertical stress of concrete*
$f_{z,y}$ *Maximum vertical stress of steel*
φ *Coefficient of confinement,* f_c / f_{cc}

The maximum deviation observed between the value of axial load obtained by the incremental method and that coming from the experimental test is about 5.89 %. The maximum analytical compressive strength of confined concrete [$f_{z,cc}$] is slightly lower than the experimental one; consequently, the circumferential stress of the tube is higher. According to the von Mises yield criterion for steel, as higher is σ_2 lower is σ_1 [circumferential and vertical stresses, respectively]. This deviation can be justified by the approximate apparent Poisson's ratio of concrete considered in the analysis: this value has been determined experimentally from literature, and it has a crucial influence of the final squash load of the specimen.

In the following figure III.11, it is shown the comparison between the load-strain curve obtained experimentally, and the curve coming from the application of the incremental method. The analysis has been done until reaching the yielding of steel [this means a proportional modulus almost horizontal]. The truth is that a Young modulus equal to zero is impossible in a manual approach through an elastic formulation. This is mainly the reason why the analysis has been stopped once the curve has reached a significant flatness. Main divergences between the experimental and the analytical curves come probably from the secant modules considered for concrete in the manual approach.

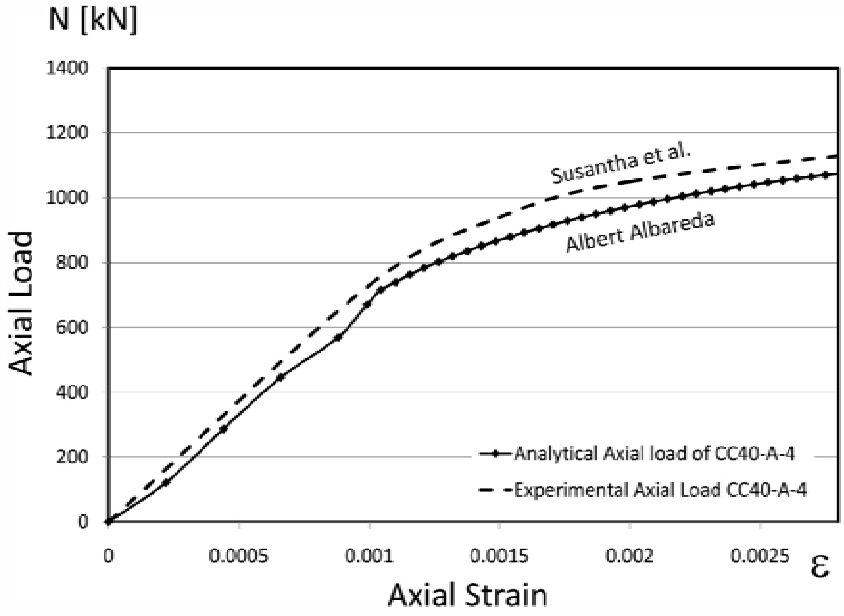

Fig. III.11 Load-strain curve obtained analytically.
This curve belongs to the specimen CC4-A-4, tested by (Susantha, et al., 2000)

3.2.4 Influence of local buckling in circular CFT sections.

Although most part of the specimens analyzed in this investigation do not show local instability problems owing to evident reasons of practical design, an accurate description of this phenomenon is crucial in order to understand and analyze the results obtained from the FE models. Most specimens proposed for the analysis in Chapter VI are clearly thick-walled, although some of them accomplish this condition only considering the stiffening plates inside. However, local buckling also can occur in the plastic period of thick-walled sections beyond the elastic range, by following a similar formulation.

Circular CFT sections are more unlikely to buckle than rectangular ones, as it can be observed from results presented in further Sections. In thick-walled tubes, buckling effects appear only in the plastic range. Instability takes place at advanced stages of loading, becoming a useful warning about the proximity of the collapse. According to the Classical Theory of Elasticity[5], buckling of cylindrical shells follows a sinusoidal function [Fig III.12, a)], talking about the mode of collapse of these sections. For specimens completely embedded in the two loaded edges, the usual mode of failure is the mentioned *"elephant foot"* [Section 2.4.1, Chapter II].

It is important to take into account that elastic buckling occurs only in those thin-walled cylindrical shells. The limit stablished by the Eurocode for thick-walled tubes is:

$$\frac{D}{t} \leq 90 \cdot \varepsilon^2 = 59.57, \quad \text{for steel S275} \qquad \textbf{(3.51)}$$

[5] (Timoshenko, et al., 1961)

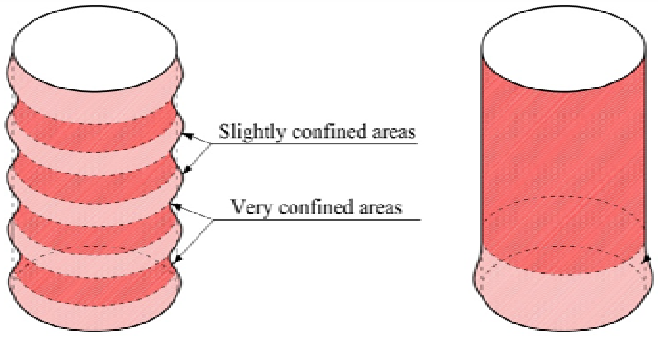

Fig. III.12 Buckling in cylindrical shells
[a] elastic local buckling of thin-walled shells, [b] plastic local buckling, "*elephant foot"*

For usual thicknesses[6], cylindrical tubes do not show buckling problems, and instability does not appear until advanced plastic strains. In this case, it is caused by plastic buckling, becoming much more unpredictable than the elastic one. Commonly, plastic buckling in thick-walled tubes follows a deformed shape known as *"elephant foot*", which usually precedes the collapse of the section [case b) in figure III.12]. Although only the case of elastic buckling is analyzed here, instability of cylindrical shells in plasticity follows a similar pattern, by varying the flexural stiffness of the shell, *D*.

The case of cylindrical shells in CFT sections is clear and completely determined: the tube is subjected to a biaxial stress state, as a result of a combination of axial loading and lateral pressure. Since it is a situation of combined stresses, the mode of buckling will depend on the two components, the way of loading and also the boundary conditions. In case of loading the steel and concrete simultaneously, buckling is caused basically by axial loading. Anyway, the shell remains cylindrical until a critical value of lateral pressure combined with vertical load, from where the equilibrium becomes instable. In the following Sections, the Classical Theory of Elasticity has been used in order to obtain the critical load of cylindrical shells in the elastic range.

3.2.4.1 Analysis of buckling of thin-walled cylindrical shells owing to axial loading.

Firstly, the analysis of buckling is presented by supposing that the cylindrical shell is only axially compressed; under this assumption, the prediction of critical stress is relatively easier than supposing a combined state. The expressions obtained through this simplified analysis are quite accurate, since vertical stresses of the steel tube in CFT sections are really higher than the circumferential ones [approximately 5 times higher]; however, the obtained results overestimate the value of the critical load slightly, as they do not take the effects of lateral pressure into account.

To well understand the origin of the differential equation that governs buckling of a cylindrical shell only subjected to axial loading, the elastic analysis of an infinitesimal cut of a shell subjected to a biaxial state[7] is necessary before all. By using a cylindrical shell of radius r [measured to the middle surface], thickness t and length mn, a unitary strip of a height dx subjected to a force N_x in the [x]

[6] With a D/t ratio, smaller than the value provided by expression (3.46)
[7] Composed by axial load and lateral pressure.

axis and a force qdz normal to the surface, is analyzed. The parameter q represents the value of the internal pressure of the cylinder. All the system is represented in figure III.14; it is important to point out that the force N_x and pressure q are considered both constant. In these conditions, the cylindrical shell is subjected to a uniform compressive stress in the [x] axis, and also a tensile stress in the circumferential axis, represented by the force N_y; the latter will depend on radial strains during the axial shortening and, obviously, on the value of lateral pressure.

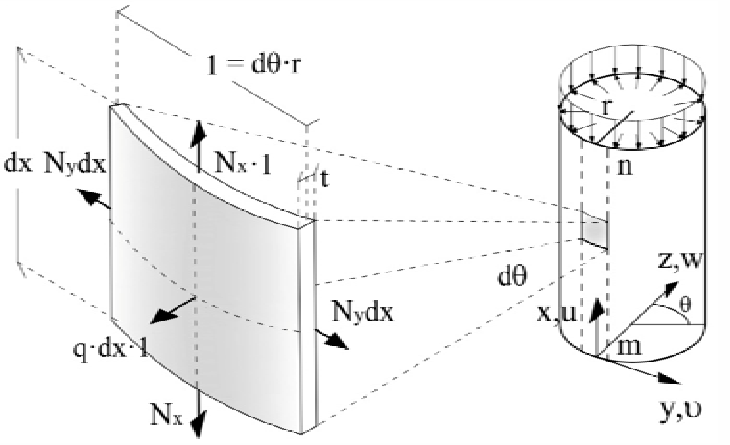

Fig. III.13 Static analysis of a cylindrical shell subjected to a biaxial stress state.
A unitary strip with a length of *mn,* radius *r* and thickness *t* has been considered.

Radial displacements in the shell are represented by the term w, axial displacements by u, and circumferential displacements by υ, according to figure III.13. Thus, by defining axial strains as ϵ_1 ($\epsilon_1 = \epsilon_x$) and circumferential strains as ϵ_2 ($\epsilon_2 = \epsilon_\theta$), the latter can be calculated through:

$$\epsilon_2 = \epsilon_\theta = \frac{-w}{r} \qquad \textbf{(3.52)}$$

From the Classical Theory of Elasticity[8], we know that being σ_x constant across the shell thickness, forces in shells are equal to:

$$N_x = \int_{-t/2}^{t/2} \sigma_x dx = \frac{Et}{1-\nu^2}(\epsilon_1 + \nu\epsilon_2) \qquad \textbf{(3.53)}$$

$$N_y = \int_{-t/2}^{t/2} \sigma_y dx = \frac{Et}{1-\nu^2}(\epsilon_2 + \nu\epsilon_1) \qquad \textbf{(3.54)}$$

then, using these last expressions, and replacing the value of ϵ_2:

$$N_x = \frac{Et}{1-\nu^2}\left(\epsilon_1 - \nu\frac{w}{r}\right) \qquad \textbf{(3.55)}$$

[8] (Timoshenko, et al., 1961)

$$N_y = \frac{Et}{1-\nu^2}\left(-\frac{w}{r} + \nu\epsilon_1\right) \qquad \textbf{(3.56)}$$

where:

r *Radius to the middle of the shell*
t *Thickness*

and combining both expressions, we obtain the following expression:

$$N_y = \nu N_x - \left(\frac{w}{r}\right)Et \qquad \textbf{(3.57)}$$

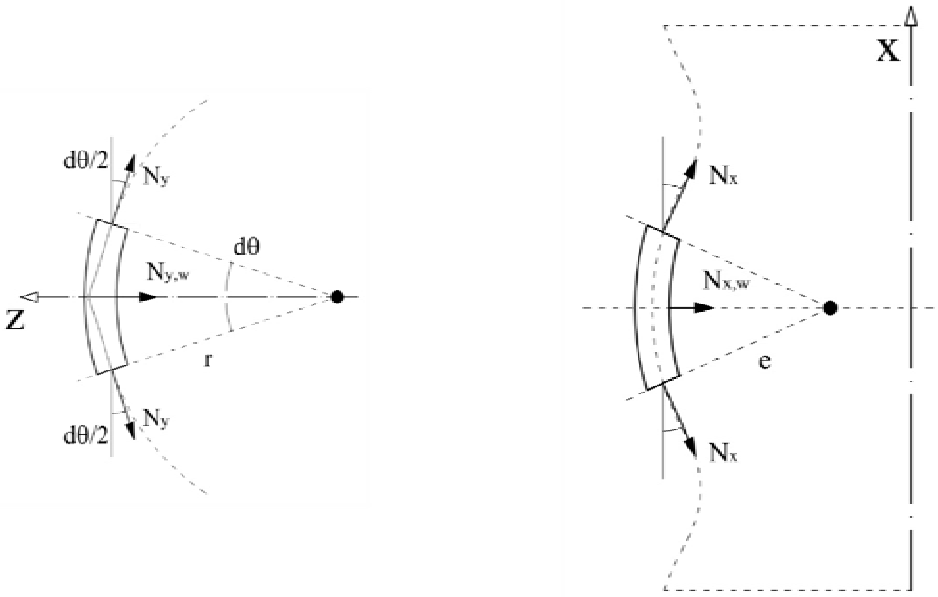

a) b)

Fig. III.14 Obtention of $N_{y,w}$ and $N_{x,w}$ components

Through a bending analysis of the mentioned strip, the force N_y generates a radial component, $N_{y,w}$, whose value per unit length is determined by (see Fig. III.14):

$$N_{y,w} = \frac{N_y}{r} = \frac{1}{r}\cdot\left(\nu N_x - \frac{w}{r}Et\right) \qquad \textbf{(3.58)}$$

being $1/r$ the curvature. Axial force N_x also generates a radial component, $N_{x,w}$, as a result of the curvature of the shell in the [*xz*] plane. Knowing that the change of curvature in the axial plane is:

$$\chi_x = \frac{\partial^2 w}{\partial x^2} \qquad \textbf{(3.59)}$$

The mentioned component of N_x can be obtained through the following expression:

$$N_{x,w} = N_x\frac{d^2 w}{dx^2} \qquad \textbf{(3.60)}$$

Finally, by adding all these transversal forces per unit length together with lateral pressure, it can be derived the following expression:

$$q_{eq} = \frac{d^4w}{dx^4} = q + \frac{1}{r} \cdot \left[\nu N_x - \left(\frac{w}{r}\right) Et\right] + N_x \frac{d^2w}{dx^2} \qquad \textbf{(3.61)}$$

Therefore, the differential equation that governs the bending of a cylindrical shell is:

$$D\frac{d^4w}{dx^4} = q + \frac{1}{r} \cdot \nu N_x - \frac{w}{r^2} Et + N_x \frac{d^2w}{dx^2} \qquad \textbf{(3.62)}$$

where coefficient D refers to the flexural rigidity of the mentioned strip, $D = Et^3/12(1-\nu^2)$. Using this last expression, the deflection of a cylindrical shell can be easily calculated, assuming that axial load and internal pressure are known variables, and supposing that they remain constant.

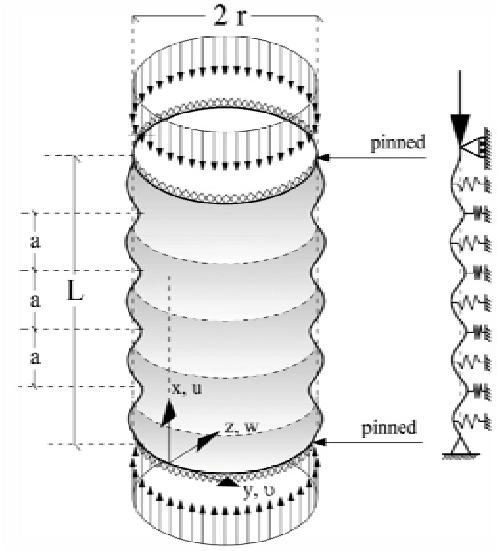

Fig. III.15 Mode of buckling of a cylindrical shell owing to axial loading (q=0).
Similarities between the mode of buckling of cylindrical shells subjected to axial loading and bars embedded in elastic media is observed.

Through the expressions obtained from the static analysis of a biaxially stressed cylindrical shell, the buckling mode can be easily derived assuming that the shell is only subjected to axial loading. Through equation (3.62), and considering that q tends to 0 initially and measuring the displacement ω from the middle surface after having applied the compressive force, the differential equation that governs buckling of a cylindrical shell can be obtained:

$$D \cdot \frac{d^4w}{dz^4} + N_x \cdot \frac{d^2w}{dz^2} + Et\frac{w}{r^2} = 0 \qquad \textbf{(3.63)}$$

The fact of considering the displacement ω after applying the axial load requires to replace displacement ω by $\omega + (\nu \cdot N_z \cdot r)/(E \cdot t)$ and to consider N_z positive, even in compression. From the Theory of Elastic Stability, we know that lateral displacements of a deformed shell follow a sinusoidal equation with amplitude "*A*", similar to:

$$w = A \cdot sin\frac{m\pi z}{l} \qquad \textbf{(3.64)}$$

By replacing ω for its value in equation (3.63), and equating to zero the coefficient $sin\, m\pi z/l$, we can obtain the critical stress of a cylindrical shell under axial pressure:

$$\sigma_{cr} = \frac{N_{cr}}{t} = D\left(\frac{m^2\pi^2}{tl^2} + \frac{E}{Dr^2}\frac{l^2}{m^2\pi^2}\right) \qquad \textbf{(3.65)}$$

Then, by considering that local buckling can occur at several points along the length of the cylinder, and that σ_{cr} is a continue function of $m\pi/l$, the minimum value of this expression [critical stress] can be obtained:

$$\sigma_{cr} = \frac{2}{rt}\sqrt{EDt} = \frac{Et}{a\sqrt{3(1-\nu^2)}} \qquad \textbf{(3.66)}$$

And it occurs at:

$$\frac{m\pi z}{l} = \sqrt[4]{\frac{Et}{r^2D}} \qquad \textbf{(3.67)}$$

Thus, the half wavelength where the shell buckles [assuming, ν = 0.3] coincides with:

$$\frac{l}{m} = \pi\sqrt[4]{\frac{r^2D}{Et}} = \pi\sqrt[4]{\frac{r^2t^2}{12(1-\nu^2)}} \approx 1.72\sqrt{rt} \qquad \textbf{(3.68)}$$

It can be noted that results obtained for symmetrical buckling of cylindrical shells are really similar to those corresponding to a single bar embedded in an elastic media [as it is shown in figure III.15]. It is important to point out again that cylindrical shells are unlikely to buckle in the elastic range, unless they were thin-walled [as it is shown in results presented by Timoshenko (Timoshenko, et al., 1961)]. Besides, the half wavelengths are smaller than one-tenth of the radius, and this means that for a cylinder with a length equal to the diameter, there would appear more than 20 waves. This fact leads to conclude that buckling of circular CFT columns is quite unusual.

Although expression (3.66) provides a good approximation to the critical stress of a cylindrical shell in a CFT section, lateral pressure derived from volumetric expansion of concrete has not been taken into account. It is obvious that the presence of this pressure has a direct effect on the critical stress described above; any existing lateral pressure clearly diminishes this value, since the steel tube becomes biaxially loaded. To determine the differential equation that governs the instability of a cylindrical shell under a combined state of axial loading and lateral pressure, it is necessary to carry out a more accurate analysis [see the following Section].

3.2.4.2 Analysis of buckling of cylindrical shells owing to axial loading and lateral pressure.

As it has been mentioned in the previous Section, to determine a more accurate value of the critical stress of cylindrical tubes in CFT sections, it is also possible to analyze the problem by considering

the combination of uniform axial loading and lateral pressure. To solve this problem, it is necessary to establish first the complete equilibrium of an element cut of a shell [as it is shown in figure III.16]. Before deformation, the Cartesian axes have the directions of the normal axis of the cylinder [*x*], the tangent to the circumference [*y*] and the normal to the middle surface of the shell [*z*]; after deformation[9], these directions change into the tangent to the generator [*x*], the perpendicular to the *xz* plane [*y*] and the normal to the deformed middle surface [*z*].

The process will be based on calculating the angular motions produced by each one of these displacements, and afterwards on calculating the resultant angular displacement by superposition on the element OABC. Rotations of the sides OA and BC with respect to the [x] axis are due to the displacements υ and w; as displacements υ correspond to motion of the sides OA and BC in the circumferential directions and *r* is the radius of the middle surface, the corresponding rotation of the side OA with respect to the *x* axis is υ/r, and the rotation of the side BC according to figure III.16 is:

$$\frac{1}{r}\left(\upsilon + \frac{\partial \upsilon}{\partial x}dx\right) \qquad \textbf{(3.69)}$$

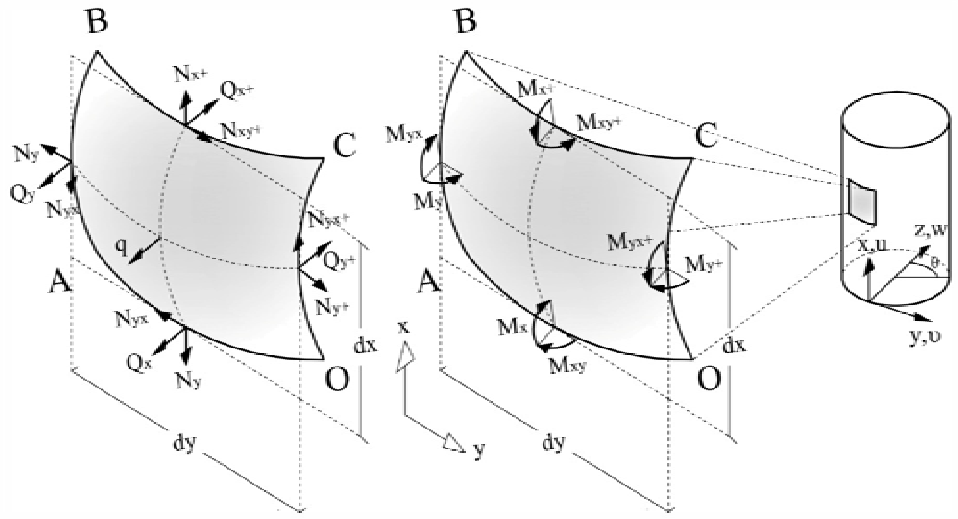

Fig. III.16 Forces and moments in bending of an infinitesimal cylindrical shell cut.
An infinitesimal element cut of a shell from a cylindrical tube of a CFT has been considered.

Owing to displacement υ, the relative angular motion of BC with respect to AO about the [*x*] axis can be obtained through:

$$\frac{1}{r}\frac{\partial \upsilon}{\partial x}dx \qquad \textbf{(3.70)}$$

And owing to the displacement w, the side OA rotates with respect to the [*x*] axis by following the angle $\partial w/r\partial\theta$, and the side BC by following the angle:

$$\frac{\partial w}{r\,\partial\theta} + \frac{\partial}{\partial x}\frac{\partial w}{r\,\partial\theta}\,dx \qquad \textbf{(3.71)}$$

[9] Assumed very small.

Due to displacements w, the relative angular displacement is:

$$\frac{\partial}{\partial x}\frac{\partial w}{r\,\partial\theta}dx \qquad \textbf{(3.72)}$$

By adding the two relative displacements obtained before about the [x] axis:

$$\frac{1}{r}\left(\frac{\partial v}{\partial x}+\frac{\partial^2 w}{\partial x\,\partial\theta}dx\right) \qquad \textbf{(3.73)}$$

The rotation about the [y] axis of the side BC with respect to the side OA is caused by bending of generators in axial planes, and it can be obtained through:

$$-\frac{\partial^2 w}{\partial x^2}dx \qquad \textbf{(3.74)}$$

The rotation about the [z] axis of the side BC with respect to the side OA is caused by bending of the generators in tangent planes:

$$\frac{\partial^2 v}{\partial x^2}dx \qquad \textbf{(3.75)}$$

These last three expressions give the three components of rotation of the side BC with respect to the side OA. It is necessary to obtain also the angular displacement of the side AB with respect to OC. Due to the initial curvature of the shell, there is an initial angle to be considered: $d\theta$. However, this initial angle will be changed due to the displacements v and w; then, the rotation of the lateral side OC with respect to the [x] axis will be:

$$\frac{v}{r}+\frac{\partial w}{r\,\partial\theta} \qquad \textbf{(3.76)}$$

and the rotation of the lateral side AB will be[10]:

$$\frac{v}{r}+\frac{\partial w}{r\,\partial\theta}+\frac{\partial}{\partial\theta}\left(\frac{v}{r}+\frac{\partial w}{r\,\partial\theta}\right)d\theta \qquad \textbf{(3.77)}$$

Therefore, instead of considering the initial angle $d\theta$ for the curvature of the shell, it is necessary to replace this value by adding the rotation of the side AB:

$$d\theta+d\theta\left(\frac{\partial v}{\mathrm{r}\,\partial\theta}+\frac{\partial^2 w}{\mathrm{r}\,\partial\theta^2}\right) \qquad \textbf{(3.78)}$$

The angular displacement about the [y] axis of the side AB, with respect to the side OC:

[10] The signs of the angles with respect to the Cartesian axes are supposed according to the right-hand screw rule.

$$-\left(\frac{\partial^2 w}{\partial\theta\,\partial x}+\frac{\partial v}{\partial x}\right)d\theta \qquad \textbf{(3.79)}$$

The rotation about the [*z*] axis of the side AB with respect to OC is caused by displacements v and w; the rotation of the side OC, owing to displacement v, is $\partial v/\partial x$ and that of the side AB is:

$$\frac{\partial v}{\partial x}+\frac{\partial}{\mathrm{r}\,\partial\theta}\frac{\partial v}{\partial \mathrm{x}}\,\mathrm{r}\,d\theta \qquad \textbf{(3.80)}$$

so that the relative angular displacement is the second term of the last expression:

$$\frac{\partial}{\mathrm{r}\,\partial\theta}\frac{\partial v}{\partial \mathrm{x}}\,\mathrm{r}\,d\theta \qquad \textbf{(3.81)}$$

And, owing to displacement w, the side AB rotates in the axial plane by following the angle $\partial w/\partial x$. The component of this rotation with respect to the [*z*] axis is:

$$-\frac{\partial w}{\partial \mathrm{x}}d\theta \qquad \textbf{(3.82)}$$

and adding the relative rotations of the side AB respect to the [*z*] axis, caused by the displacements v and w:

$$\frac{\partial^2 v}{\partial\theta\,\partial \mathrm{x}}-\frac{\partial w}{\partial \mathrm{x}}d\theta \qquad \textbf{(3.83)}$$

Once all the angles have been already defined through the proposed expressions, the equilibrium of the element OABC can be obtained by projecting the forces on the [*x*],[*y*],[*z*] axes. The forces parallel to the resultant forces N_x and N_{yx} become into $(\partial N_x/\partial x)dxrd\theta$ and $\left(\partial N_{yx}/d\theta\right)d\theta dx$. Thanks to the expression obtained for the rotation of the side AB respect to the [*z*] axis [equation (3.83)], the forces parallel to N_y in the *x* direction become:

$$-N_y\left(\frac{\partial^2 v}{\partial\theta\,\partial \mathrm{x}}-\frac{\partial w}{\partial \mathrm{x}}\right)d\theta\;d\mathrm{x} \qquad \textbf{(3.84)}$$

And, caused by the rotation about the [*z*] axis of the side BC with respect to the OA, the forces parallel to the resultant forces N_{xy} give the following component in the [*x*] direction:

$$-N_{xy}\frac{\partial^2 v}{\partial \mathrm{x}^2}\;d\mathrm{x}\;r\;d\theta \qquad \textbf{(3.85)}$$

In order to finalize, and thanks to the rotation angles about the [*y*] axis of the side BC with respect to the side OA, and about the [*y*] axis of the side AB with respect to the side OC, the forces parallel to Q_x and Q_y give in the [*x*] axis the following components:

$$-Q_x \frac{\partial^2 w}{\partial x^2}\, dx\; r\, d\theta - Q_y \left(\frac{\partial^2 w}{\partial \theta\, \partial x} + \frac{\partial v}{\partial x}\right) d\theta\, dx \qquad \textbf{(3.86)}$$

In the previous elastic analysis, it is assumed that the unique external force acting on element OABC is normal pressure, q, which projection on the [x] axis is zero. By adding all the projections previously calculated:

$$\begin{aligned} &\frac{\partial N_x}{\partial x}\, dx\, r\, d\theta + \frac{\partial N_{yz}}{\partial \theta}\, d\theta\, dx - N_y \left(\frac{\partial^2 v}{\partial \theta\, \partial x} - \frac{\partial w}{\partial x}\right) d\theta\, dx - \\ &-N_{xy} \frac{\partial^2 v}{\partial x^2}\, dx\, r\, d\theta - Q_x \frac{\partial^2 w}{\partial x^2}\, dx\; r\, d\theta - Q_y \left(\frac{\partial^2 w}{\partial \theta\, \partial x} + \frac{\partial v}{\partial x}\right) d\theta\, dx = 0 \end{aligned} \qquad \textbf{(3.87)}$$

And by following the same procedure, two other equations are obtained from the equilibrium of the element. After simplifying terms, it is obtained the following system:

$$r \frac{\partial N_x}{\partial x} + \frac{\partial N_{yz}}{\partial \theta} - r\, Q_x \frac{\partial^2 \omega}{\partial x^2} - r\, N_{xy} \frac{\partial^2 v}{\partial x^2} - Q_y \left(\frac{\partial v}{\partial x} + \frac{\partial^2 w}{\partial \theta\, \partial x}\right) - N_y \left(\frac{\partial^2 v}{\partial \theta\, \partial x} - \frac{\partial w}{\partial x}\right) = 0 \qquad \textbf{(3.88)}$$

$$\begin{aligned} &\frac{\partial N_y}{\partial \theta} + r \frac{\partial N_{xy}}{\partial x} + r\, N_x \frac{\partial^2 v}{\partial x^2} - Q_x \left(\frac{\partial v}{\partial x} + \frac{\partial^2 w}{\partial \theta\, \partial x}\right) + N_{yx} \left(\frac{\partial^2 v}{\partial \theta\, \partial x} - \frac{\partial w}{\partial x}\right) \\ &- Q_y \left(1 + \frac{\partial v}{r\, \partial \theta} + \frac{\partial^2 w}{r\, \partial \theta^2}\right) = 0 \end{aligned} \qquad \textbf{(3.89)}$$

$$\begin{aligned} &r \frac{\partial Q_x}{\partial x} + \frac{\partial Q_y}{\partial \theta} + N_{xy} \left(\frac{\partial v}{\partial x} + \frac{\partial^2 w}{\partial \theta\, \partial x}\right) + r\, N_x \frac{\partial^2 w}{\partial x^2} + N_y \left(1 + \frac{\partial v}{r\, \partial \theta} - \frac{\partial^2 w}{r\, \partial \theta^2}\right) \\ &+ N_{yx} \left(\frac{\partial v}{\partial x} - \frac{\partial^2 w}{\partial x\, \partial \theta}\right) + q\, r = 0 \end{aligned} \qquad \textbf{(3.90)}$$

And finally, it is convenient to obtain the three expressions for moments with respect to the [x],[y] and [z] axes, by taking the angular displacements mentioned before into account:

$$r \frac{\partial M_{xy}}{\partial x} - \frac{\partial M_y}{\partial \theta} - r\, M_x \frac{\partial^2 v}{\partial x^2} - M_{yx} \left(\frac{\partial^2 v}{\partial \theta\, \partial x} - \frac{\partial w}{\partial x}\right) - r\, Q_y = 0 \qquad \textbf{(3.91)}$$

$$\frac{\partial M_{yx}}{\partial \theta} + r \frac{\partial M_x}{\partial x} + r\, M_{xy} \frac{\partial^2 v}{\partial x^2} - M_y \left(\frac{\partial^2 v}{\partial \theta\, \partial x} - \frac{\partial w}{\partial x}\right) - r\, Q_x = 0 \qquad \textbf{(3.92)}$$

$$\begin{aligned} &M_x \left(\frac{\partial v}{\partial x} + \frac{\partial^2 w}{\partial \theta\, \partial x}\right) + r\, M_{xy} \frac{\partial^2 w}{\partial x^2} + M_{yx} \left(1 + \frac{\partial v}{r\, \partial \theta} - \frac{\partial^2 w}{r\, \partial \theta^2}\right) - M_y \left(\frac{\partial v}{\partial x} - \frac{\partial^2 w}{\partial x\, \partial \theta}\right) \\ &+ r\, (N_{xy} - N_{yx}) = 0 \end{aligned} \qquad \textbf{(3.93)}$$

Through the first two equations, it is possible to eliminate Q_x and Q_y from the equations of the equilibrium of forces; this way three equations with six variables left: forces N_x, N_y, N_{xy}, and moments M_x, M_y and M_{xy}.

Using the equations obtained above for the equilibrium of a cylindrical shell cut, it is possible to define the equations that determine buckling in cylindrical shells subjected to combined axial loading and lateral pressure [Fig. III.17]. For that purpose, it is necessary to assume that all forces tend to zero except the vertical N_x component and the circumferential N_y component; then, all the products of these forces by the derivatives of the displacements *u,v* and w will be neglected.

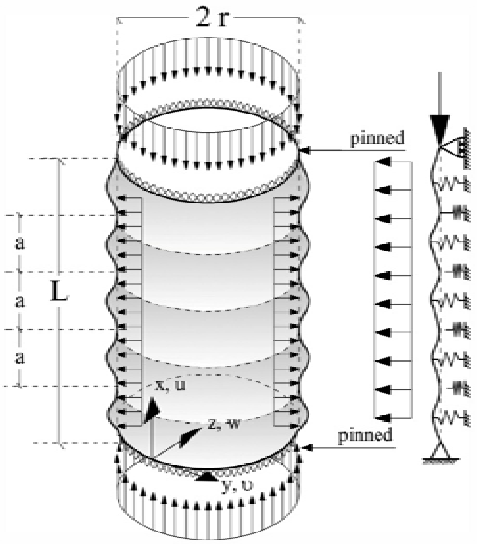

Fig. III.17 Buckling of a cylindrical shell under a combined state of axial loading and lateral pressure.

The resulting equations which govern this problem come from expressions (3.88) to (3.90):

$$r\,\frac{\partial N_x}{\partial x}+\frac{\partial N_{yz}}{\partial \theta}-N_y\left(\frac{\partial^2 v}{\partial \theta\,\partial x}-\frac{\partial w}{\partial x}\right)=0 \qquad \textbf{(3.94)}$$

$$\frac{\partial N_y}{\partial \theta}+r\,\frac{\partial N_{xy}}{\partial x}+\,r\,N_x\frac{\partial^2 v}{\partial x^2}-\,Q_y=0 \qquad \textbf{(3.95)}$$

$$r\,\frac{\partial Q_x}{\partial x}+\frac{\partial Q_y}{\partial \theta}\,+r\,N_x\frac{\partial^2 w}{\partial x^2}+N_y\left(1+\frac{\partial v}{r\,\partial \theta}-\frac{\partial^2 w}{r\,\partial \theta^2}\right)+q\,r=0 \qquad \textbf{(3.96)}$$

From the equilibrium equations of bending moments [equations (3.91) to (3.93)], it is considered that bending and twisting moments are really small in this case. Just for that reason, the products of these moments by the derivatives of the displacements u, v and w are also neglected. By applying this procedure, the first two equations lead to:

$$Q_x=\frac{\partial M_{yx}}{r\,\partial \theta}+\frac{\partial M_x}{\partial x} \qquad \textbf{(3.97)}$$

$$Q_y=\frac{\partial M_y}{r\,\partial \theta}+\frac{\partial M_{xy}}{\partial x} \qquad \textbf{(3.98)}$$

and replacing the obtained values for Q_x and Q_y in the equations (3.94) to (3.96):

$$r\,\frac{\partial N_x}{\partial x}+\frac{\partial N_{yz}}{\partial \theta}-N_y\left(\frac{\partial^2 \upsilon}{\partial\theta\,\partial x}-\frac{\partial w}{\partial x}\right)=0 \qquad \textbf{(3.99)}$$

$$\frac{\partial N_y}{\partial \theta}+r\,\frac{\partial N_{xy}}{\partial x}+r\,N_x\,\frac{\partial^2 \upsilon}{\partial x^2}-\frac{\partial M_y}{r\,\partial\theta}+\frac{\partial M_{xy}}{\partial x}=0 \qquad \textbf{(3.100)}$$

$$\frac{\partial^2 M_{yx}}{\partial\theta\,\partial x}+r\,\frac{\partial^2 M_x}{\partial x^2}+\frac{\partial^2 M_y}{r\,\partial\theta^2}-\frac{\partial^2 M_{xy}}{\partial\theta\,\partial x}+N_y\left(1+\frac{r\,\partial^2 w}{\partial x^2}+\frac{\partial \upsilon}{r\,\partial\theta}-\frac{\partial^2 w}{\mathrm{r}\,\partial\theta^2}\right)+q\,r=0 \qquad \textbf{(3.101)}$$

In reference to the buckling of the shell, it is necessary to considerate those deflections which are capable of perturbing its equilibrium. The value of N_y will be slightly different, and this increment will be expressed as N'_y:

$$N_y=-q\,r+N'_y \qquad \textbf{(3.102)}$$

For this analysis, it is necessary to consider also the stretching of the middle surface of the shell by replacing N_y and q by $N_y\,(1+\epsilon_1)$ and $q(1+\epsilon_1)(1+\epsilon_2)$, respectively in the equations (3.99), (3.100) and (3.101). Knowing that:

$$\epsilon_1=\frac{\partial u}{\partial x} \quad \text{and} \quad \epsilon_2=\frac{\partial \upsilon}{r\,\partial\theta}-\frac{w}{r} \qquad \textbf{(3.103)}\ \textbf{(3.104)}$$

$$D=\frac{E\cdot t^3}{12\cdot(1-\nu^2)} \qquad \textbf{(3.105)}$$

by using the expressions (3.53), (3.54) and (3.56) proposed in the first part of this Section, together with the following notations:

$$\phi_1=\frac{q\,r\,(1-\nu^2)}{E\,t}\ ;\ \phi_2=-\frac{N_x(1-\nu^2)}{E\,t} \quad \text{and} \quad \alpha=\frac{t^2}{12\,r^2} \qquad \textbf{(3.106)}\ \textbf{(3.107)}\ \textbf{(3.108)}$$

According to (Flügge, 1932), equations (3.99), (3.100) and (3.101) can be expressed depending on displacements u,υ,ω by using the parameters ϕ_1,ϕ_2 and α, in the following form:

$$r^2\,\frac{\partial^2 u}{\partial x^2}+\frac{1+\nu}{2}\,\frac{r\,\partial^2 \upsilon}{\partial x\partial\theta}-\nu\,r\,\frac{\partial w}{\partial x}+r\,\phi_1\left(\frac{\partial^2 \upsilon}{\partial x\partial\theta}-\frac{\partial w}{\partial x}\right)+\frac{1-\nu}{2}\,\frac{\partial^2 u}{\partial\theta^2}=0 \qquad \textbf{(3.109)}$$

$$\frac{1+\nu}{2}\,\frac{r\,\partial^2 u}{\partial x\,\partial\theta}+\frac{1-\nu}{2}\,r^2\frac{\partial^2 \upsilon}{\partial x^2}+\frac{\partial^2 \upsilon}{\partial\theta^2}-\frac{\partial w}{\partial\theta}+ \qquad \textbf{(3.110)}$$
$$+\alpha\left[\frac{\partial^2 \upsilon}{\partial\theta^2}+\frac{\partial^3 w}{\partial\theta^3}+r^2\frac{\partial^3 w}{\partial x^2\partial\theta}+r^2(1-\nu)\frac{\partial^2 \upsilon}{\partial x^2}\right]-r^2\,\phi_2\,\frac{\partial^2 \upsilon}{\partial x^3}=0$$

$$r\cdot\nu\,\frac{\partial u}{\partial x}+\frac{\partial \upsilon}{\partial\theta}-w-\alpha\left[\frac{\partial^3 \upsilon}{\partial\theta^3}+(2-\nu)\,r^2\frac{\partial^3 \upsilon}{\partial x^2\partial\theta}+r^4\,\frac{\partial^4 w}{\partial x^4}+\frac{\partial^4 w}{\partial\theta^4}+2r^2\frac{\partial^4 w}{\partial x^2\partial\theta^2}\right]= \qquad \textbf{(3.111)}$$

$$= \phi_1 \left(w + \frac{\partial^2 w}{\partial \theta^2} \right) + \phi_2 \, r^2 \, \frac{\partial^2 w}{\partial x^2}$$

Then, to obtain the critical value under a state of combined vertical stress and lateral pressure, it is necessary to solve the three differential equations proposed above, by satisfying also the boundary conditions of the shell. For a generic cylinder, simply supported in the loaded edges, the boundary conditions can be introduced by assuming that w and $\partial^2 w/\partial x^2$ are zero at the ends. The solution for displacements $u, v \; and \; w$ is in this case:

$$u = A \sin n\,\theta \cos \frac{\pi\, x}{l} \qquad \textbf{(3.112)}$$

$$v = B \cos n\,\theta \sin \frac{\pi\, x}{l} \qquad \textbf{(3.113)}$$

$$w = C \sin n\,\theta \sin \frac{\pi\, x}{l} \qquad \textbf{(3.114)}$$

By replacing equations (3.112) to (3.114) in the three previous differential equations, a system of three linear equations for A, B and C coefficients can be obtained. The equation for calculating the critical value of vertical stress or lateral pressure comes from equating to zero the determinant of these three equations. According to (Flügge, 1932), the final equation can be simplified to:

$$C_1 + C_2 \alpha = C_3 \phi_1 + C_4 \phi_2 \qquad \textbf{(3.115)}$$

where:

$$C_1 = (1 - \nu^2)\lambda^4 \qquad \textbf{(3.116)}$$

$$C_2 = (\lambda^2 + n^2)^4 - 2[\nu\,\lambda^6 + 3\lambda^4 n^2 + (4 - \nu)\lambda^2 n^4 + n^6] + 2(2 - \nu)\lambda^2 n^2 + n^2 \qquad \textbf{(3.117)}$$

$$C_3 = n^2(\lambda^2 + n^2)^2 - (3\lambda^2 n^2 + n^4) \qquad \textbf{(3.118)}$$

$$C_4 = \lambda^2(\lambda^2 + n^2)^2 + \lambda^2 n^2 \qquad \textbf{(3.119)}$$

being:

$$\alpha = \frac{t^2}{12\, r^2} \qquad \textbf{(3.120)}$$

$$\lambda = \frac{m\, \pi\, r}{l} \qquad \textbf{(3.121)}$$

By assuming specific values for *m* and *2n* [referred to the number of axial and circumferential wavelengths, respectively], the equation (3.115) can be represented in the bidimensional plane formed by the coordinates (ϕ_1, ϕ_2). Keeping constant the value of *m*, a collection of linear curves can be determined corresponding to n = 2,3,4,5 ...; the smaller values of ϕ_2 for a given value of ϕ_1 at each range generates the line which determines the critical stress, depending on axial load and lateral pressure [see Fig. III.18].

As it can be observed, the prediction of critical stress under a combined state of axial loading and lateral pressure is much more complex than the case where only axial load is considered. Besides, the approximation given by the latter is enough accurate to predict the critical stress and the mode of buckling of CFT sections, as vertical stress is usually much higher than the circumferential.

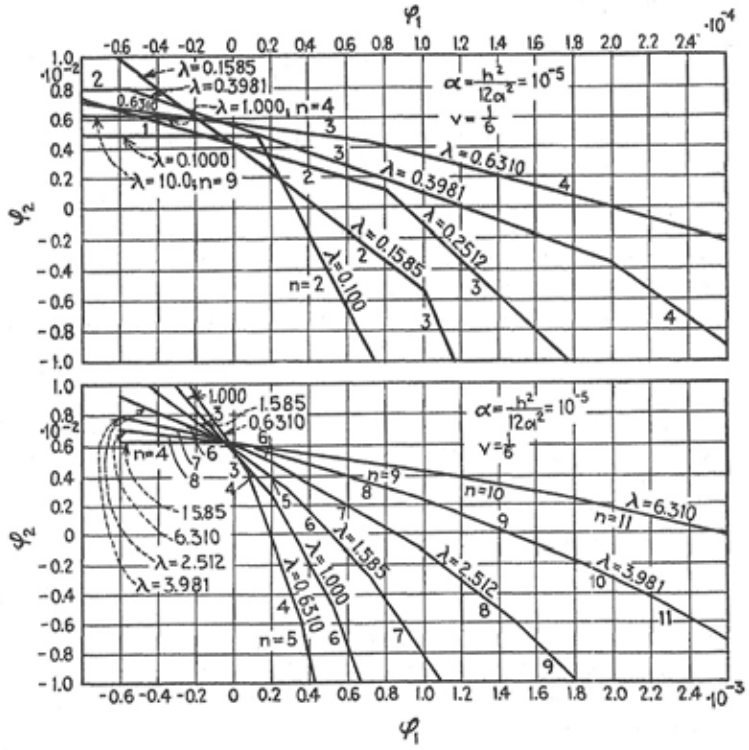

Fig. III.18 Linear curves in the (ϕ_1, ϕ_2) plane, defining the buckling stresses under combined axial loading and lateral pressure.
ϕ_1 refers to lateral pressure and ϕ_2 refers to axial load, (Timoshenko, et al., 1961).

3.2.5 Resistant advantages of introducing stiffening plates in circular CFT sections.

The main objective of this investigation is to analyze the behavior of concrete-filled tubes stiffened with plates, assuming a state of pure compression; the purpose is to compare their behavior with the compressive response of non-stiffened tubes. As it has been explained before, these typologies have the clear vocation of increasing the confinement effect and the ductility of the composite section, thanks to the restriction to buckling of the plates.

In case of thick-walled circular CFT sections, the fact of replacing part of the steel of the tube by these plates seems to not have a clear influence on ductility and confinement effect. The case of thin-walled tubes is clearly different, since the fact of stiffening restrains local buckling of the shell. This will be demonstrated in further chapters, especially in Chapter VII.

Referring to thick-walled tubes, the maximum pressure on concrete core is determined by the maximum circumferential tensile force resisted by the tube wall. This annular force is determined by the scheme of case a) in figure III.19. Cylindrical shells in CFT sections are not subjected to bending in the cross-sectional plane, since they become strictly tensioned circumferentially. By assuming the introduction of stiffening plates in the core as in the model shown in case b) of the following figure III.19, the tensile stress of the wall is combined with bending, as a consequence of the high rigidity provided by stiffening plates to the tube in the points of their concurrence [some parasit moments appear as a result of stiffening specific points of the tube].

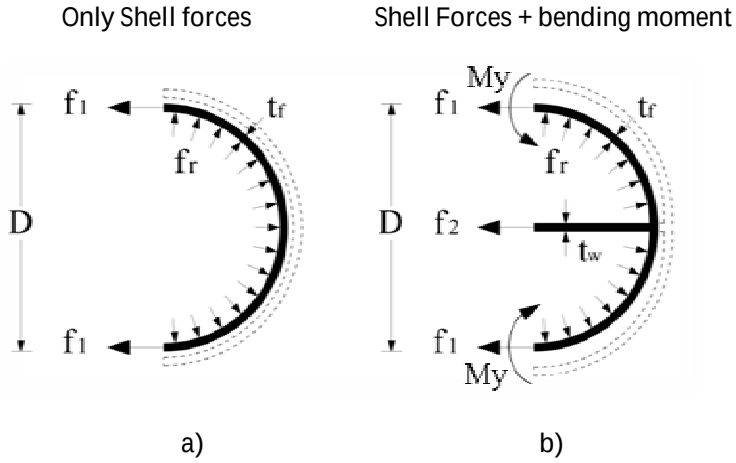

Fig. III.19 Distribution of pressure on the steel tube: a) unstifffened, b) stiffened tube.
The horizontal component of lateral pressure is converted into tensile forces in the tube wall.

For circular shapes, it will be easily demonstrated that $f_2 \ll f_1$ [see Fig. III. 22], as a result of the efficiency of circular geometry of the tube. Thus, stiffening plates do not contribute actively to absorb this internal pressure derived from volumetric expansion of concrete core.

By following this assumption, the horizontal component of pressure is equal to the product of the thickness by the yield limit stress of steel. In cases b) and c), the same equivalence cannot be supposed [by adding the thickness of the internal plates to the tube], since the intersection points are much more rigid than the rest. If stiffening plates are stiffer in the axial direction, the welded shell between them becomes subjected to slight parasite bending moments, apart from the axial tensile stress. Then, the introduction of stiffening plates could be even prejudicial, as circular shells behave better subjected to annular tension than under combined tension and bending.

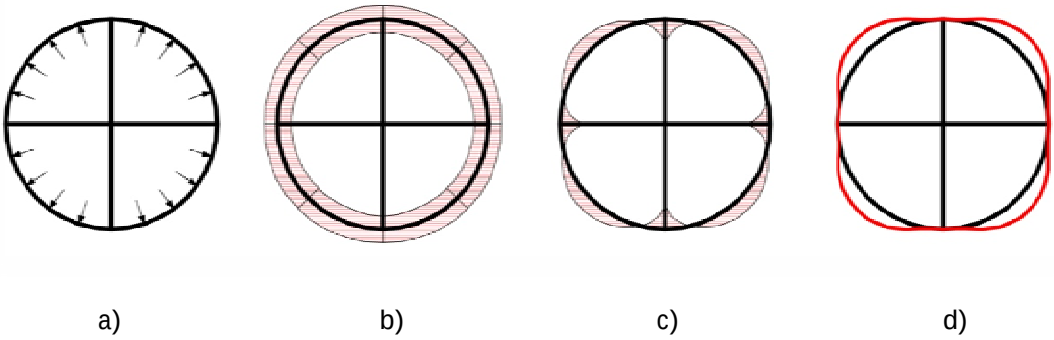

Fig. III.20 Static analysis of the cross-section, assuming a uniform distribution of pressure.
Bidimensional analysis of the steel tube in circular CFT sections.
[a] Considered uniform pressure [b] Axial force [c] Bending moments [d] Deformed shape

In figure III.20, it can be noted how those points of the tubes which intersect with stiffening plates are really stiffer than the rest, and how bending moments are more important in these intersection points and in the mid-span of the derived sectors. Then, the tube tends to fail owing to the conjunction of tension and bending in these areas, being not capable of reaching the full yield limit stress of steel in the whole section. Bending moment diagrams shown in figure III.20 [c] are caused

by the simplification of the circular geometry of the tube into a finite number of individual bars, just for modeling reasons. A more credible distribution of bending moments in the cross-sectional plane will be something similar to figure III.21:

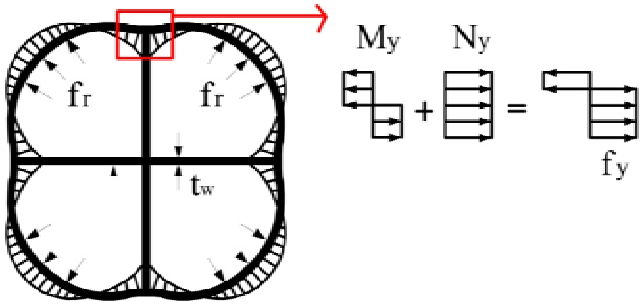

Fig. III.21 Idealization of bending of the tube in the cross-sectional plane, owing to the rigidity of the stiffening plates.
The cylinder is subjected to a combined state of tension and slight bending in the [*yz*] plane. Lateral pressure *fr* is considered constant in this assumption.

From this simple and elastic analysis, we can conclude that this phenomenon leads to a low effectiveness in confinement effect of cruciform shapes, in comparison with circular geometries. Of course, concrete of central areas will be more severely confined, but the efficacy of this confinement in relative terms will be poorer compared with that shown by a circular shape. Besides, it seems that the presence of stiffening plates does not have a positive effect on the ductility of CFT sections; however all these assumptions will have to be validated by the FE model [see Chapters VI and VII].

The plates which are embedded in concrete seem to be completely restricted to buckling, by giving to the section an important increment of load-bearing capacity [this effect will be also analyzed from results of the FE analysis]. In addition, their distribution in the cross-sectional could play a decisive role in resisting shear forces, so that they become useful for those columns located in ground floors of tall buildings.

A 2-D elastic analysis has been carried out, by comparing the influence of different thicknesses of stiffening plates. From this analysis, it can be seen how thickness is not really significant on results; once stiffening plates are welded to the tube, the deformed shape quickly changes from a circular geometry into cruciform, almost independently of their thickness [see figure III.22]. Note that force f_2 of figure III.20 is infinitely smaller than f_1, owing to circular geometry. This means that most part of the pressure is absorbed by the tube wall. However, in case a), the tube is completely tensioned [thanks to be circular-shaped], while in case b) it is also slightly bended.

In unstiffened circular concrete-filled tubes, the pressure derived from volumetric expansion of concrete is fully absorbed by a tensile stress on the tube wall-thickness. Thus, no bending moments appear in the cross-sectional plane thanks to the efficiency of the circular shape; this effect is represented by case b) of the first row in figure III.22, although in this simplified bidimensional analysis the stiffening bars have been considered with an area almost zero instead of zero, strictly for numerical reasons. Therefore, the parasit bending moments have been omitted in the figure presented below.

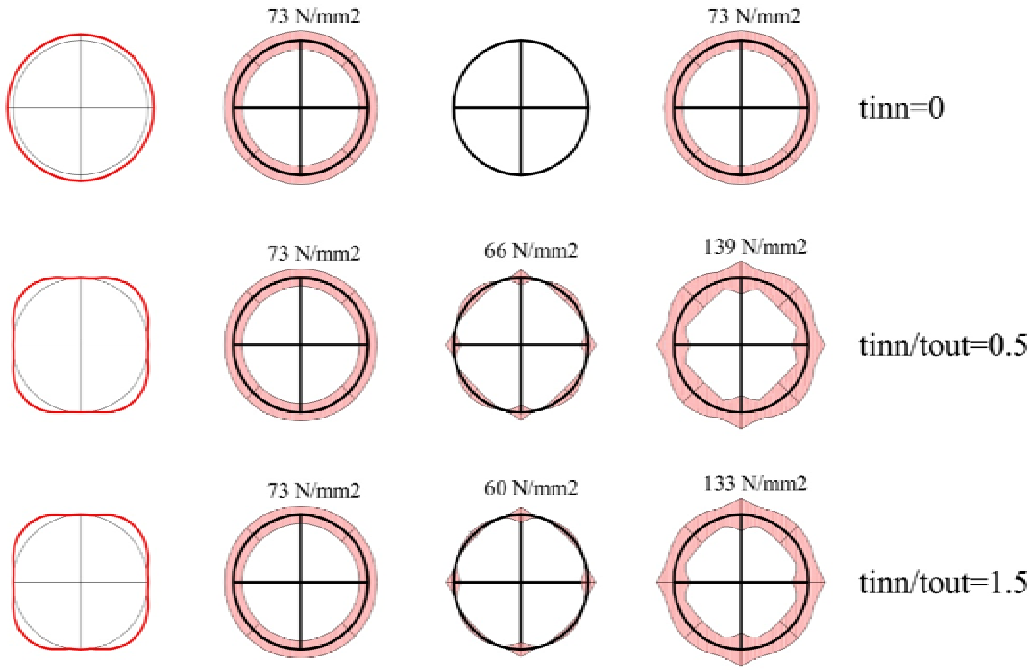

a) Deformed shape b) σ_{AXIAL} c) $\sigma_{BENDING}$ d) $\sigma_{TOTAL,max}$

Fig. III.22 Influence of the thickness of stiffening plates on the deformed shape of the tube.
No significant influence is observed, derived from the thickness of the inner plates.
[a] Deformed shape [b] Stress from Axial Force [c] Stress from Bending Moment
[d] Total Max Stress

3.3 Elastic analysis of rectangular concrete-filled tubes under compression.

In case of rectangular and square-shaped CFT sections, the stress distribution of the core is much less uniform than in case of circular sections. The fact of disposing the plates one perpendicular to the other, and being completely planar, involves the appearance of bending moments and important deflections, with the consequent decrement of confinement effect on concrete core.

These deflections appear especially in central areas of the plates of the tube, so that in the nearby of the edges concrete becomes more confined than in the mid-span of the plates. This effect is well illustrated in figure III.23, where the core has been modeled by using a set of individual and bidimensional bars, with different lengths depending on the position. This model was firstly introduced by Susantha (Susantha, et al., 2000) in its investigation about the confinement effect on concrete and the importance of the softening period.

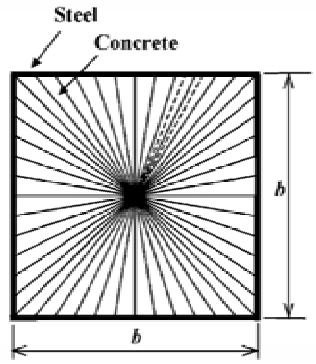

Fig. III.23 Theoretical discretization of concrete core in individual linear bars.
Model proposed by Susantha and Ge (Susantha, et al., 2000)

Thus, lateral pressure on concrete core is not constant along the perimeter, depending on the orientation. Using the simplification shown in figure III.23, it would be possible to calculate an "equivalent pressure" as a result of integrating all forces generated by each individual bar. For that purpose, it would be necessary to do a non-linear analysis and bidimensional, since the model corresponds to an idealization of a slice of the theoretical column and concrete does not behave linearly. The expression which summarizes the idea of calculating an equivalent value of pressure on the core is the following:

$$f_{r,eq} = \frac{\sum_l^n F_{ri}}{\sum_l^n S_i} \qquad \textbf{(3.122)}$$

where:

F_{ri} *Reactions at the ends of the fictitious bars.*
S_i *Corresponding area of each individual bar.*

The averaged transversal strain of the plates could be calculated using the following integration:

$$w_{r,eq} = \frac{\sum(U_i/L_i)}{n} \qquad \textbf{(3.123)}$$

where:

L_i *Length of each individual bar*
U_i *Transversal displacement of each individual bar.*
n *Number of bars.*

Using these expressions, it would be possible to analyze the confinement effect of rectangular CFT sections analytically. By replacing the value of $f_{r,eq}$ in equation (2.19), it is possible to approximate the confinement effect in these cases, by loading only the core and without considering friction forces. To analyze these individual bars, and assuming that pressure is far from being constant along the plates, the following expression can be used for lateral stiffness of each concrete bar:

$$k = \frac{A \cdot E_{cr}}{L_c} \qquad \textbf{(3.124)}$$

being:

A *Cross-sectional area of the idealized element.*

E_{cr} *Tangent modulus of elasticity of concrete in the lateral direction.*

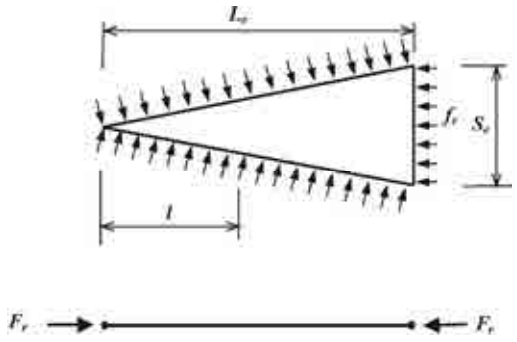

Fig. III.24 Idealized concrete element.
Model proposed by Susantha and Ge (Susantha, et al., 2000)

However, results obtained through this theoretical method come from an approximation of the real 3-D problem, far from being an accurate approach. The plates in rectangular-shaped tubes bend in the two axes, and boundary conditions are decisive to determine the maximum deflection and confinement effect on the core. This is the reason why this analytical approximation is not enough accurate to provide reliable results.

3.3.1 Differences in behavior from circular-shaped sections.

The compressive behavior of rectangular and square-shaped CFT sections is really different from that of circular sections, in many aspects. Main divergence lies in the capacity of the tube of confining the core: while in circular tubes this effect is uniform and really significant, in square sections it is more heterogeneous and consequently, smoother.

However, the loading process is similar in both cases, with a first elastic period during which the core becomes slightly tensioned circumferentially by the tube, and a second elastic-plastic period in which the concrete starts expanding laterally. During this second phase, concrete becomes triaxially compressed thanks to be contained by the tube. Contact of the interface is subjected to lateral strains coming from bending of the plates and from the difference in Poisson's ratio of both materials. The difference between lateral displacements of steel and concrete at each point determines the severity of hydrostatic pressure on the core, far from being uniform.

Owing to the low confining pressure shown by rectangular and square-shaped sections, all application codes worldwide, dealing with CFT sections, limit the transference of tangential stresses between components in square sections to values of 0.40 N/mm^2, instead of 0.55 N/mm^2. The latter corresponds to the limit allowed for circular sections, assuming that contact pressure is really higher in those cases.

3.3.2 Influence of local buckling in square-shaped CFT sections.

The lack of uniform pressure on the core is not only a phenomenon of the cross-section in thin-walled tubes, but also of the height of the column -since the plates bend in their two possible axes. This fact confers to the system a third dimension, giving more complexity to the problem and converting into impractical an analytical resolution if accurate results are wanted. Thin plates could be more effective than thick plates from the point of view of cost, although buckling effects have to be controlled accurately. To avoid instability problems, the Eurocode gives some basic expressions

referring to the B/t ratio, in a similar way than for circular sections (Hicks, et al., 2002). Rectangular and square-shaped tubes do not buckle, providing that the following proportion is satisfied:

$$\frac{B}{t} \leq 52 \cdot \varepsilon \qquad \text{[in steel S275, this value is 42.30]} \qquad \textbf{(3.125)}$$

On the one hand, the plates forming the faces of the tube have two stiffened edges [assumed as embedded edges], and on the other hand, the other two show continuity in the [x] axis as a virtual infinite column. This condition of continuity generates a mode of deformation in double curvature that tends to reduce the wavelengths of the plates, compared with other hypothetical analyses based on isolated column slices. The deformation of the plates takes a sinusoidal shape, and this fact implies to have some areas more confined than the others; for that reason, local buckling of the plates in rectangular and square thin-walled CFT sections becomes something decisive, in order to determine the maximum load bearing capacity of the section.

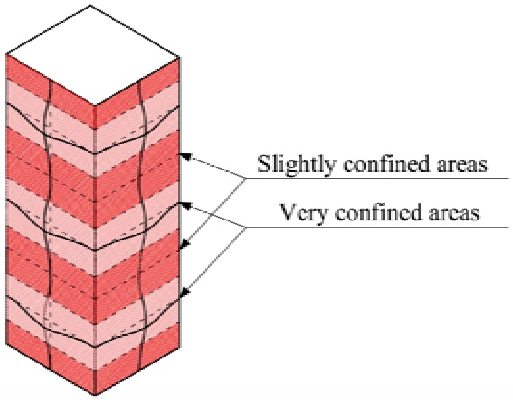

Fig. III.25 Mode of buckling of the plates in thin-walled square CFT sections.

Logically, the value of the wavelength will depend on the thickness basically, but also on the buckling length [corresponding always to the widest side in case of rectangular sections]. Thus, as smaller is the width of the tube, higher is the confinement effect which can be considered. In rectangular tubes, the deformed shape is mostly governed by the wider plate as it can be observed in results presented in Chapter VI.

3.3.2.1 Buckling analysis of rectangular plates owing to axial loading.

Although this study only proposes a complete analytical model for circular CFT sections subjected to compression[11], the elastic buckling analysis of the tubes has been done for both typologies. The fact of considering buckling of the plates in square sections is decisive in order to understand their compressive behavior.

Thus, it is known that as a consequence of axial loading, the plates of square thin-walled CFT sections are subjected to second-order effects. The deflection takes place always outwards, since these plates are restricted by concrete of the core. Regarding to boundary conditions, the plates have two edges restricted against rotation, and two edges clamped in order to simulate the effect of

[11] The analytical approach for square-shaped tubes under compression sections has not been proposed analytically, owing to its complexity.

continuity of the column according to the figure III.25. Different from circular-shaped sections, buckling of square tubes is analyzed by considering axial loading only since the influence of lateral pressure is really much less important in this case [lateral pressure in circular sections can reach significant values being uniformly distributed].

First of all, to describe the problem it is necessary to propose the static equilibrium of a cut of a plate under a combined state of axial loading, *N*, and lateral uniform pressure, *q*. The element is formed by the cut of two pairs of planes parallel to the *xz* and *yz* planes. The forces resulting are those represented in figure III.26:

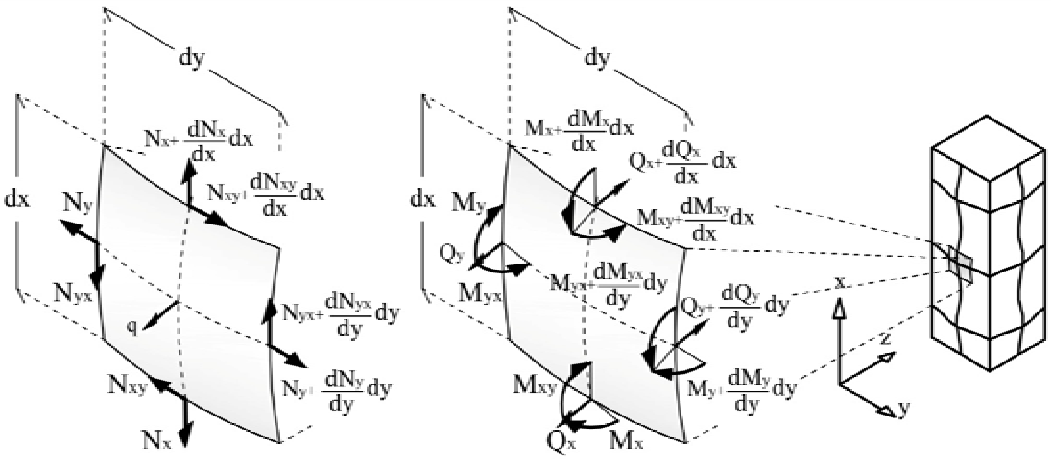

[a] [b]

Fig. III.26 Static analysis of a cut of plate subjected to axial loading and lateral pressure.

By projecting the forces represented in figure III.26.a on the [*x*] and [*y*] axes, and considering that there are no body forces acting in these directions:

$$\frac{\partial N_x}{\partial x} + \frac{\partial N_{yx}}{\partial y} = 0 \qquad \textbf{(3.126)}$$

$$\frac{\partial N_y}{\partial y} + \frac{\partial N_{xy}}{\partial x} = 0 \qquad \textbf{(3.127)}$$

then, by considering the projection of the mentioned forces on the [*z*] axis, owing to the curvature of the plate:

$$-N_x\, dy\, \frac{\partial w}{\partial x} + \left(N_x + \frac{\partial N_x}{\partial x} dx\right)\left(\frac{\partial w}{\partial x} + \frac{\partial^2 w}{\partial x^2} dx\right) dy \qquad \textbf{(3.128)}$$

the small quantities of higher order can be neglected from the last expression:

$$N_x\, \frac{\partial^2 w}{\partial x^2}\, dx\, dy + \frac{\partial N_x}{\partial x}\, \frac{\partial w}{\partial x}\, dx\, dy \qquad \textbf{(3.129)}$$

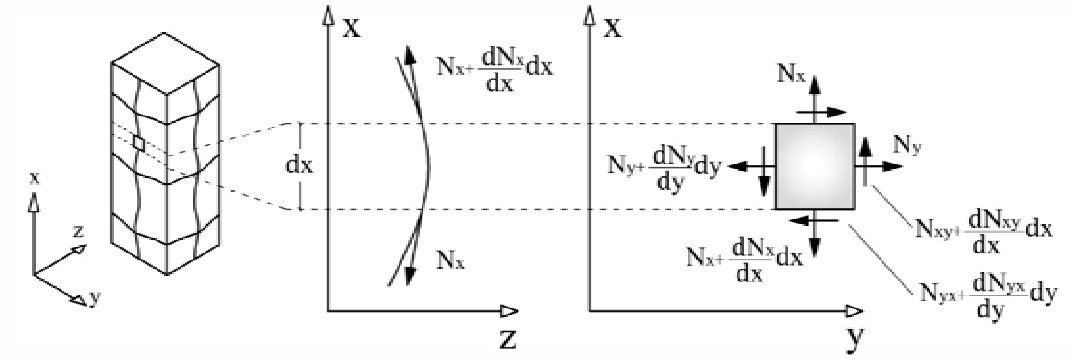

Fig. III.27 Equilibrium of a cut of plate subjected to combined bending and compression.

and for N_y, we obtain expression (3.130), by following the same procedure:

$$N_y \frac{\partial^2 w}{\partial y^2} dx\, dy + \frac{\partial N_y}{\partial y} \frac{\partial w}{\partial y} dx\, dy \qquad \textbf{(3.130)}$$

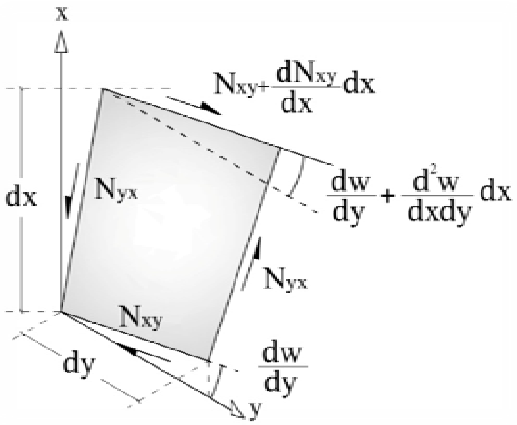

Fig. III.28 Deflection of an element $dx\ dy$ of the middle plane

Through the analysis of the deflection of an infinitesimal element $dx\ dy$, according to figure III.28, and projecting the shearing force N_{xy} on the [z] axis, the following expression is obtained:

$$N_{xy} \frac{\partial^2 w}{dx\, dy} dx\, dy + \frac{\partial N_{xy}}{\partial x} \frac{\partial w}{\partial y} dx\, dy \qquad \textbf{(3.131)}$$

owing to the two angles represented in the previous figure:

$$\frac{\partial w}{\partial y} \quad \text{and} \quad \frac{\partial w}{\partial y} + \frac{\partial^2 w}{\partial x\, \partial y} dx \qquad \textbf{(3.132)}$$

by following the same procedure for N_{yx}, and adding all the projections:

$$2N_{xy}\,\frac{\partial^2 w}{dx\,dy}\,dx\,dy + \frac{\partial N_{xy}}{\partial x}\,\frac{\partial w}{\partial y}\,dx\,dy + \frac{\partial N_{xy}}{\partial y}\,\frac{\partial w}{\partial x}\,dx\,dy \qquad \textbf{(3.133)}$$

By adding the expressions obtained for projections on the [*z*] axis of N_y, N_x and $N_{yx} + N_{xy}$ to the transversal load [result of the product of the pressure *q* by the infinitesimal area $dxdy$], we obtain the expression for the equilibrium of the element:

$$\frac{\partial^2 M_x}{\partial x^2} - 2\frac{\partial^2 M_{xy}}{dx\,dy} + \frac{\partial^2 M_y}{\partial y^2} = -\left(q + N_x\frac{\partial^2 w}{\partial x^2} + N_y\frac{\partial^2 w}{\partial y^2} + 2N_{xy}\frac{\partial^2 w}{dx\,dy}\right) \qquad \textbf{(3.134)}$$

In plates of square-shaped tubes, it is obvious that bending occurs in double curvature. To analyze those moments of the plates, it is necessary to consider an infinitesimal element cut as it is shown in figure III.27. We assume that during bending, lateral sides of the element remain plane and rotate about the neutral axes *n-n*, so as to remain normal to the deflection surface; then we can conclude that the middle surface of the plate does not suffer any deformation and it can be called neutral surface. The unitary elongations in the [*x*] and [*y*] axes at distance *z* from the neutral surface can be obtained as in case of a beam:

$$\epsilon_z = \frac{z}{\rho_x} \quad \text{and} \quad \epsilon_y = \frac{z}{\rho_y} \qquad \textbf{(3.135)}$$

where:

$1/\rho_x$ *Curvature of the neutral surface in sections parallel to the [zx] planes*
$1/\rho_y$ *Curvature of the neutral surface in sections parallel to the [yz] planes*

By applying the Hook's law, we can obtain the following expressions:

$$\epsilon_z = \frac{1}{E}(\sigma_z - \nu\sigma_y) \quad \text{and} \quad \epsilon_z = \frac{1}{E}(\sigma_y - \nu\sigma_z) \qquad \textbf{(3.136)}$$

And then, the stresses in the infinitesimal cut of lamina are the following:

$$\sigma_z = \frac{E_z}{1-\nu^2}\left(\frac{1}{\rho_x} + \nu\frac{1}{\rho_y}\right) \quad \text{and} \quad \sigma_z = \frac{E_z}{1-\nu^2}\left(\frac{1}{\rho_y} + \nu\frac{1}{\rho_x}\right) \qquad \textbf{(3.137)}$$

The distributed normal stresses over the lateral sides of the element can be reduced to couples which must be equal to the external moments:

$$\int_{-h/2}^{h/2}\sigma_z\; z\,dy\,dz = M_x\,dy \quad \text{and} \quad \int_{-h/2}^{h/2}\sigma_y\; z\,dx\,dz = M_y\,dx \qquad \textbf{(3.138)}$$

By replacing the expressions obtained for stresses in these last expressions, we get the value of the bending moments in the two axes:

$$M_x = D\left(\frac{1}{\rho_x} + \nu\frac{1}{\rho_y}\right) \quad \text{and} \quad M_y = D\left(\frac{1}{\rho_y} + \nu\frac{1}{\rho_x}\right) \qquad \textbf{(3.139)}$$

where:

$$D = \frac{E_z}{1-\nu^2}\int_{-t/2}^{t/2} z^2\, dz = \frac{E_z}{12(1-\nu^2)} \qquad \textbf{(3.140)}$$

Finally, D corresponds to the flexural rigidity of the plate.
The assumption that there is no strain in the middle plane of a plate during bending is true if the deflections are really small compared with the thickness, *t*. Assuming that w is the deflection of the plate, we can express the curvature of the plate through the well-known expression:

$$\frac{1}{\rho_x} = \frac{\partial^2 w}{\partial x^2} \quad \text{and} \quad \frac{1}{\rho_y} = \frac{\partial^2 w}{\partial y^2} \qquad \textbf{(3.141)}$$

we obtain the expressions for bending moments in a rectangular plate:

$$M_x = -D\left(\frac{\partial^2 w}{\partial x^2} + \nu\frac{\partial^2 w}{\partial y^2}\right) \quad \text{and} \quad M_y = -D\left(\frac{\partial^2 w}{\partial y^2} + \nu\frac{\partial^2 w}{\partial x^2}\right) \qquad \textbf{(3.142)}\ \textbf{(3.143)}$$

Then, by replacing these expressions for the bending moments in the equation (3.134):

$$\frac{\partial^4 w}{\partial x^4} - 2\frac{\partial^4 w}{\partial x^2 \partial y^2} + \frac{\partial^4 w}{\partial y^4} = \frac{1}{D}\left(q + N_x\frac{\partial^2 w}{\partial x^2} + N_y\frac{\partial^2 w}{\partial y^2} + 2N_{xy}\frac{\partial^2 w}{dx\, dy}\right) \qquad \textbf{(3.144)}$$

In order to finalize the analysis, it is also necessary to study the strain energy in bending of plates. By having a rectangular plate under bending by uniformly distributed moments M_x and M_y, the strain energy accumulated in an element can be obtained by calculating the work done by the moments $M_x dy$ and $M_y dx$ on the element. As the sides of the element remain plane, the work done by these moments is obtained by taking one half of the product of the moment and the angle between the sides of the element after bending. Assuming that the curvature of the plate in the [*xz*] plane can be expressed as $-\partial w^2/\partial x^2$, the corresponding angles to the moments $M_x dy$ and $M_y dx$ are $-(\partial w^2/\partial x^2)dx$ and $-(\partial w^2/\partial y^2)dx$, and the work done by these moments is:

$$-\frac{1}{2}M_x\frac{\partial^2 w}{\partial x^2}dx\, dy \quad \text{and} \quad -\frac{1}{2}M_y\frac{\partial^2 w}{\partial y^2}dx\, dy \qquad \textbf{(3.145)}$$

Then, the work produced by these two moments will be the result of adding the two expressions, and this will be the potential energy of the element:

$$dU = -\frac{1}{2}\left(M_x\frac{\partial^2 w}{\partial x^2} + M_y\frac{\partial^2 w}{\partial y^2}\right)dx\, dy \qquad \textbf{(3.146)}$$

Finally, by replacing the moments M_x and M_y for their respective expressions [eq. (3.142) and (3.143)], we obtain:

$$dU = -\frac{1}{2}D\left[\left(\frac{\partial^2 w}{\partial x^2}\right)^2 + \left(\frac{\partial^2 w}{\partial y^2}\right)^2 + 2\nu\frac{\partial^2 w}{\partial x^2}\frac{\partial^2 w}{\partial y^2}\right]dx\, dy \qquad \textbf{(3.147)}$$

And the total strain energy of the plate can be obtained by integrating the previous expression:

$$U = -\frac{1}{2} D \iint \left[\left(\frac{\partial^2 w}{\partial x^2} \right)^2 + \left(\frac{\partial^2 w}{\partial y^2} \right)^2 + 2\nu \frac{\partial^2 w}{\partial x^2} \frac{\partial^2 w}{\partial y^2} \right] dx\, dy \qquad \textbf{(3.148)}$$

By considering an element of the plate, and also neglecting the strain energy due to shearing forces Q_x and Q_y, it derives that the strain energy of the element is equal to the work done on it by the bending moments $M_x dy$ and $M_y dx$ and by the twisting moments $M_{xy} dy$ and $M_{yx} dx$. The total strain energy done by the pure bending moments has been obtained in (3.148). In order to take also into account the strain energy done by the twisting moments M_{xy} and M_{yx} the corresponding twisting angle shown in figure III.27 is used,$(\partial^2 w / dx\, dy) dx$, and the expression for the strain energy is:

$$\frac{1}{2} M_{xy} \frac{\partial^2 w}{dx\, dy} dx\, dy = \frac{1}{2} D\,(1-\nu) \left(\frac{\partial^2 w}{dx\, dy} \right)^2 dx\, dy \qquad \textbf{(3.149)}$$

As in the case described before, the work produced by M_{xy} will be the same as for M_{yx}, therefore:

$$dU = -\frac{1}{2} D \left[\left(\frac{\partial^2 w}{\partial x^2} \right)^2 + \left(\frac{\partial^2 w}{\partial y^2} \right)^2 + 2\nu \frac{\partial^2 w}{\partial x^2} \frac{\partial^2 w}{\partial y^2} \right] dx\, dy + D\,(1-\nu) \left(\frac{\partial^2 w}{dx\, dy} \right)^2 dx\, dy \qquad \textbf{(3.150)}$$

And the total strain energy of the plate will be:

$$U = \frac{D}{2} \iint \left\{ \left(\frac{\partial^2 w}{\partial x^2} + \frac{\partial^2 w}{\partial y^2} \right)^2 - 2 \cdot (1-\mu) \cdot \left[\frac{\partial^2 w}{\partial x^2} \frac{\partial^2 w}{\partial y^2} - \left(\frac{\partial^2 w}{\partial x \partial y} \right)^2 \right] \right\} \partial x \partial y \qquad \textbf{(3.151)}$$

According to Cai together with Long (Cai, et al., 2009), the four edges of a rectangular tube can be considered elastically restrained against rotation due to the assumption of high rigidity. The rest of loaded edges must be considered clamped, in order to simulate the continuity of the column. The model to analyze the effects of buckling under axial loading in rectangular plates is the following, shown below:

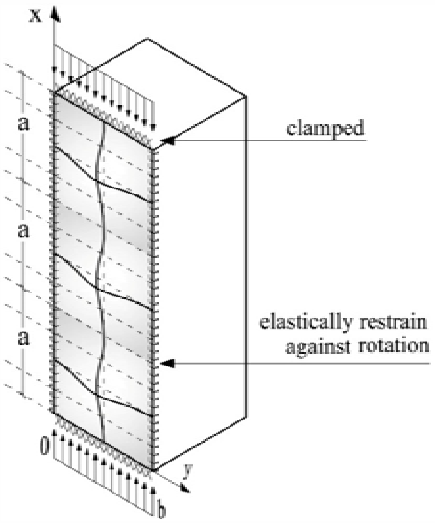

Fig. III.29 Boundary conditions of a buckling analysis of a plate in a rectangular CFT section.
The four edges are considered elastically restrained against rotation, assuming q=0.

Using the mentioned equation (3.151) obtained to calculate the strain energy of a plate, *U*, and the expression of the energy produced by the applied load, *V*, with the form[12]:

$$V = \frac{1}{2}\iint \left[N_x \left(\frac{\partial w}{\partial x}\right)^2 + 2N_{xy}\left(\frac{\partial w}{\partial x}\frac{\partial w}{\partial y}\right) + N_y \left(\frac{\partial w}{\partial y}\right)^2 \right] \partial x \partial y \qquad \textbf{(3.152)}$$

and knowing that in rectangular CFT sections subjected to pure axial loading, boundary stresses of the plates are $\sigma_y = \tau_{xy}$, then:

$$N_y = \sigma_y \cdot t = N_{xy} = \tau_{xy} \cdot t = 0 \qquad \textbf{(3.153)}$$

$$N_x = -p_x \cdot t = -\sigma_x \cdot t \qquad \textbf{(3.154)}$$

In point $x = 0$ or $x = a$, the displacement in the [*z*] axis is zero, due to the sinusoidal shape:

$$w = \frac{\partial w}{\partial x} = 0 \qquad \textbf{(3.155)}$$

On the contrary, when $y = 0$ or $y = b$, then:

$$w = 0, \quad M_y = \begin{cases} -D\dfrac{\partial^2 w}{\partial y^2} = -\zeta_r \dfrac{\partial w}{\partial y} & (y = 0) \\ -D\dfrac{\partial^2 w}{\partial y^2} = +\zeta_r \dfrac{\partial w}{\partial y} & (y = b) \end{cases} \qquad \textbf{(3.156)} \quad \textbf{(3.157)}$$

where deformation must be positive $w \geq 0$, and ζ_r is the twisting stiffness of the unloaded edges. By assuming that the deformed shape of the plate on the [*x*] axis is a cosine function, and that the deformed shape on the [*y*] axis is a biquadrate function, according to Cai and Long (Cai, et al., 2009):

$$w = C \cdot \left[a_1 \cdot \frac{y}{b} \cdot \left(1 - \frac{y}{b}\right) + a_2 \cdot \left(\frac{y}{b}\right)^2 \cdot \left(1 - \frac{y}{b}\right) + a_3 \cdot \left(\frac{y}{b}\right) \cdot \left(1 - \frac{y}{b}\right)^2 + a_4 \cdot \left(\frac{y}{b}\right)^2 \cdot \left(1 - \frac{y}{b}\right)^2 \right] \cdot \left(1 - cos\frac{2\pi}{a}\right) \qquad \textbf{(3.158)}$$

This last function satisfies both boundary conditions as well as compatibility of deformations. By replacing the derivative respect [*y*] of the last equation (3.158) in equations (3.156) and (3.157), it can be observed how coefficient a_2 is equal to the coefficient a_3 in equation (3.158). Assuming this equivalence, the expression (3.158) can be simplified in the following form:

$$w = C \cdot \left[\frac{y}{b} \cdot \left(1 - \frac{y}{b}\right) + m \cdot \left(\frac{y}{b}\right)^2 \cdot \left(1 - \frac{y}{b}\right)^2 \right] \cdot \left(1 - cos\frac{2\pi}{a}\right) \qquad \textbf{(3.159)}$$

Replacing the derivative in first order and the partial derivative in second order in respect to [*y*] of equation (3.159) in equations (3.156) and (3.157), the following expression can be obtained:

$$m = \chi + 1 \qquad \textbf{(3.160)}$$

[12] (Cai, et al., 2009)

where χ is the coefficient of elastic restraint against rotation of the unloaded edges, defined by the following expression:

$$\chi = \frac{\zeta_r \cdot b}{2 \cdot D} \tag{3.161}$$

Equation (3.159) can be rewritten in the following form:

$$\omega = C \cdot \left[\frac{y}{b} + \emptyset_1 \cdot \left(\frac{y}{b}\right)^2 + \emptyset_2 \cdot \left(\frac{y}{b}\right)^3 + \emptyset_3 \cdot \left(\frac{y}{b}\right)^4\right] \cdot \left(1 - cos\frac{2\pi x}{a}\right) \tag{3.162}$$

where C is a constant and factors $\emptyset_1, \emptyset_2, \emptyset_3$ are:

$$\emptyset_1 = \chi \tag{3.163}$$

$$\emptyset_2 = -2\,(\chi + 1) \tag{3.164}$$

$$\emptyset_3 = \chi + 1 \tag{3.165}$$

The final potential energy of a plate, Π, in a rectangular tube is defined by:

$$\Pi = U + U_\Gamma + V \tag{3.166}$$

Terms U [strain energy of the plate] and V [energy corresponding to axial load] are defined by the expressions mentioned before (3.151) and (3.152). Finally, U_Γ is the energy associated to the elastic restriction against rotation along the unloaded edges:

$$U_\Gamma = \frac{\zeta_r}{2} \int_\Gamma \left[\left(\frac{\partial w}{\partial y}\right)^2_{y=0} + \left(\frac{\partial w}{\partial y}\right)^2_{y=b}\right] \partial\Gamma \tag{3.167}$$

According to the analysis carried out by (Cai, et al., 2009), by adding all the components of energy and using equation (3.162), it can be easily derived:

$$\Pi = \frac{D_r}{2}\left[\frac{8\pi^4 C^2 b}{a^3}A_1 + \frac{3C^2 a}{2b^3}A_2 + 2(1-\mu)\frac{2\pi^2 C^2}{ab}A_3 - \frac{4\pi^2 C^2}{ab}A_4\right] + \frac{3C^2 \cdot \zeta_r \cdot a \cdot (1 + A_5^2)}{4b^2} - \frac{p_x \cdot t \cdot \pi^2 \cdot C^2 b}{a}A_1 \tag{3.168}$$

where coefficients A_1, A_2, A_3, A_4 and A_5 are:

$$A_1 = \frac{1}{3} + \frac{\phi_1}{2} + \frac{\phi_1^2 + 2\phi_2}{5} + \frac{\phi_3 + \phi_1\phi_2}{3} + \frac{\phi_2^2 + 2\phi_1\phi_3}{7} + \frac{\phi_2\phi_3}{4} + \frac{\phi_3^2}{9} \tag{3.169}$$

$$A_2 = 4\phi_1^2 + 12\phi_2^2 + 12\phi_1\phi_2 + \frac{144}{5}\phi_3^2 + 16\phi_1\phi_3 + 36\phi_2\phi_3 \tag{3.170}$$

$$A_3 = 1 + 3\phi_1 + 2\phi_1^2 + 4\phi_2 + 5\phi_3 + 5\phi_1\phi_2 + 6\phi_1\phi_3 + 7\phi_2\phi_3 + 3\phi_2^2 + 4\phi_3^2 \tag{3.171}$$

$$A_4 = \phi_1 + \frac{2\phi_1^2 + 6\phi_2}{3} + 3\phi_3 + 2\phi_1\phi_2 + \frac{14\phi_1\phi_3 + 6\phi_2^2}{5} + 3\phi_2\phi_3 + \frac{12\phi_3^2}{7} \quad \textbf{(3.172)}$$

$$A_5 = 1 + 2\phi_1 + 3\phi_2 + 4\phi_3 \quad \textbf{(3.173)}$$

and according to the principle of minimum potential energy:

$$\frac{\partial \Pi}{\partial C} = 0 \quad \textbf{(3.174)}$$

equations (3.169) to (3.174) lead to:

$$\sigma_x \cdot t = \frac{\pi^2 D_r}{b^2}\left[\frac{4}{\gamma^2} + \frac{3\gamma^2 A_2}{4\pi^4 A_1} + \frac{2(1-\mu)A_3 - 2A_4}{\pi^2 A_1} + \frac{3\chi\gamma^2(1 + A_5^2)}{2\pi^4 A_1}\right] = k\frac{\pi^2 D_r}{b^2} \quad \textbf{(3.175)}$$

where γ is a parameter that correspond to half wavelength, or $\gamma = a/b$, being k the coefficient of elastic local buckling defined as:

$$k = \frac{4}{\gamma^2} + \frac{3\gamma^2 A_2}{4\pi^4 A_1} + \frac{2(1-\mu)A_3 - 2A_4}{\pi^2 A_1} + \frac{3\chi\gamma^2(1 + A_5^2)}{2\pi^2 A_1} \quad \textbf{(3.176)}$$

When $\partial k/\partial\gamma = 0$, the minimum value of k is obtained, and it is known as k_{cr}. By deriving the equation (3.176) respect γ and optimizing the function, we can obtain the value of the critical half wavelength:

$$\gamma_{cr} = 2\pi \cdot \left[\frac{A_1}{3A_2 + 6\chi(1 + A_5^2)}\right]^{1/4} \quad \textbf{(3.177)}$$

This way, and replacing this last equation in (3.176), the value of k_{cr} can be derived. The critical stress of local buckling of the plate, clamped in the two loaded edges and restricted to buckling in the other two, can be defined by:

$$\sigma_{cr} = \frac{k_{cr}\pi^2 E}{12(1-\mu^2)(b/t)^2} \quad \textbf{(3.178)}$$

When the rotational stiffness of the unloaded edges tends to zero ($\zeta_r = 0$), then χ is also zero and consequently, the half wavelength is equal to 1.52 [case a) of Fig. III.30]:

$$\chi = 0$$

$$\phi_1 = 0; \quad \phi_2 = -2; \quad \phi_3 = 1$$

$$A_1 = \frac{1}{3} + \frac{-4}{5} + \frac{1}{3} + \frac{4}{7} + \frac{-2}{4} + \frac{1}{9} = 0.049$$

$$A_2 = 48 + \frac{144}{5} - 72 = 4.8$$

$$A_5 = 1 - 6 + 4 = -1$$

$$\gamma_{cr} = 2\pi \cdot \left[\frac{0.049}{14.4}\right]^{1/4} = 1.52$$

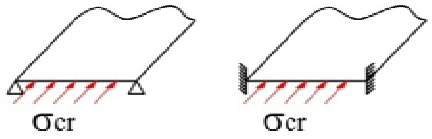

a) b)

Fig. III.30 Critical stress depending on boundary conditions.

This would correspond to the case of a plate loaded in two of the four edges and simply supported in the other two, so that the restriction against rotation of these last edges of the tube would not be considered. The value obtained before means that the distance called "*a*" in figure III.28 would be equal to $1.52 \cdot b$, being *b* the width of the tube. On the contrary, when the rotational rigidity of the two unloaded edges is assumed infinite, ($\zeta_r \to \infty$), then [case b) of Fig. III.30]:

$$\chi = \infty$$

$$\phi_1 = \infty; \quad \phi_2 = -\infty; \quad \phi_3 = \infty$$

$$A_1 = A_2 = A_5 = \infty$$

And solving the limit of the function that expresses the critical half wavelength, it is derived that[13]:

$$\lim_{x \to \infty} \gamma_{cr} = 1.00$$

In this case, the magnitude "*a*" coincides with the width of the tubular section, *a=b*.

3.3.3 Influence of the slenderness of the plate on the amplitude of local buckling.

The importance of local buckling effects in determining the confinement effect of rectangular CFT sections has been widely explained before. This fact is due to the influence of transversal rigidity of the plates on the deformability of the tube, and the derived pressure to the core. The decisive variable in order to determine the amplitude of the wavelength in transversal deformation is the length of the widest side of the tube. As larger is the length between the two rigid edges, larger is the deflection of the mid-span area. Besides, this increase of deformation is clearly non-linear.

As it has been mentioned before, the deformability of the plate has a clear influence on the capacity of the tube of providing confinement to the core. As larger is the B/t ratio, lower is the critical stress.

According to Bleich (Bleich, 1952), the parameter of the rotational restriction of the unloaded edges in square-shaped CFT sections can be obtained through the following expression:

$$\chi = \left(\frac{\alpha \cdot t_w}{t_f}\right)^3 \cdot \frac{r'}{\rho} \qquad \textbf{(3.179)}$$

[13] The first who propose this value was Uy and their collaborators (Uy, et al., 1996)

where:

$$r' = 2 - \left(\frac{t_f \cdot b_w}{t_w \cdot b_f}\right)^2 \qquad \textit{(3.180)}$$

$$\rho = \frac{1}{\pi} \cdot \tanh\left(\frac{\pi \cdot b_w}{4 \cdot b_f}\right) \cdot \left[1 + \frac{\pi \cdot b_w/2 \cdot b_f}{\sinh(\pi \cdot b_w/2 \cdot b_f)}\right] \qquad \textit{(3.181)}$$

By following the condition:

$$\frac{t_f \cdot b_w}{t_w \cdot b_f} \leq 1.0 \qquad \textit{(3.182)}$$

t_w *Thickness of the transversal plate to the analyzed one.*
t_f *Thickness of the analyzed plate*
b_w *Width of the transversal plate to the analyzed one.*
b_f *Width of the analyzed plate*
α *Experimental coefficient, with an approximated value of 0.80*

Thus, for instance, in case of a square-shaped section of 400x400 mm width and 3 mm thick:

$$\rho = \frac{1}{\pi} \cdot \tanh\left(\frac{\pi}{4}\right) \cdot \left[1 + \frac{\pi/2}{\sinh(\pi/2)}\right] = 0.351$$

$$\chi = \alpha^3 \cdot \frac{r'}{\rho} = 0.80^3 \cdot \frac{1}{0.351} = 1.458$$

$$\emptyset_1 = 1.458 \quad ; \quad \emptyset_2 = -2(\chi + 1) = -4.916 \quad ; \quad \emptyset_3 = \chi + 1 = 2.458$$

$$A_1 = 0.079 \quad ; \quad A_2 = 8.832 \quad ; \quad A_3 = 0.000 \quad ; \quad A_4 = -0.776 \quad ; \quad A_5 = -1.000$$

$$\gamma_{cr} = 1.289 \quad ; \quad \boldsymbol{\sigma_{cr} = 162.420\ N/mm^2}$$

The critical stress of the plate is about 162.42 N/mm², a value clearly below the yield limit stress. And in a similar square-shaped section of 3 mm thick, but this time 200 mm width [as a result of introducing stiffening plates inside the core]:

$$\rho = \frac{1}{\pi} \cdot \tanh\left(\frac{\pi}{4}\right) \cdot \left[1 + \frac{\pi/2}{\sinh(\pi/2)}\right] = 0.351$$

$$\chi = \alpha^3 \cdot \frac{r'}{\rho} = 0.80^3 \cdot \frac{1}{0.351} = 1.458$$

$$\emptyset_1 = 1.458 \quad ; \quad \emptyset_2 = -2(\chi + 1) = -4.916 \quad ; \quad \emptyset_3 = \chi + 1 = 2.458$$

$$A_1 = 0.079 \quad ; \quad A_2 = 8.832 \quad ; \quad A_3 = 0.000 \quad ; \quad A_4 = -0.776 \quad ; \quad A_5 = -1.000$$

$$\gamma_{cr} = 1.289 \quad ; \quad \boldsymbol{\sigma_{cr} = 649.680\ N/mm^2}$$

The critical stress grows up to 649.68 N/mm^2.
The critical stress –used to determine the point from where the plate starts to buckle- has been increased almost four times, although the half wavelength ratio is still the same. While the width has been reduced only to a half-part, the critical stress has been enhanced 4 times and buckling clearly starts after the yield limit stress of the plate. This is the reason why geometric proportions of the plate [width to thickness] are crucial in order to determine the effects of buckling; in figure III.31 presented below, the influence of combining different widths and thicknesses on the value of the critical stress is shown.

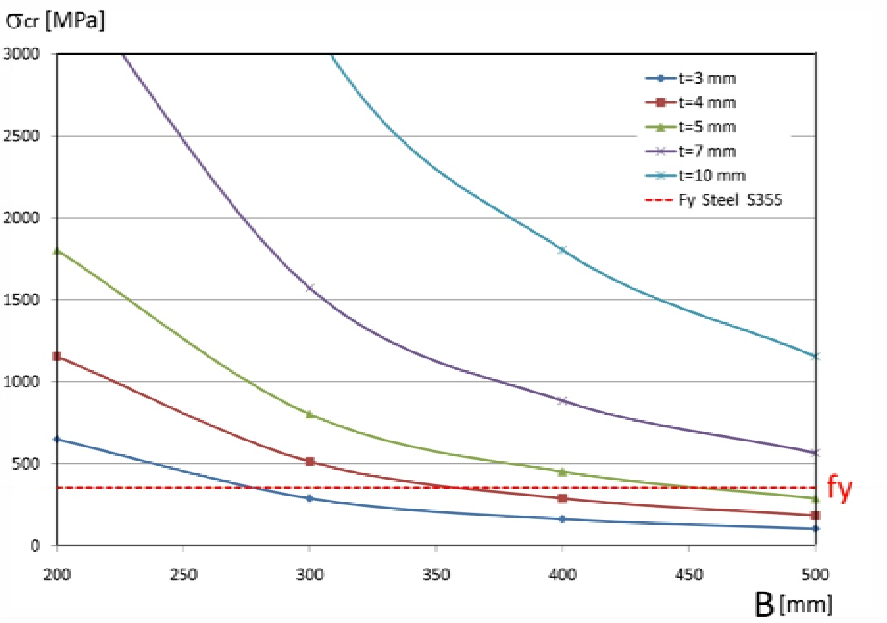

Fig. III.31 Comparison of critical stresses between tubes of different widths and thicknesses. All the combinations under the dashed line are susceptible of buckling in the elastic range.

3.3.4 Resistant advantages of introducing stiffening plates in square CFT sections.

As it has been explained in previous Sections, the final purpose of this study is to valorize the behavior and advantages of stiffening CFT sections. Different from circular concrete-filled tubes, the fact of introducing stiffening plates in concrete core of rectangular sections seems to provide to the tube more than one mechanical advantage. To determine the influence of stiffening plates on the compressive behavior of square CFT sections, it is also convenient to differentiate thin-walled tubes from thick-walled ones.

In the first case, from conclusions obtained in Section 3.3.3, it can be derived that as larger is the slenderness of the plates in rectangular sections, wider is also the transversal deformation and therefore, lower is its global strength. The fact of stiffening these sections reduces the buckling length and increases the global strength of the composite section automatically. The aim of "stiffening" square-shaped sections is to reduce the slenderness of the plates involved and to standardize the behavior of these sections through an individual response of different alveoli. By reducing the buckling length of loading cells, it is also possible to diminish the second order effects notably.

This effect can be observed through the diagram of figure III.31 in the previous Section. This figure shows how the critical stress of the plates is dizzily increased, as its size diminishes. As an example,

a square-shaped tube of 400mm width and 3 mm thick never reaches the yield limit stress of steel, since its plates start buckling before; contrarily, another section of equivalent thickness with reticulated alveoli of 200 mm width can take full advantage of the yield stress of steel. This fact justifies itself the introduction of stiffening plates in square-shaped tubes. By disposing internal plates, thin-walled tubes can be converted into thick-walled tubes; besides, the plates which are embedded in the core are restricted to buckling and therefore, they could be assumed really thin.

Analyzing now the effect of introducing stiffening plates with different thicknesses, it can be observed how the half wavelength parameter decreases as the thickness of the contiguous plate grows. In thin-walled square tubes, the introduction of these plates is really decisive. From the figure shown before, it can be derived that for equivalent plate thicknesses [both inner and outer plates of 5 mm], the half wavelength of the deformed shape is approximately 1.30 times the length of the widest side of the section [Fig. III.32]. Contrarily, it is also shown how the result of disposing these plates two times thicker than the tube leads to an equivalent result as the one obtained from a plate embedded by the four edges [γ_{cr} = 1.05 ≈ 1].

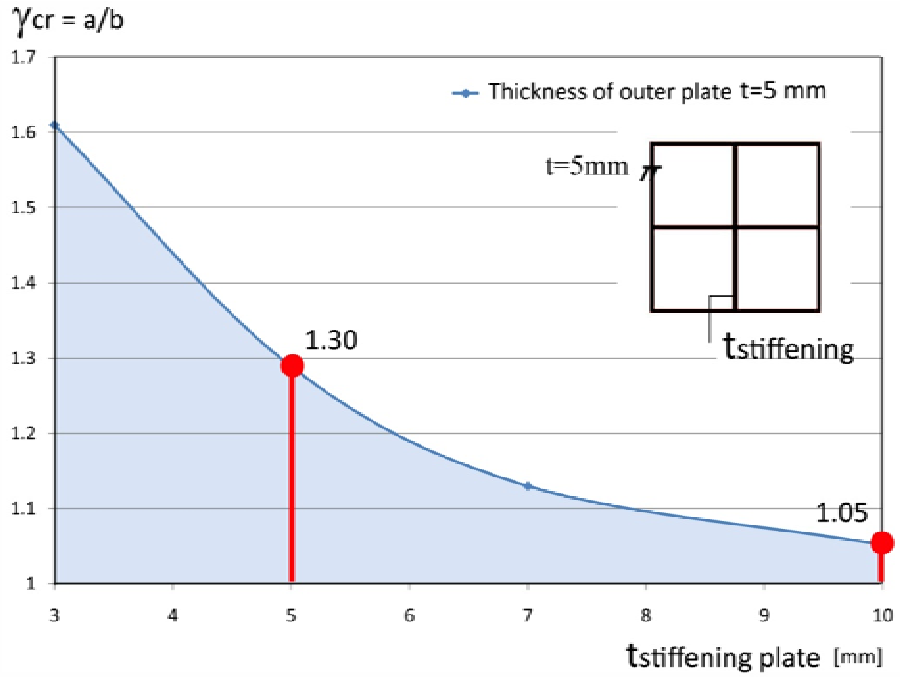

Fig. III.32 Evolution of the half wavelength depending on the thicknesses of the plates, in a 5mm-thick reticulated square tube.
The half wavelength diminishes dizzily with the growth of the thickness of the stiffening plate. This diagram belongs to a square-shaped tube of 5 mm wall-thickness.

The "contiguous plate" in the previous diagram refers to the stiffening plate.
For the second group corresponding to thick-walled rectangular sections, the presence of stiffening plates is also important: they reduce the deflection at the mid-span of the outer plates. This way, the confinement effect can be also clearly enhanced. Bending of the plates in a thick-walled rectangular tube only occurs in the cross-sectional plane, as it is shown in figure III.33 a).

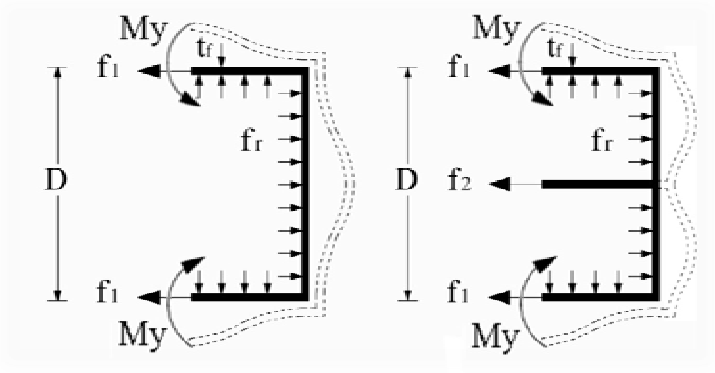

Fig. III.33 Distribution of pressure on the steel tube: a) unstiffened, b) stiffened.
The introduction of these plates reduces considerably the deflections of the deformed shape.

It will be demonstrated later that, contrarily to circular sections, in stiffened square-shaped tubes tensile forces of the stiffening plates are usually larger than tensile forces of the tube walls, $f_2 > f_1$. This fact is caused by the stiffening provided by these inner plates and the poor efficiency of the square geometry in distributing the pressure coming from concrete expansion.

Through a bidimensional elastic analysis of square-shaped sections, and by applying a uniform distributed pressure, we can clearly note the benefits of introducing stiffening plates in thick-walled rectangular and square-shaped CFT sections. The stiffening plates introduced in concrete core absorb most part of the pressure axially, coming from volumetric expansion of concrete. Thus, the span of the tube plates is reduced in a half part, and the curvature of the deformed shape also diminishes [see figure III.34].

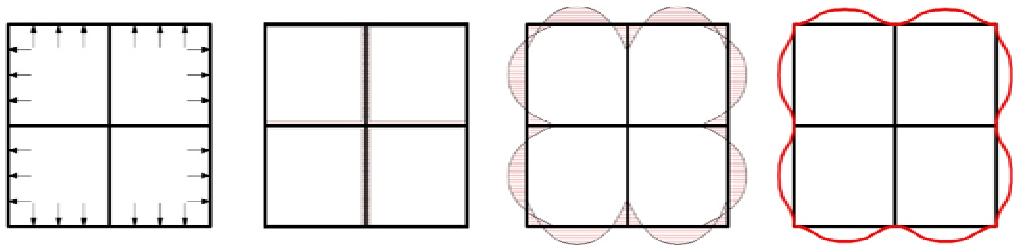

Fig. III.34 Influence of stiffening plates on lateral deformability.
The introduction of stiffening plates improves the confinement effect also in thick-walled tubes, since it reduces the deformability of the plates in the cross-sectional plane.
[a] Uniform pressure [b] Axial load [c] Bending moments [d] Deformed shape

The influence of the ratio between the thicknesses of the plates is not decisive in order to restrain the deformability of thick-walled tubes, but it is in thin-walled sections. A simple elastic analysis in the cross-sectional plane has been done with different thicknesses of the stiffening plates [the first case with both thicknesses equal to 0, a second case with the inner plate 50% thinner than the outer and a third case with the inner plate two times thicker]. Note that in the two latter cases, the axial load absorbed by the stiffening plates is much higher than that of circular sections, owing to

the inefficiency of the square geometry [Fig. III.21]. Benefits in this case are not only significant, but also decisive to guarantee the confinement effect on concrete core.

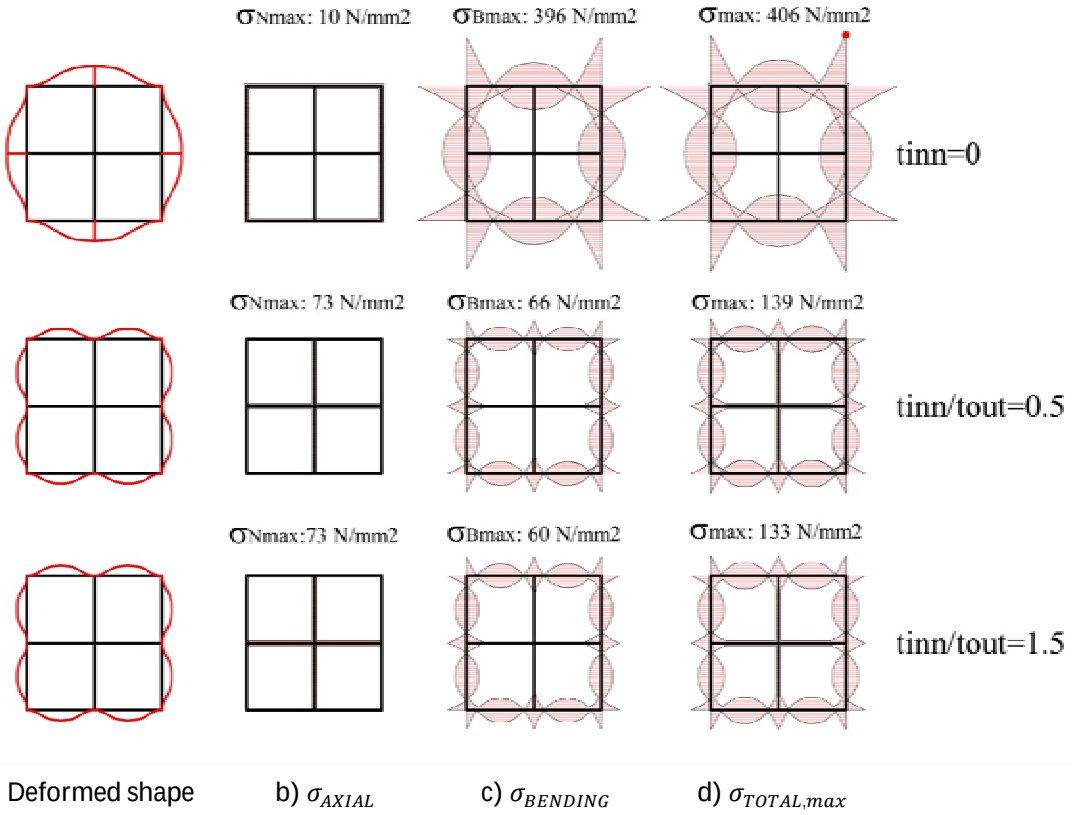

Fig. III.35 Influence of the thickness of the stiffening plates on the deformability of the tube.
The introduction of these plates reduces considerably the half wavelength of the deformed shape.
[a] Deformed shape [b] Stress from Axial Force [c] Stress from Bending Moment
[d] Total Max Stress

The surprise was to discover how the plate thickness does not have a decisive importance on the deformed shape of thick-walled tubes. Once the tube is stiffened, internal plates become axially tensioned by restricting the deflection of the plates, independently of their thickness [deflections from bending are much higher than elongation of the stiffening plate, see Fig. III.36]. As a result, ductility may be also clearly enhanced, since the collapse seems to be clearly delayed [see the results presented in Chapter VI].

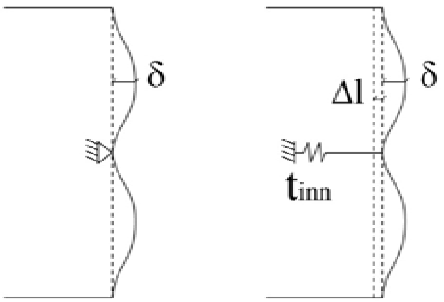

Fig. III.36 Influence of the thickness of the stiffening plates on the deformability of the tube.
The introduction of these plates reduces considerably the half wavelength of the deformed shape.